Title
Computational simulations and methods for biomedical applications

Author
Felberg, Lisa E.

Publication Date
2017

Peer reviewed|Thesis/dissertation

Computational simulations and methods for biomedical applications

by

Lisa E. Felberg

A dissertation submitted in partial satisfaction of the

requirements for the degree of

Doctor of Philosophy

in

Chemical Engineering

and the Designated Emphasis

in

Computational and Data Science and Engineering

in the

Graduate Division

of the

University of California, Berkeley

Committee in charge:

Professor Teresa Head-Gordon, Chair
Professor Bryan McCloskey
Professor Mark Asta

Summer 2017

Computational simulations and methods for biomedical applications

Abstract

Computational simulations and methods for biomedical applications

by

Lisa E. Felberg

Doctor of Philosophy in Chemical Engineering

Designated Emphasis in Computational and Data Science and Engineering

University of California, Berkeley

Professor Teresa Head-Gordon, Chair

The interplay of molecular simulations and experiment have been instrumental in the last decade in establishing quantitative understanding of the physics underlying molecular processes relevant to applications involving interfaces, polymers and biopolymers and the water solvent used to solvate them. Water in confinement is present in a range of biological environments on the cellular level, important for stimuli responsive polymers and their use as drug delivery vehicles, and is ubiquitous in many technological applications such as water desalination. In the first half of this dissertation, I have used a range of experimental and simulation techniques to study water in nanoscale confinement for water between graphene sheets and water trapped in stimuli-responsive star diblock polymers. Using MD simulations to study water confined between two graphene walls, it was observed that different phases of water could be created as a function of the two-dimensional density and graphene wall flexibility such as square and hexagonal ice. Additionally, at incommensurate 2D densities, the flexible walls were found to bend, creating a coexistence in the system between n- and (n+1) water interlayers. Using small angle X-ray scattering and MD simulations, I determined that by varying the hydrophilic block chemistry of the star polymer arms using poly-ethylene glycol (PEG), poly-2,methyl-oxazoline (POXA) and a highly branched polycarbonate-based polymer with a pendant hydrophilic group (PC1), only the PEG system displayed thermosensitivity over the temperature range observed due to reduction in water entropy, while an increased sidechain length and charge density leads to decreased solvent interactions. In addition to temperature sensitivity, pH sensitivity of acidic, basic and neutral polymers was studied in non-degradable nanogel star polymers. Using small angle X-ray scattering, it was found that the acidic (PMAA) and basic (PDMAEMA) polymers exhibited sharp transitions between expanded and collapsed states, with apparent pK_as that were qualitatively different from the reported monomer pK_as. By modulating the fraction of basic or acidic groups in the hydrophilic region, we were also able to change the apparent pK_a of the star polymer.

Despite the large success of traditional atomistic simulation methods, their applicability to systems of large size and long time scales are prohibitive. Therefore there exists a need to develop novel methods to overcome this obstacle. In the second half of my thesis I present an efficient method to evaluate the electrostatic interactions in large molecular systems based on the linearized Poisson-Boltzmann equation (LPBE) , which allows for the simulation of much larger systems at a fraction of the cost.[1–3]. I have developed a robust software implementation of the fully analytical LPBE model, PB-AM, which solves for the complete mutual polarization potential of a system comprised of an arbitrary number of molecules with arbitrary charge distributions in a screened environment with each molecule represented as a single, spherical, low dielectric cavity. I also developed a software implementation of the semi-analytical LPBE solution, PB-SAM [2, 3] that extends the analytical model that represents a molecule as a collection over overlapping rigid spheres that better describes a detailed molecular boundary. The software is available as stand-alone code, with automated installation using CMake and is also available as a part of the distributed and open source software in the highly popular Adaptive Poisson-Boltzmann Solver (APBS) package. Both software implementations have new features of a simple application programming interface, can produce electrostatic potential visualizations in two and three dimensions, and run Brownian dynamics schemes with a variety of applications.

To my family

Contents

List of Figures

List of Tables

Acknowledgments

First and foremost, I want to thank my family. They have always been there for me, challenging and encouraging me. My parents are amazing, inspiring and giving, and have always supported me. My sisters although distant, have always been there with kind text messages and my thoughts are always with them, regardless of where we travel. I also want to thank Mike, who has been my family for the past five years.

Thanks to my advisor Teresa Head-Gordon, and the members of the Head-Gordon group, who have been great lab mates. The lab has been such a diverse environment to learn about a large number of projects, and to work with such a talented professor and graduate students. Alex Albaugh has been a constant friend, confidant and roommate, and I cannot thank him enough, for everything. Thanks to Luis Pestana, a brilliant and driven Post-Doc in the THG lab who was such a great person to work with on my last project. Additionally, I have had the opportunity to work with some very amazing undergraduate researchers: Anjali Doshi and David Brookes, who is now embarking on his own PhD. I know that they both will accomplish great things.

I want to thank the people I have worked with at IBM: Amber Carr, William Swope and Julia Rice. It has been such a pleasure collaborating with you during the past three years. I always look forward to our meetings, and want to thank you for hosting me down at Almaden. Thanks to the group at Pacific Northwest National Lab. My internship there was such an amazing experience and it was really nice working with Elizabeth Jurrus, Nathan Baker, Juan Brandi-Lozano, Keith Star, Leighton Wilson and Maria Tartakovsky.

Chapter 1

Introduction

Physics-based computer simulations of molecular systems provide insight and predictions that can guide the design of experiments. Classical molecular dynamics (MD) based on empirical force fields has been instrumental in the study of large molecules such as polymers and biopolymers [4] and complex solid-liquid interfaces. Coarse-grained models, where the large number of degrees of freedom of the original atomistic system are systematically reduced, have also provided important insight on longer timescales and lengthscales not accessible from atomistic approaches [5]. Advancements in molecular simulations can be generally divided into method development and application, and this thesis covers both aspects. For the first part, molecular atomistic simulation and X-ray scattering techniques were used to understand the physical properties of two different nanoscale systems: water in graphene confinement and nanogel star diblock copolymers. The second part concerns new software efforts to develop novel and efficent solvers of the linearized Poisson-Boltzmann equation into robust software that were made available in the Adaptive Poisson Boltzmann Solver (APBS) community code.

Molecular dynamics and experiments on nanoscale systems

The widespread use of computational methods has allowed for a deep exploration of systems that were previously inaccessible to experimental techniques. Often computational methods are used in tandem with experimental methods to elucidate underlying atomistic mechanisms for experimental observables and are used to access system properties otherwise inaccessible by traditional methods. For this reason, MD was chosen to study two nanoscale systems: water in nanoscale confinement and nanogel star polymers.

The study of water in its many forms has always been an area of great interest for a range of scientific studies, due to its ubiquity and unique long-range structure and properties. In contrast to water in a bulk environment, water in a confined environment exhibits drastically different structural and dynamic properties. Although it may not immediately be apparent,

water in a confined form is just as ubiquitous as that in bulk, from biological systems (cell interiors, and membrane pores and channels), as well as industrial systems (presence of moisture in instruments) and technology (desalination). Thus, the characterization of water in confinement has recently become a growing field field with applications in a variety of domains, including biological applications [6, 7], microfluidics [8] and energy conversion [9, 10].

The introduction of hydrophobic walls immediately alters the structure of water by introducing an anisotropic interface. Additionally, the form of these walls, e.g. in parallel walls or nanosized tubes, reduces the dimensionality of the system, to 2D and 1D, respectively. The effect of the hydrophobic confinement is generally analyzed by a characteristic length scale, such as plate separation for lamellar systems, and pore diameter for nanotubes. With larger length scales, the systems are typically divided into a core-shell or two-state model [11, 12], which considers two different regions of confined water - those in the core are far enough from the wall that they behave like bulk water and those in the shell, whose properties are affected by the presence of the wall. Confined solute properties and experimental results can then be interpreted as a linear combination of these two regions. Recently [13], the validity of this approximation has been examined, and it is also evident that this model is not valid at length scales commensurate with the size of water solvation shells.

At the smaller length scales, all confined water is affected by the presence of an interface. Structurally at the smallest confinement lengths, water adapts ice-like structures, both in carbon nanotubes (CNT) and lamelllar graphene. In the carbon nanotubes, it has been seen that the ice monolayer mimics the cylindrical nature of the CNT, through x-ray diffraction and molecular dynamics (MD) studies. [14] In graphene sheets, ice has been seen in transmission electron microscopy (TEM) [15] as well as MD simulations of monolayers and bilayers of water. [16, 17] Almost all theoretical studies of water under confinement do not account for flexibility of the confining environment.

In chapter 2 of my thesis, I have quantified the structure and dynamics of water in graphene confinement as a function of graphene flexibility and two-dimensional water interlayer density, ρ_{2D}. With increasing ρ_{2D}, both the rigid and flexibly confined water transitioned from monolayer (ML) to bilayer (BL) to trilayer (TL) systems, in the out-of-plane direction. It was found that at intermediate 2D densities, the flexible graphene walls bend to accommodate a coexistence between n- and (n+1) water interlayers, e.g. ML and BL or BL and TL. Additionally, as ρ_{2D} was increased, both ML systems transitioned from disordered liquid to square ice. In the rigid BL system, the lower densities formed a coexistence between hexagonal ice and low-density vapor regions. These features were not observed in the case of rigid walls. This allows experimentalists to consider a new parameter - bending modulus or rigidity - to control nanoscale behavior.

Recent advances in polymer synthesis have advanced nanogel star polymers [18–20] as materials with interesting properties for a range of applications, including lubrication for engine oils [21], medical imaging [22] and drug and biomaterial delivery [23]. One of the goals of polymers for biomedical applications is the tunable response of an expansion-to-collapse transition as a function of environmental conditions, such as pH, ion concentration,

and temperature, and optimized for function over the ranges of physiological conditions found in the human body, such as an ion concentration differential across the cell wall or the low pH within the stomach. Leveraging the sensitivity of polymers to environmental conditions has been identified as a potential way to design a highly targeted and specified drug loading.

In chapter 3 of my thesis, I have focused on nanogel star diblock copolymers and their temperature sensitivity. For most polymers, the observed trend with temperature is an increase in solubility, usually accompanied by a phase transition from a two-phase system (ϕ_1 = solvent and ϕ_2 = polymer), to a one-phase system (ϕ_m = mixed phase of solvent and polymer). The temperature of this transition is a function of the chain length and the Flory-Huggins parameter, χ, a metric describing the energetic favorability of phase separation, and is known as the upper critical solution temperature (UCST). For some polymers, the opposite trend is observed. Upon heating, the polymer will phase separate from solution, at a temperature known as the lower critical solution temperature (LCST). Leveraging this collapsed-to-expanded transition, a polymer system that is expanded at high temperature can load drugs and as the temperature is lowered the polymer will collapse and entrap the drug cargo.

Chapter 3 explores the effect of sidechain length and hydrophilic chemistry on polymer properties. For all the systems, the hydrophobic chemistry was poly-δ-valerolactone (PVL) and the hydrophilic region was varied as poly-ethylene glycol (PEG), poly-2,methyl-oxazoline (POXA) and a highly branched polycarbonate-based polymer with a pendant hydrophilic group (PC1). It was found that increased branching lead to a decrease in polymer-water interaction. Generally, the star polymer systems had a collapsed, glassy hydrophobic region, with vastly differing hydrophilic block solvation. Only one of the polymers studied, the star polymer with a poly-ethylene glycol (PEG) hydrophilic region, displayed any thermosensitive behavior. This finding was confirmed by intermonomer and time autocorrelation functions, backbone dihedral angle analysis and polymer-water hydrogen bond interactions.

In chapter 4 of my thesis, I have focused on nanogel star diblock copolymers and their pH sensitivity. For this study, a star polymer with a divinyl benzene (DVB) cross-linked core, and diblock arms of hydrophobicpoly-styrene (PS) and hydrophilic poly-methyl methacrylate (PMMA) derivative arms was used. The PMMA side group was modified to create a poly-ethylene glycol methacrylate (PEGMA) derivative as well as pure acidic (PMMA), pure basic (PDMAEMA), and 50% PEG and acidic or basic sidechains. I used small angle X-ray scattering (SAXS) to characterize the star polymers in solution. The scattering intensity of a monodisperse system of particles, comprised of particles of the same size, shape and mass, is described as follows:

$$I(Q) = NP(Q)S(Q) \tag{1.1}$$

Where I(Q) is the experimental scattering intensity, N is the number of particles, P(Q) is the single particle scattering function, also known as the form factor, and S(Q) is the interparticle scattering function that accounts for interactions between particles. When the particles are non-interacting, the interparticle scattering function, S(Q), is approximately 1 and the main

function of interest becomes the single-particle scattering function, P(Q), also known as a form factor. Using analytical form factors and fitting these to the experimentally obtained scattering functions, one can obtain information about the general shape and size of the molecules. It was observed that as the polymers expanded and collapsed in solution, the analytical form factor changed, meaning the polymer structure changed. The control system with PEGMA hydrophilic block polymer displayed no transition or significant swelling or collapse events over the pH range studied. In contrast, when the acidic or basic polymers were charged, e.g. low pH for the basic and high pH for the acidic polymer, the polymer adapted the scattering profile of a blob model of a star polymer. When uncharged, the polymer adapted the scattering profile of a core-shell system. This transition was accompanied by a change of overall radius of gyration. It was also found that the hydrophilic block composition greatly altered the pK_a of the monomer units studied. For the basic polymer, the pK_a was found to be between that of a linear block and a small core polymer, previously reported [24]. For the polymers with 50% mixtures of PEGMA and acidic or basic polymers, the pK_a was shifted in unexpected ways. For the 50% basic polymer, the pK_a is much lower than that of the 100% basic block and for the 50% acidic polymer, the pK_a is shifted to high pH, when compared the monomer and linear forms of PMMA. This suggests that perhaps the PEGMA is stabilizing the protonated PMMA, as has been reported before with PEGMA-PMMA membranes.

Coarse-grain models and Linearized Poisson-Boltzmann equation Solvers

Coarse-grain (CG) models, where the atomistic degrees of freedom are reduced using a simpler model, enable computational studies of systems at larger length and time scales when compared to atomistic MD. To approach these longer length and timescales, a reduction of system complexity is needed. Strategies to reduce the degrees of complexity of the systems generally aim to reduce the number of particles in the system, which may involve, for example, representing a group of atoms as a single entity or removing the explicitly defined solvent molecules. In many applications, other energetic interactions, for example, electrostatics, dominate molecular behavior such that the atomistic details of the solvent are in comparison, negligible. Additionally, when reducing the degrees of complexity, it is often beneficial to reduce the complexity of the solute. Therefore for many important biological systems, charge interactions are the predominant driving force for aggregation and association, which can be described by the nonlinear and linear forms of the Poisson-Boltzmann equation.

The linearized Poisson-Boltzmann equation (LPBE) is a linearization of the nonlinear Poisson-Boltzmann equation (PBE), which is given as

$$-\nabla[\epsilon(r)\nabla\Phi(r)] - 4\pi\sum_i \bar{n}_i Z_i exp\left(-\frac{eZ_i\Phi((r)}{k_BT}\right) = 4\pi\rho_{\text{fixed}}(r) \tag{1.2}$$

where $\Phi(r)$ is the electrostatic potential at position $\mathbf{r}$, ϵ is the dielectric function, ρ_{fixed} is the molecular fixed charge density. $\bar{n}_i$ and Z_i are bulk concentration and valence of ion species i respectively, e is the fundamental electronic charge, k_B the Boltzmann constant and T the system temperature. From the nonlinear PBE, the LPBE is obtained by assuming that $eZ_i\Phi/k_BT << 1$ and that the salt is monovalent and is in a 1:1 ratio of cations to anions, resulting in the linearized form:

$$-\nabla[\epsilon(r)\nabla\Phi(r)] + \kappa^2\Phi(r) = 4\pi\rho_{\text{fixed}}(r) \tag{1.3}$$

Where $\kappa = \sqrt{8\pi\bar{n}e^2/\epsilon_s k_B T}$ is the inverse Debye length.

Coupled with the LPBE solution for the solute we can describe its dynamics as it experiences random, constant collisions as well as frictional drag. The Langevin equation of motion, describing the position of solute, r:

$$m\ddot{r}(t) = -\xi\dot{r}(t) + F_c(t) + F_R(t) \tag{1.4}$$

where m is the solute mass, ξ is the damping constant, $F_c(t)$ is the conservative force and $F_R(t)$ is a random force that is a Gaussian with a delta correlation (e.g. $\langle F_R(t) \cdot F_R(t')\rangle = \delta(t-t')$). In cases where the solute is much larger in size and mass than the solvent molecules, we may further simplify the equation of motion by taking the limit of no inertia and obtain the equation for Brownian motion:

$$\xi\dot{r}(t) = F_c(t) + F_R(t) \tag{1.5}$$

By simple integration, we obtain the following equation in a system of N particles for the displacement of particle i, $\Delta r_i = r_i(t+\Delta t) - r_i(t)$, in Brownian dynamics (BD)

$$\Delta r_i = \sum_{j\neq i}^{N} \frac{D_{ij}(t)F_{c,j}(t)}{k_BT}\Delta t + R_i(\Delta t) \tag{1.6}$$

where j is another particle in the system, $D_{ij}(t)$ is the configuration-dependent diffusion tensor, and $R_i(\Delta t)$ is a Gaussian-distributed random displacement with zero mean and variance $2D_i\Delta t$, where D_i is the 6×6 generalized diffusion tensor of particle i at the center of diffusion. The diffusion tensor can be simplified in isotropic cases to $D_{ij}(t) = \delta_{ij}D(t)$.

In chapters 5 and 6, I focus on progress in developing simulation techniques, using a novel solution to the LPBE. Chapter 5 presents an updated version of the open-source software for a fully analytical solution to the LPBE: PB-AM. We present the software algorithm and new techniques for visualization. Chapter 6 presents a numerical expansion of PB-AM, the Poisson-Boltzmann Semi-Analytical method (PB-SAM). This work also includes extension of the software to improve the user interface and to assist in creating informative outputs, such as electrostatic potential visualizations and simulation schemes. Additionally, the software is available online as open-source and has extensive documentation with a website and PDF manual.

Chapter 2

Coexistence of multilayered phases of confined water: the importance of flexible confining surfaces

Flexible nanoscale confinement is critical to understanding the role that bending fluctuations play on biological processes where soft interfaces are ubiquitous, or to exploit confinement effects in engineered systems where 2D materials, inherently flexible, are pervasively employed. Using molecular dynamics simulations we compare the phase behavior of water under nanoconfinement between flexible and rigid graphene sheets as a function of the in-plane density, ρ_{2D}. We find that both rigid and flexible cases show commensurate mono-, bi-, and tri-layered states, however the multi-layered states and transitions between them are qualitatively different for the rigid and flexible cases. The rigid systems exhibit discontinuous transitions between an (n)-layer and an (n+1)-layer state at particular values of ρ_{2D}, whereas under flexible confinement we find that the graphene sheets bend to accommodate an (n)-layer and an (n+1)-layer state that coexist at equilibrium at the same density. We show that the flexible walls introduce a very different sequence of ice phases and their phase co-existence with vapor and liquid phases than that observed with rigid walls. A particularly striking example is seen at intermediate densities where the rigid walls invoke an aligned-stacking of hexagonal ice with a large number of defects at a solid-gas interface, whereas the flexible walls never nucleate a solid phase but instead exhibit a coexistence between two different liquid states. Our study provides new comprehensive understanding

of the phase behavior of confined water under a more experimentally realistic model of graphene, and sheds light into the role of flexible confinement and its interplay with commensurability effects.

Introduction

The properties and phase behavior of water under nanoconfinement are remarkably different than that in the bulk, which has important implications for a myriad of nanotechnology materials applications and biological processes [25–28]. Driven by the pursuit of understanding the anomalous phase behavior of confined water, topics such as low-dimensional ice formation [15, 29, 30], unconventional phase transitions [31–34], and hydrophobic evaporation or dewetting [35–39], have been extensively studied over the last two decades. The specific manifestation of anomalous water phase behavior depends on the nature of the confining environment, e.g. surface chemistries, surface roughness, and/or 1D or 2D geometric boundaries that may or may not be deformable. Graphene, a highly flexible two-dimensional carbon allotrope [40, 41], has become a paradigmatic example of a 2D hydrophobic confining surface [42]. In graphene nanocapillaries, since the effect of the confining carbon interfaces on water persists at short range ($\sim$5 Å) [43, 44], nanoconfined water can adopt a multi-layered structure characterized by strong density fluctuations along the direction of confinement. Confinement has been shown to play a critical role in the formation of stable multi-layered two dimensional ice [45–47],which at room temperature forms at pressures on the order of several GPa [34]. Even at ambient pressures the formation of square ice from droplets of water confined between graphene sheets has been observed experimentally [15], which is possible because the interfacial adhesion forces between the confining graphene surfaces are effectively generating pressures of $\sim$1 GPa within the confined space. Confinement may also give rise to phase coexistence, in which molecular simulations have observed a stable liquid water layer that is enveloped between two ice layers under 2D hydrophobic boundaries [31, 48]. Besides thermodynamic control parameters, such as pressure or temperature, the phase behavior of water under confinement is affected by the commensurability between the confinement distance and the density of water. [15, 31, 34, 47, 48] For example, driven through incommensurate transitions, a transformation from a liquid, to a low-density ice phase, back to a high-density liquid, to finally a high-density ice phase, has been predicted for water nanofilms. [32] In another recent study, it was found that oscillations in the shear viscosity of confined water of several orders of magnitude occur over small variations in the confinement distance (under 1 Å). [49] When the density and confining distance are incommensurate, the system can also exhibit a sharp transition to a different multi-layer state with different types of phases. Giovambattista et al. found a phase transition between a bilayer liquid and a trilayer heterogeneous fluid (THF), characterized by highly ordered ice layers close to the confining surfaces and a disordered (liquid) middle layer, upon increasing the density of water while keeping the confinement distance constant between 8 - 9 Å. [31] When the confinement distance was kept at 6 Å, a transition between THF and bilayer ice

occurred upon decompression instead. Despite the extensive research efforts, most computational studies, however, have focused on rigid confinement, with only a handful of studies having investigated water confined within flexible surfaces [15, 35, 50], and none have systematically addressed the phase behavior of water under conditions of deformable interfaces. The question we aim to answer here is whether the phase behavior of water mapped under rigid confinement can be extended to the more relevant scenario of flexible confinement, under ambient conditions of temperature and pressure (0.1 MPa and 300 K) that are relevant in most practical applications In this paper, we use molecular dynamics simulations at constant ambient pressure and temperature to study the phase behavior of water confined under flexible graphene sheets in which we systematically vary the amount of water in the nanoslit (the 2D density of water, ρ_{2D}) and relax the system in the confinement direction so that it reaches an equilibrium confinement distance, d_{gg}. We also simulate the same systems using rigid graphene sheets for comparison. We find that both rigid and flexible cases show intervals of ρ_{2D} where the d_{gg} changes systematically from monolayer (ML) to bilayer (BL) to trilayer (TL) commensurate states of the system. However, we find that the multi-layered states and the transitions between them are qualitatively different for the rigid and flexible cases. Our study provides new comprehensive understanding of the phase behavior of confined water based on a more realistic model of graphene, and we believe it will be useful to interpret experimental results in the future, where graphene is ubiquitously employed.

Results

Out-of-plane ordering

We first analyze how the number of layers in the system varies with the 2D density over the range $0.06 < \rho_{2D} < 0.5$, which allows us to sample systems ranging from an incomplete ML to complete TL systems, beyond which the system adopts an equilibrium phase that tends is consistent with towards bulk conditions. The 2D density is the only control parameter in our systems, i.e. the confinement distance d_{gg} is not prescribed, but adopts an equilibrium value for a given ρ_{2D}. In addition, by using ρ_{2D} as a control parameter, we also avoid making ambiguous assignments of the 3D density under confinement, which requires choosing an ill-defined excluded distance from the confining surfaces.[51]

Figure 2.1 shows the dependence of the equilibrium confining distance on ρ_{2D}, for both flexible and rigid cases. We observe three well-defined regimes characterized by small changes of d_{gg}over relatively large variations in ρ_{2D}, which are separated by discontinuous transitions signaled by abrupt changes in d_{gg} over very small variations in ρ_{2D}. The first regime, 6 Å $< d_{gg} <$8 Å and $0.062 < \rho_{2D} < 0.123$ corresponds to ML states, the second regime 8 Å $< d_{gg} <$10 Å and $0.154 < \rho_{2D} < 0.215$ to BL states, and for 10 Å $< d_{gg} <\sim$15 Å and $\rho_{2D} > 0.245$ we observe the TL states. In the ML and BL states, the equilibrium confinement distance varies only marginally as ρ_{2D} is increased. For the TL case, however, a linear dependence is observed, $d_{gg} \propto \rho_{2D}$, which is a signature of bulk behavior since $\rho_{3D} = \rho_{2D}/d_{gg} =$ constant.

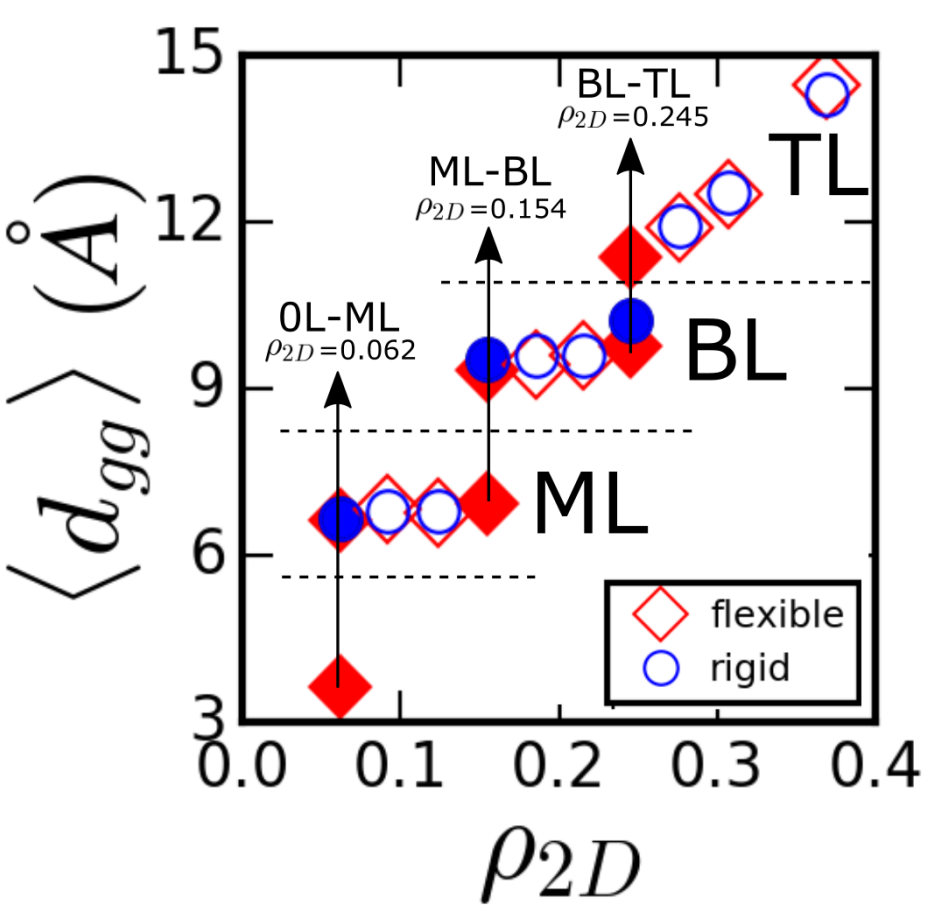

Figure 2.1: *Average confining distance, $\langle d_{gg} \rangle$, as a function of the 2D density of water, ρ_{2D}.* The confining distance is calculated as the average separation between the graphene sheets. The three transitions between no-water to monolayer (0L-ML), monolayer to bilayer (ML-BL), and bilayer to trilayer (BL-TL) are indicated in the plot by full symbols and vertical arrows. The ML, BL, and TL regimes are also illustrated, separated by discontinuous horizontal lines.

The transitions between the (n)-layer and (n+1)-layer states occur for both rigid and flexible graphene walls at the same values of ρ_{2D}, however they are found to be qualitatively different. For the case of rigid walls, the ML-BL and BL-TL transitions are sharp, although more finely spaced density values would be required to quantify whether the two transitions are closer to first or second order behavior. However, for the situation of flexible confinement, we observe a split in the d_{gg} distances (red filled diamonds in Figure 2.1), at the same transition value of ρ_{2D} that occurs for the rigid walls. Upon closer inspection, and displayed in Figure 2.2, we observe the coexistence of an (n)-layer and an (n+1)-layer state in the same flexible system. The heat maps in Figure 2.2 show the position of water as a function of d_{gg} averaged over time. For the lowest density studied, where the strong graphene adhesion between the surfaces traps 1D pockets of ice, similar to the phenomena observed in [15].

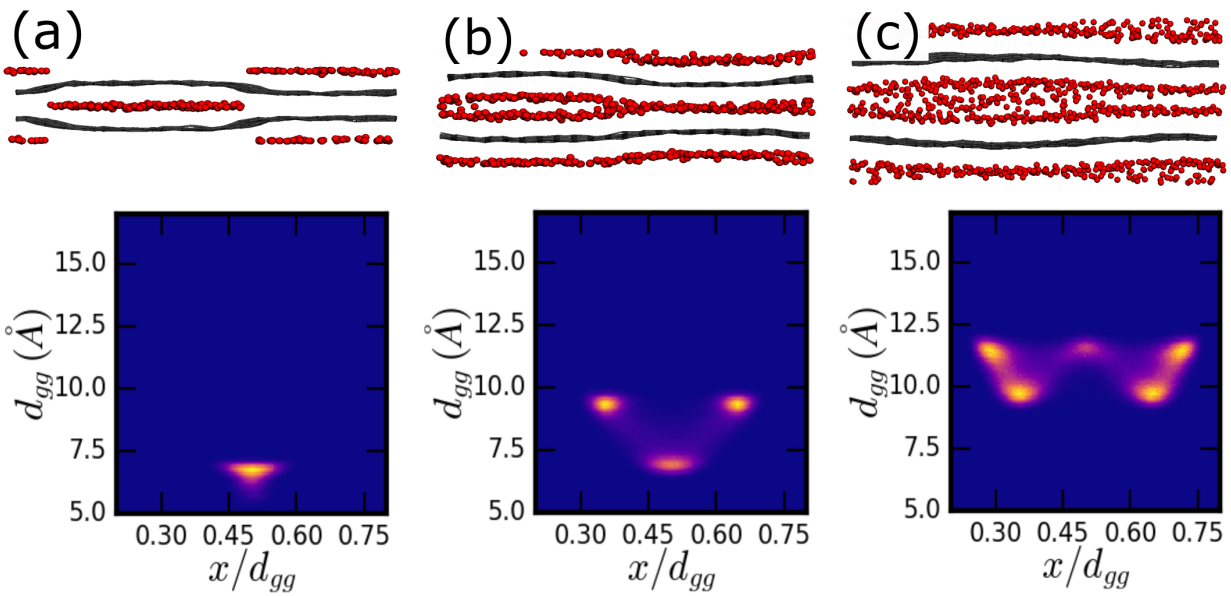

Figure 2.2: *Systems at the transition between multi-layered states for the case of flexible graphene sheets.* In the snapshots the oxygen atoms of the water are shown in red and the graphene atoms in grey. In the heat maps on the bottom, warmer colors correspond to a higher probability of finding a water molecule there. (a) 0L-ML, (b) ML-BL, (c) BL-TL.

The incommensurability of the systems is evidenced by a broadening of the density peaks, illustrated at the mid-transition point of ρ_{2D}= 0.245 for the BL-TL transition in Figure 2.3b. At the transition, the probability distributions reveal two broad peaks in the case of rigid confinement and a split to a BL/TL coexisting states in the case of flexible graphene walls. The confining distance for the rigid wall, d_{gg}= 10.14 Å, which falls between the local BL and TL d_{gg}values of the corresponding flexible system, which are 9.76 and 11.36 Å, respectively. In the case of the ML-BL transition, the system with rigid walls shows two sharp peaks (Figure 2.3a), which we will show later correspond to the formation of bilayer ice.

In-Plane Structural Order and Dynamics

Now, we study the structure and dynamics of water to assess the in-plane phase behavior in the commensurate states between the transitions, so that we can discern between ice, liquid, gas, or more complex phases such as glasses, heterogeneous liquids, or phase coexistence. For this purpose, we calculate the oxygen-oxygen pair correlation function $g_{OO}(r)$, the 3-body angle, θ, distributions between the oxygen atoms of coplanar water molecules, $p(\theta)$, and the lateral mean-squared-displacement, $\mathcal{D}_{||}$, for all the cases (see Methods). We start by analyzing the in-plane phase behavior in the ML regime, shown in Figure 2.4. For the lowest density investigated, ρ_{2D}=0.062, there is not enough water to form a full monolayer. In the rigid confinement case this leads to liquid-vapor coexistence, where the liquid phase is characterized by a relatively high diffusivity of $\mathcal{D}_{||}$=2.26 x 10^{-5} cm^2/s (Figure 2.4a), close to the

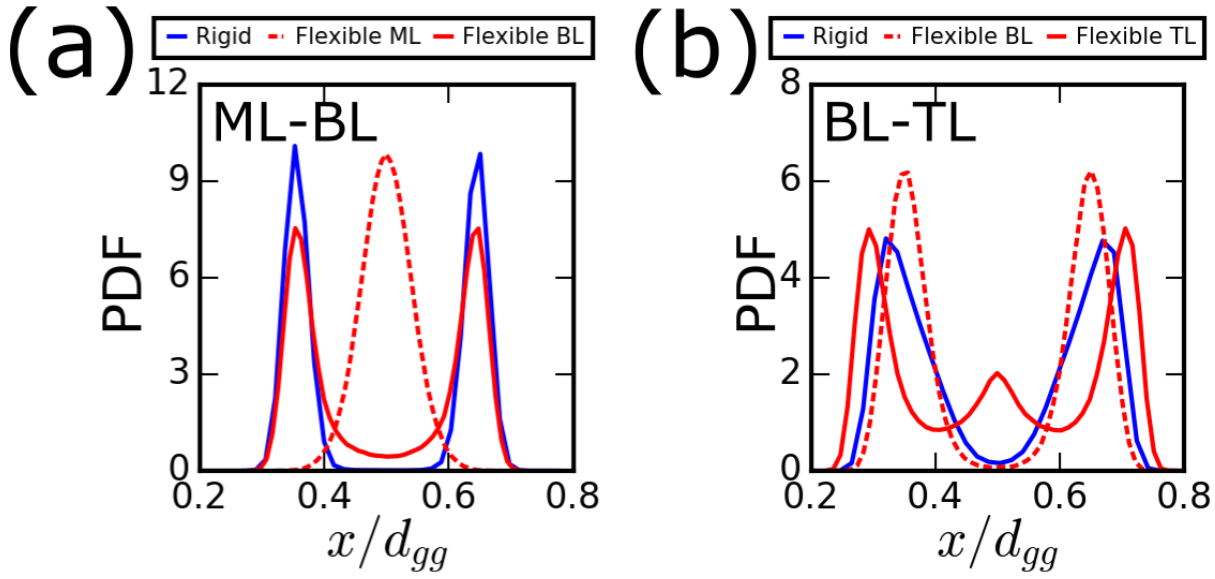

Figure 2.3: *Water density profiles comparing the ML to BL and the BL to TL transition for flexible and rigid cases.* (a) ML-BL transition. (b) BL-TL transition. Because the transition states for the systems with flexible walls correspond to coexisting states of (n)-layer and (n+1)-layer states, those are shown in the plots as dashed and full red lines, respectively.

value for bulk water. The ML liquid structure is best described as a highly defective tetrahedral network as seen in the $g_{OO}(r)$ and the very broad peak in $p(\theta)$ around the tetrahedral angle θ=104° as well as θ=160° [52]. By contrast, the flexible graphene system exhibits a coexistence of square and rhombic ices at the lowest density of ρ_{2D}=0.062, characterized by peaks in $p(\theta)$ at θ=90° and θ=160°, with a diffusivity that is 4 orders of magnitude smaller than observed for rigid walls (Fig 4b). The snapshot of the system reveals a region where there is no water, but unlike the rigid ρ_{2D}=0.062 system, this area is not a vapor region but a region of graphene-graphene contact (Figure 2.2a). When ρ_{2D} is increased to 0.092 and 0.123, the rigid graphene walls induce the formation of square and rhombic ice coexistence seen in the flexible case at the lower density, again supported by a structured $g_{OO}(r)$, bimodality in the $p(\theta)$ with peaks at θ=90° and θ=160°, and corresponding self-diffusion coefficients with nearly arrested values. At ρ_{2D}=0.092 the ice phases coexist with a vapor phase, while the vapor phase nearly vanishes at ρ_{2D}=0.123. By contrast, the flexible graphene walls induce a very different sequence as a function of increasing ρ_{2D} for the phases that are present. The confined flexible system exhibits a liquid-vapor coexistence that was observed for the rigid case, but at the higher density value of ρ_{2D}=0.092. At the highest ML density the flexible wall induces the square and rhombic ice phases, which was formed at the lowest ML density.

The results of the analysis for the BL states are shown in Figure 2.5a for water confined between rigid graphene walls. In contrast to the square and rhombic ice phases observed for ML, the BL exhibits hexagonal ice sheets that are stacked in phase, but with an abundance of

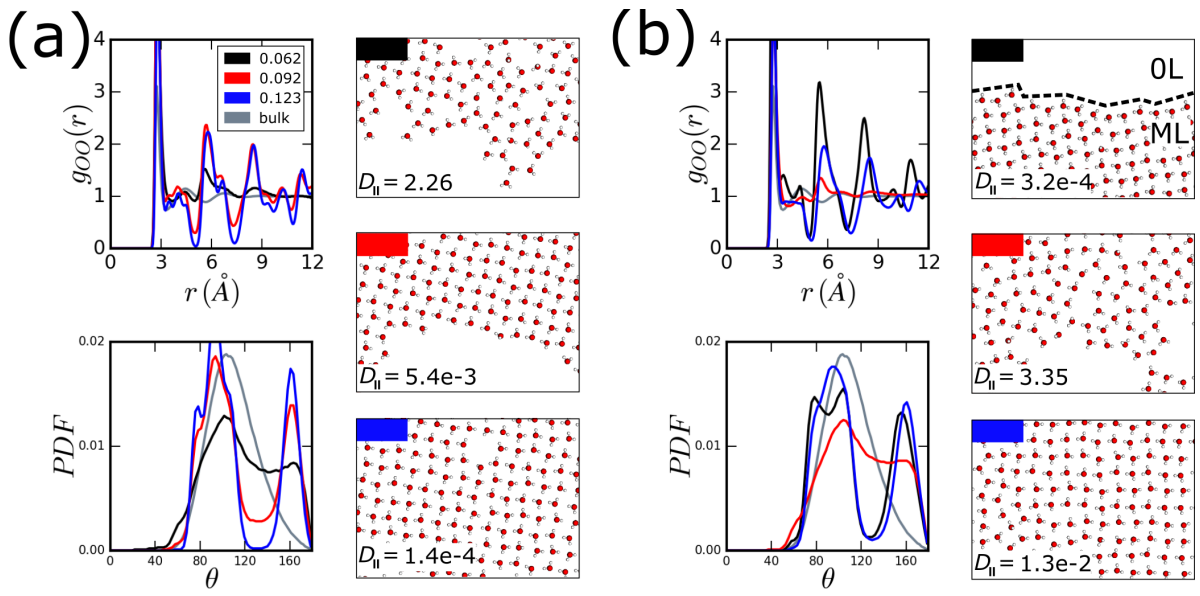

Figure 2.4: *Structure and dynamics, and phase behavior, of systems in ML regime.* (a) Rigid walls. (b) Flexible walls. Each panel shows the lateral oxygen-oxygen pair correlation functions, $g_{OO}(r)$, (top), and the three-body angle distributions, p(?), (bottom). Snapshots are also shown corresponding to the different cases, and the lateral diffusion coefficients, $\mathcal{D}_{||}$, are given in units of 10^{-5} cm^2/s. The separation between the 0L and the ML ice coexisting states shown in the first snapshot of panel (b) is illustrated by a black dashed line.

defects necessary to accommodate the nearly circular vapor-solid interface in the rectangular simulation box (Figure 2.5a). This is confirmed by the unimodal peak at $p(\theta)$ at θ=114° and the $g_{OO}(r)$ which exhibit a smooth oscillatory structure that is qualitatively different from the structure of square ice. As ρ_{2D} is increased to 0.215, the amount of water confined is too large to develop in-plane crystalline order, and the water adopts a liquid phase, with small patches of ice that nucleate and dissipate on the time scales of the simulation; these metastabilities suggest that we are very close to the solid-liquid phase transition. This effect is reflected in the slower than bulk self-diffusion coefficient ($\mathcal{D}_{||}$=1.07 x 10^{-5} cm^2/s), and in the shoulder at θ=160° in the $p(\theta)$ distribution.

For the systems with flexible walls (Fig. 2.5b), As we increase the 2D density to ρ_{2D}=0.154, a coexistence of a ML liquid and a BL liquid, as observed from simulation snapshots (Fig 2.2b). These coexisting liquid phases are structurally different, as confirmed by their $g_{OO}(r)$ and $p(\theta)$ plots, although both are generally classifiable as a highly defective tetrahedral network due to peaks at θ=60° and θ=160°. Although there are structural differences between the ML and BL regions of the system, the poorly aligned interface between the two liquids prevents any solidification of the ML component, and the resulting $\mathcal{D}_{||}$ is similar to the other BL liquid states. At the higher densities for the BL state, the system transitions to the liquid state alone, and very similar to that observed for rigid confinement, although the diffusivity is consistently higher in the flexible case. As we increase the density

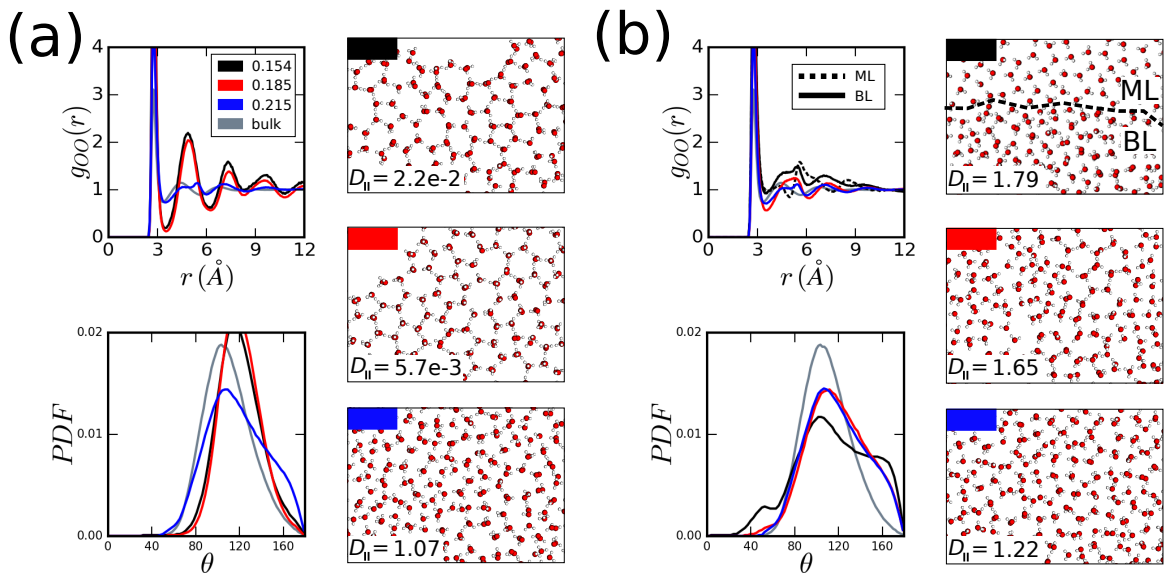

Figure 2.5: *Structure and dynamics, and phase behavior, of systems in BL regime.* (a) Rigid walls. (b) Flexible walls. Each panel shows the lateral oxygen-oxygen pair correlation functions, $g_{OO}(r)$, (top), and the three-body angle distributions, p(?), (bottom). Snapshots are also shown corresponding to the different cases, and the lateral diffusion coefficients, $\mathcal{D}_{||}$, are given in units of 10^{-5} cm^2/s. The separation between the ML and the BL ice coexisting states shown in the first snapshot of panel (b) is illustrated by a black dashed line.

beyond ρ_{2D}=0.245, the systems transition into the TL state. As the density is increased even further, the intermediate layer of water becomes thicker and more bulk-like, dominating the behavior of the system eventually at larger confining distances, in good agreement with previous studies [51]. In this case we find that the differences between rigid and flexible graphene walls are found to be minor except for the higher self-diffusion coefficients in the latter.

Conclusions

In this paper, we have shown that confinement effects in slit nanocapillaries depend strongly on the flexibility of the planar confining surfaces. We find that the transitions between different multi-layered states of nanoconfined water, although occurring at the same density values, are very different between systems with rigid and flexible walls. Remarkably, while the rigid systems exhibit sharp differences in the confinement distances at the transition incommensurate states, the flexible walls allow the system to spatially split into an (n)-layer and an (n+1)-layer coexisting states. This finding suggests that incommensurate states are energetically unfavorable, such that when the constraint of infinite rigidity of the confining surfaces is relaxed, the system splits into two commensurate states with a different number of layers. Although a similar coexisting state has been observed under imposed inhomogeneous

confinement [48], in this study the coexisting states are qualitatively different because we do not impose any inhomogeneity in the system. Furthermore, within the same multi-layer state, the flexible walls introduce a very different sequence of ice phases and phase co-existence with vapor and liquid phases than that observed with rigid walls. The differences can be dramatic. For example, in the BL state, an hexagonal ice phase forms in the case of rigid walls, but a liquid phase forms instead in the case of flexible confining surfaces. Because flexible interfaces are widely present in both technological and biological processes, it is of critical importance to understand nanoconfinement effects in the phase behavior of water under realistic conditions, beyond the idealized confinement conditions of infinitely rigid walls. This work is a step forward in that direction.

Acknowledgements

LRP and THG acknowledge support from the Director, Office of Science, Office of Basic Energy Sciences, Chemical Sciences Division of the U.S. Department of Energy under Contract No. DE-AC02-05CH11231. LF was supported by the National Science Foundation Graduate Research Fellowship under Grant No. DGE 110640. This research used resources of the National Energy Research Scientific Computing Center, a DOE Office of Science User Facility supported by the Office of Science of the U.S. Department of Energy under Contract No. DE-AC02-05CH11231.

Computational Methods

The model system consists of two parallel graphene sheets with water molecules filling the two interlayer spacings at a prescribed density ρ_{2D}. The confinement occurs in the x-direction, and the in-plane dimensions of the system are L_y = 46.2 Å, and L_z = 48.5 Å. Periodic boundary conditions are applied in all dimensions. We use the TIP4P-Ew model of water [53], and the parameters for graphene have been adapted from previous works [37, 54]. All the bonded parameters are summarized in Appendix Table 2.1, and the non-bonded parameters in Appendix Table 2.2.

All the simulations were performed with the LAMMPS software package [55] found at http://lammps.sandia.gov. We use a time step of 2.0 fs for all the simulations, and all the simulations are performed at T = 298 K. We use the RATTLE algorithm [56] with a tolerance of 10^{-4} to keep the water molecules rigid. First in order to relieve close contacts or other high-energy configurations in the system, we run Brownian dynamics [57] for 10 ps where we limit the atoms displacement in a single time step to 0.1 Å. Subsequently we simulate the system in the NVT ensemble for another 10 ps using a Nose-Hoover extended Lagrangian procedure [58] with a temperature damping parameter of 0.1 ps. Finally we perform 10 ns simultions in the NPT ensemble, where only the x-direction (i.e. the direction of confinement) is allowed to fluctuate, P_{xx} = 0.1 MPa, and the temperature and pressure

control were implemented using Nose-Hoover extended with characteristic damping times of 0.1 ps and 1.0 ps, respectively. We consider the first 3 ns equilibration, and we collect data for analysis every 500 steps (2 ps) over the last 7 ns of the NPT trajectories. In the rigid cases, the graphene sheets are kept rigid but their center of mass position can fluctuate. In the flexible cases the full force-field is employed without further constraints. To calculate $g_{OO}(r)$ [52], the oxygen atoms were histogrammed into 0.6 Å bins according to their x-coordinate. Within each bin, the distances between all oxygen pairs were histogrammed and normalized by the area of each bin:

$$g_{\text{lateral}}(r) = \frac{A}{\pi r N^2} \left\langle \sum_i \sum_{j \neq i} \delta(r - r_{ij}) \right\rangle \tag{2.1}$$

For the 3-body angle distributions, $p(\theta)$, the angle θ is the angle between the central oxygen and the first and second nearest neighbors within the same bin. The lateral MSD is computed as follows:

$$\text{MSD}_{||} = \langle r_{YZ}^2 \rangle = \frac{1}{N} \sum_{i=1}^{N} \left(r_{i,YZ}(t) - r_{i,YZ}(0) \right)^2 \tag{2.2}$$

We estimate the lateral diffusion coefficient, $\mathcal{D}_{||}$, from the lateral MSD using Einstein's relation, $\langle r_{YZ}^2 \rangle \propto 4\, t\, \mathcal{D}_{||}$.

Appendix

bonded term	**parameters**		
Bond	K_b ($kCal/mol/\text{Å}^2$)	b_0 (Å)	
	938.0	1.40	
Angle	K_θ ($kCal/mol/rad^2$)	θ_0 (degrees)	
	126.0	120.0	
Improper	K_{im} (kCal/mol)	χ_0 (degrees)	
	15.0	0.0	
Dihedral	K_{di} (kCal/mol)	n (multiplicity)	ϕ (degrees)
	3.150	2	180.0

Table 2.1: *Force field bonded parameters used for graphene in confined water simulations.*

atom type	**partial charge (e)**	σ **(Å)**	ϵ **(kCal/mole)**
Graphene carbon	0.0000	3.55	0.07
Water oxygen	-1.0484	3.16435	0.16275
Water hydrogen	0.5242	0.00000	0.00000

Table 2.2: *Force field parameters used for each atom type in confined water simulations.*

Chapter 3

Role of Hydrophilicity and Length of Diblock Arms for Determining Star Polymer Physical Properties

We present a molecular simulation study of star polymers consisting of 16 diblock copolymer arms bound to a small adamantane core, by varying both arm length and the outer hydrophilic block when attached to the same hydrophobic block of poly-δ-valerolactone (PVL). Here we consider two biocompatible star polymers in which the hydrophilic block is composed of polyethylene glycol (PEG) or poly-methyloxazoline (POXA), in addition to a polycarbonate-based polymer with a pendant hydrophilic group (PC1). We find that the different hydrophilic blocks of the star polymers show qualitatively different trends in their interactions with aqueous solvent, orientational time correlation functions, and orientational correlation between pairs of monomers of their polymeric arms in solution, in which we find that the PEG polymers are more thermosensitive compared to the POXA and PC1 star polymers over the physiological temperature range we have investigated.[1]

Introduction

Star polymers are globular nanoparticle architectures in which linear polymer "arms" are connected to a central polymer core. Recent advances in the ease of their synthesis has created the possibility of realizing a large combinatorial variation in the structure and function of these nanoparticles through the patterning of chemical functional groups and/or the length

[1]Reproduced from [59] with permission.

of the polymeric arms [18, 19]. However, synthetic advances made on star polymers have far out-paced the corresponding physical characterization of their structural, thermodynamic, or dynamical properties, and thus the ability to rationally navigate the vast chemical landscapes of possibilities for creating a useful star polymer. For example, a particular functional goal is to develop a star polymer capable of serving as a molecular drug-delivery vehicle, which therefore adds additional design restraints for safe performance under physiological conditions of temperature and aqueous solvent [60]. In a recent paper, some of us have performed all atom explicit solvent molecular dynamics simulations of three different star polymeric systems in water at physiological temperatures [61]. In this previous star polymer comparison, the diblock arms consisted of an inner "hydrophobic" block which was varied in the three systems to be either polylactide, poly-δ-valerolactone (PVL), or polyethylene, while holding the outer hydrophilic block fixed to the same polyethylene glycol (PEG) polymer that is widely used as an in vivo biomaterial. (We note that PEG versus PEO is a matter of size, with smaller MW polymers being referred to as PEG while larger ones are called PEO, with a cutoff that is usually around 20,000 Daltons; we are below this threshold and hence refer to them as PEG star polymers). It was determined that the hydrophobic regions of these systems were very glassy, but it was speculated that this could be an artifact that is due to the small and structured adamantane core to which they are directly attached, and perhaps the small sizes of star polymers that were simulated. Furthermore, a sharp boundary existed between the hydrophobic cores and outer block of water solubilized PEG at low temperatures, although solubility as measured by surface area contact of the polymer arms with water decreased as the temperature was increased. This might suggest the presence of a lower critical solution temperature (LCST) for the PEG star polymer, which is known to exist for linear PEG-water mixtures [62], suggesting that through design such polymers could be thermally responsive in a temperature regime useful for physiological applications.

Here we present a comparative simulation study of how the physical properties of the model star polymers change by now holding the inner hydrophobic PVL block (attached to the adamantane core) fixed, but now varying the outer block hydrophilic monomer as either PEG, poly-methyloxazoline (POXA), or a polycarbonate-based polymer with a pendant hydrophilic group (PC1). The introduction of POXA adds additional hydrogen bonding sites beyond the basic PEG ester group, while PC1 adds yet an additional feature of polymer branching. We also compare doubling the length of the hydrophobic PVL block to assess possible artifacts introduced by the adamantane core, as well as significantly elongating the hydrophilic blocks compared to the previous study. These new comparisons of chemical features and size are explored to understand what drives star polymer thermally induced structural changes, especially in regards to questions on how cargo is held or released, or the exposure of sites to hydrolysis reactions that promote biodegradation, all of which are important factors relevant to their suitability as a drug delivery material.

Methods and models

Molecular systems

Each of the polymer systems was created by connecting 16 diblock polymer arms to a central adamantane molecule. Adamantane, $C_{10}H_{16}$, is comprised of 10 carbon atoms in a diamond lattice structure. Each hydrogen site of the adamantane was removed and used as a connection site for the hydrophobic end of a diblock arm. The hydrophobic chain was connected to a hydrophilic chain, completing the diblock arm. Each of the four polymers studied had the same hydrophobic region chemistry of a block polymer created from the monomer δ-valerolactone, which will be referred to as PVL. The varying hydrophilic regions were designed to represent a range of molecular features including various degrees of hydrogen-bonding and branching, as well as arm length variation. Figure 3.1 provides an example of the representative features of the diblock star polymers evaluated here.

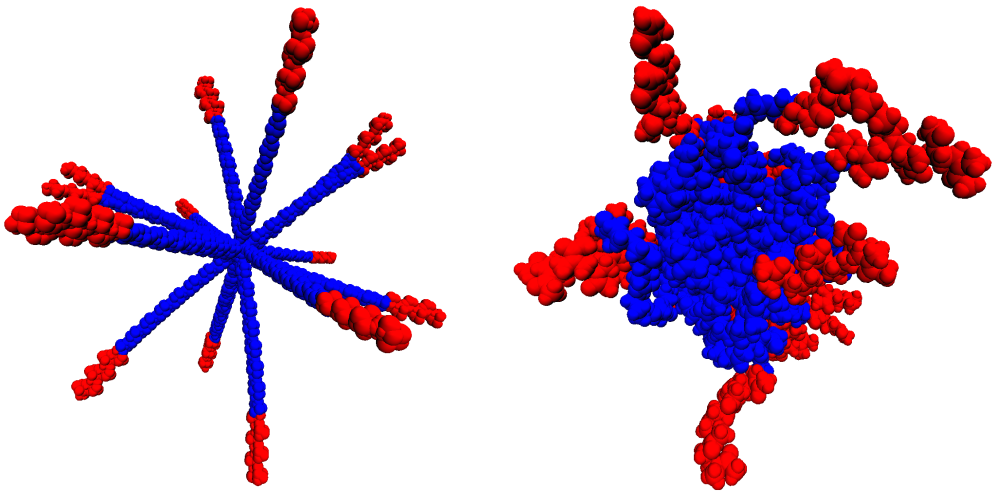

(a) **(b)**

Figure 3.1: *Visualization of star polymer* (a) Depiction of the generic diblock star polymer nanoparticle structure when fully extended showing: adamantane core region (yellow), inner hydrophobic polymeric block (blue), and outer hydrophilic polymer block (red). (b) Depiction of the generic star polymer in a partially collapsed state, with same color scheme as (1a). Please note that (a) and (b) are not on the same scale

The arm chemistry of the first polymer consists of eight units of PVL connected to a hydrophilic region of six repeat units of ethylene oxide to form PEG; it will be referred to throughout the paper as PVL_8PEG_6 or S-PEG (S for short). This nomenclature refers both to the arms that make up the star polymer as well as to the star polymer made from those arms. The second polymer consists of eight units of PVL connected to a hydrophilic region of six repeat units of dimethylacetamide to form poly-oxazoline, POXA; experimentally, the polymer POXA is created from a ring-opening polymerization of the compound oxazoline, which is the origin of its name. It will be referred to throughout the paper as PVL_8POXA_6

Star Polymer	**Name**	**Hydrophilic region region**	**Ext. len. (Å)**	**No. star atom**	**No. water**
$A[PVL_8\text{-}PEG_6]_{16}$	S-PEG	PEG=(-CH_2-O-CH_2-)	78	2618	45702
$A[PVL_8\text{-}POXA_6]_{16}$	S-POXA	POXA=(-CH_2-N(COCH_3)-CH_2-)	81	3194	45483
$A[PVL_{16}\text{-}PEG_{24}]_{16}$	L-PEG	PEG=(-CH_2-O-CH_2-)	199	6554	44285
$A[PVL_{16}\text{-}PC1_{12}]_{16}$	L-PC1	PC1=(-CH_2-OCOO-CH_2-C(CH_3)R-) R = (-CO-NH-CH_2-CH_2-OH)	204	9050	43058

Table 3.1: *Chemical composition of star polymers studied.* All star polymers have the same hydrophobic block polymer chemistry of PVL = (-CH_2-CH_2-CO-O-CH_2-) that is attached to the adamantane core on one end and the hydrophilic block chemistry on the other end, in which the hydrophilic chemistry varies between the star polymers studied. The extension length corresponds to the idealized length of the star polymer arm when torsions are set to 180, which were first collapsed in vacuum and then in aqueous solvent. The collapsed star polymers were then simulated with the amount of solvent yielding somewhere between 4-8 solvation layers around the polymer.

or S-POXA. The number of monomer units of the hydrophilic regions of PVL_8PEG_6 and PVL_8POXA_6 were selected to yield approximately equal arm lengths when the two star polymer arms are fully extended. The third polymer is chemically related to the first, comprised of sixteen units of PVL connected to a hydrophilic region of twenty-four repeat units of ethylene glycol; it will be referred to throughout the paper as $PVL_{16}PEG_{24}$ or L-PEG (L for long). The fourth polymer is also composed of longer arms, comprising sixteen units of PVL connected to a hydrophilic region of twelve repeat units of a functionalized methyl propyl carbonate to form the polymer PC1; it will be referred to throughout the paper as $PVL_{16}PC1_{12}$ or L-PC1. Again, the number of monomer units of the hydrophilic regions of $PVL_{16}PEG_{24}$ and $PVL_{16}PC1_{12}$ were selected to yield approximately equal arm lengths when the two star polymer arms are fully extended. A summary of each polymer and their monomeric chemical structure is given in Table 3.1.

Force fields

The force fields used for water, PVL, and PEG have been described thoroughly in a previous publication [60, 61], which we briefly summarize here. We used the TIP4P-Ew [53] as the model for aqueous solvent in all simulations performed in this study. For the adamantane core and the linkage of adamantane to the hydrophobic chain of PVL, OPLS-AA parameters [63] were used but with improved parameters of Price et al. [64] for the alkane torsion angle energy expressions. Our previous study carefully reparameterized the charge model and C-C-O-C and O-C-C-O torsions for PEG to be suitable for aqueous solvation studies [61].

These modified OPLS parameters were derived from QM calculations and then validated on Raman spectra for DME.

For the polyoxazoline segments of each arm, the repeat unit is -CH_2-N(CO-CH_3)-CH_2- with parameters expected to be like those for N,N-dimethylacetamide, but with charges modified so that repeat units are charge neutral. For polyoxazaline chains, the OPLS-AA atom types are -CT-N-CT along the backbone, with HC as the atom type for hydrogen on backbone carbon aliphatic CT sites, and N (amide) for the nitrogen. The polyoxazaline side chain is a methoxy group (-CO-CH_3) with OPLS-AA atom types C and O for the carbonyl group and CT and HC for the terminal methyl sites. Charges are +0.06 for all HC sites and +0.06 for the backbone CT sites; the N sites have charge -0.36; C of the carbonyl groups have charges of +0.60 and O of the carbonyl groups have charges of -0.60; CT on methyl groups at the end of the sidechains have charges of -0.18. At the end of each arm, there is a terminal methyl group with a charge on the carbon sites set to 0.00; the three hydrogen atoms on that site make the last repeat unit charge neutral. Bond, angle and torsion parameters for the polyoxazoline segment were OPLS-AA parameters from the literature [63–71], and especially from Price, et al. [64], who report parameters for esters and hydrocarbons. The parameter set did not include parameters for torsions with atom types CT-N-CT-CT, so values for type CT-N-CT-HC were substituted. For linkages between the polyoxazoline and polyvalerolactone segments, parameters for ethyl propanoate were used from Price, et al [64]. OPLS-AA parameters in the current literature also do not include parameters for torsions with atom types N-CT-CT-N, so values for NT-CT-CT-NT (NT for amine nitrogen) were substituted.

The repeat units on the PC1 hydrophilic segments are -CR(CH_3)-CH_2-O-CO-O-CH_2- and the side chain on each repeat unit is R=-CO-NH-CH_2-CH_2-OH. Propylmethyl carbonate (PMC) and dimethyl carbonate (DMC) were studied as model molecules for the determination of parameters for the repeat units along the polycarbonate backbone for the hydrophilic segment. OPLS-AA atom types for the carbonate were chosen to be similar to esters, namely CT for the methyl and propyl aliphatic carbon sites, HC for the corresponding hydrogen sites; OS for the ether-type backbone oxygen sites, C for the backbone carbonyl carbon and O for the carbonyl oxygen. These OPLS-AA atom types determine the Lennard-Jones parameters and most of the bonded parameters (bond, angle and torsion parameters) consistent with those for esters.

Charges for the carbonate group sites were taken from an analysis of charges used for DMC by other force fields, from ESP fits to electrostatic potentials produced from gas phase quantum chemical calculations, as well as solution phase (PCM) quantum chemical calculations using continuum representations of either liquid water or dimethyl carbonate (DMC), with a dielectric constant of approximately 3, as solvent. The quantum chemical approach was based on structures optimized using MP2 (aug-ccpVTZ), after which B3LYP DFT calculations were performed using PCM models for the solvent. Electrostatic potentials were fitted using software developed in house at IBM that supports constraints on total charge as well as to establish charge equivalence among sets of sites. Although there were small variations among methods, the results were surprisingly consistent. Moreover, there

	OPLS (ester)	**ESP (water)**	**ESP (DMC)**	**Soetens**	**This work**
C (carbonyl)	+0.510	+0.997	+0.963	1.0864	1.000
O (carbonyl)	-0.430	-0.666	-0.633	-0.6774	-0.586
-O- (alkoxy)	-0.330	-0.433	-0.414	-0.4478	-0.414
-C(H2)- (alpha)	+0.190	+0.007	-0.003	-0.1561	+0.105
HC (alpha)	+0.030	+0.087	+0.084	+0.1331	+0.051

Table 3.2: *Comparison of charge models for esters using OPLS-AA and for DMC using various approaches.* All charges are in electron units. Soetens charges [72], included for comparison, are fits to electrostatic potentials of lowest energy structure from their HF-SCF (6 - 31G**) calculations. The Soetens charges were also used in the work of Gontrani, et al.

was not much change in these charges as a function of the OCOC torsion angle. Consistency of charge model with respect to solvent environment and molecular structure suggests that a fixed charge model for carbonates might be adequate for many purposes.

For use in polymeric material we required a charge model that produced charge neutral groups and could be used in the context of material described by other OPLS-AA parameters. The charges in Table 3.2 for DMC are the result. These result in a charge of -0.414 for the -O-CO-O- carbonate functional group, which is then balanced by net charges of +0.207 on the alpha methylene groups on each side of it. These methylene groups have a charge of +0.105 on the (CT) carbon sites and +0.051 on the (HC) hydrogen sites. Changing the number of hydrogen sites bonded to this alpha carbon would change its charge by 0.051 for each hydrogen added or removed in order to maintain a net charge of +0.207 on groups alpha to the carbonate. Although the local charge density on the carbonyl group is more polar than for esters, the rest of the charges are similar. Simulations of pure liquid DMC using these parameters (not shown) give adequate densities.

Given this charge model and ester-like atom types, all of the Lennard-Jones, bond and angle parameters and most of the torsion parameters for a polycarbonate backbone can be found in the OPLS force field literature. There are a few exceptions. Angle terms involving OS-C-OS bending were missing. We used an equilibrium angle of 113.2 degrees to be compatible with the O-C-OS equilibrium angle of 123.4 degrees, in order to allow the four sites of the carbonate region to lie flat. A few torsion parameters were missing: for CT-CT-CT-OS we substituted parameters for CT-CT-CT-CT, since these have similar multiplicity and barrier height. For torsions involving atom types CT-OS-C-OS, we used parameters developed by Gontrani, et al. [73], for their modeling of DMC. This energy term produces a barrier that helps the molecule maintain the preferred trans-trans conformation, i.e., a ẅshape, over the cis-trans form. Note that starting from OPLS-AA parameters, Gontrani, et al. [73] made other modifications, but we are using only their torsion parameters for this particular torsion type.

For polycarbonate chains beyond DMC, a very important torsion is that described by CT-CT-OS-C, since this is the first "floppy" torsion beyond the relatively rigid DMC (CH_2-O-CO-O- CH_2-) group within a polycarbonate polymer. Parameters exist for this kind of torsion energy term in the OPLS-AA force field for esters groups. We used these parameters with the OPLS-AA atom types, the charge model and modifications described above, to produce an energy curve as a function of torsion angle from a series of constrained optimizations on propyl methyl carbonate, where each optimization was performed with a different constrained value of the CT-CT-OS-C torsion angle. The resulting energy curve showed three nearly degenerate minima, one at the expected value of 180 degrees (trans), and two others near +/-80 degrees, with a barrier between them of about 1 kcal/mole. This energy curve was compared with a similar one produced from calculations performed in the gas phase using an MP2/auc-ccpVTZ level of theory (Figure 3.2). The quantum calculations showed the trans structure to be the most stable, but with two very shallow minima (almost shoulders) at +/-90 degrees, and they were 1.5 kcal/mole higher in energy than the trans structure. We felt compelled to fix this error in our version of the force field since the presence of these two spurious minima would affect the persistence length and conformational preferences of the polycarbonate chains. Therefore, we developed new parameters for the CT-CT-OS-C torsion by fitting to the quantum result. The resulting three term fit, U(phi)=0.3693 *(1+cos(phi)) + 0.2342*(1-cos(2*phi)) + 0.1315*(1+cos(3*phi)) (all units are kcal/mole) did an excellent job at reproducing the quantum energy curve.

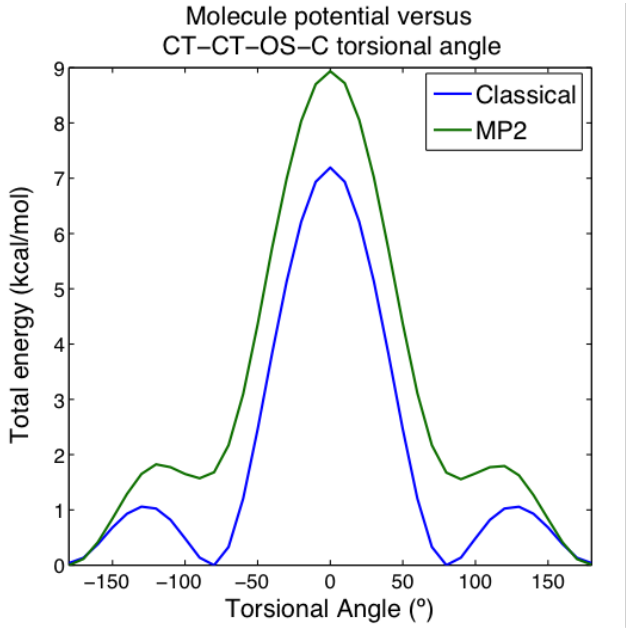

Figure 3.2: *Total molecule energy as a function of CT-CT-OS-C torsional angle estimated by both classical and quantum (MP2) methods.* Classical results are generated using OPLS-AA parameters.

The hydrophilic sidechain attached to the carbonate backbone consists of an amide group, a short ethyl chain and an alcohol group. OPLS-AA parameters for these chemical groups

are well established since they are components of peptides and other well studied organic molecules. OPLS-AA atom types and charges are C (carbonyl Carbon, +0.5), O (carbonyl Oxygen, -0.5), N (amide Nitrogen, -0.5), HN (amide hydrogen, +0.3), CT (+0.08) and HC (+0.06) for the methylene group near the amide, CT (+0.145) and HC (+0.06) for the methylene near the hydroxyl group, and OH (-0.683) and HO (+0.418) for the hydroxyl group. Note that the side chain is charge neutral. OPLS-AA parameters for the Lennard Jones and bond terms for the side chain are from the literature.

Simulation Protocol

The initial configurations for all four star polymers were developed with in-house software. The star polymers are created in a fully extended state, with end-to-end distances as long as 204 Å. These extended structures were partially collapsed in vacuo after a short energy minimization, in which the collapsed structures ranged from 48 to 70 Angstroms in diameter. A cubic box of 46,656 TIP4P-Ew [53] water molecules was prepared and equilibrated using locally developed software and a protocol previously described6 with a control temperature of 300 K and an external pressure of 1 atm. A set of bulk water coordinates was obtained from the resulting simulation (box edge length 111.9453 Å) representing an instantaneous density of 0.9949 g/cm^3, in excellent agreement with experimental values.

The starting conformation for the simulations of solvated star polymers was constructed as follows: (1) The coordinates of the partially collapsed star polymer sites were translated so that the center of geometry was at the center of the cubic box from the water simulation. (2) For each water molecule, the smallest distance from any of its three sites to any of the polymer sites was computed. (3) Using these distances, water molecules were removed from the simulation, beginning with the closest water and then the second closest and so on, until the total mass of the removed water molecules just exceeded the total mass of the star polymer. Depending on the size and type of star polymer, between 954 and 3,598 water molecules were removed by this procedure. By construction, each solvated star polymer system has the same volume and nearly the same mass, hence the same mass density, as that of water. With the closest water molecules removed in this way, dynamical simulations could be started without any additional preparation.

Simulations were performed using a version of the LAMMPS software [55] dated April 2012. Molecular dynamics simulations were performed on an IBM BlueGene/L supercomputer and on the NERSC supercomputer Carver, and the analysis of the resulting trajectory data was performed on a local cluster in the Head-Gordon lab. Each system was simulated at 300 K, 350 K, 400 K and 450 K, and at 1 atm pressure in the NPT ensemble, or for an NVT ensemble run that was equilibrated in the NPT ensemble at 1 atm. First, thermal equilibration was performed, which for the larger star polymer systems were as long as 50 ns. During equilibration, the partially collapsed star polymer structure collapsed further, and for each system, there were at least 20 Å between sites on neighboring images of polymers in the periodic system, i.e. ~ 6 or more intervening water layers to reduce direct interaction

between copies in different periodic images. After equilibration, production simulations for each of the systems at each given temperature were at least 50 ns.

All simulations were performed using an NVT or NPT ensemble, with thermal control implemented using a Nose-Hoover extended Lagrangian procedure, with a fictitious mass set so as to establish a fluctuation period [58] of approximately 100 fs in the thermostat variable (known as the thermostat damping factor in LAMMPS). The dynamical integration scheme was velocity-Verlet [74] with a timestep of 1 fs. All bond lengths involving hydrogen, as well as the HOH angle for the TIP4P-Ew model were constrained using a SHAKE [56] procedure, to guarantee that the bond length constraints were satisfied to a tolerance of 10-5 Å. Lennard-Jones interactions and direct space electrostatic interactions were truncated at 9.0 Å, and a tail correction for the Lennard-Jones potential beyond this cutoff was included in energy/force and virial pressure calculations. Electrostatic interactions were evaluated with a particle-particle-particle mesh (PPPM) procedure [75] with an accuracy parameter (10^{-5}) that resulted in a 3D k-space grid of 120-by-120-by-120. In accordance with OPLS-AA potential, neither Coulomb nor Lennard-Jones interactions are evaluated for particle pairs that are 1-2 and 1-3 interactions, and both of these interactions are scaled by a factor of 0.5 for 1-4 interactions. Geometric combining rules were used to establish the Lennard-Jones parameters.

Table 3.3 reports the simulation conditions for each star polymer. For S-POXA (300K, 350K, 400K), L-PEG (350K, 400K), and L-PC1 (350K), the star polymers-water systems were simulated in the NPT ensemble at 1 atm to define an average density, which was then used to set the volume for the production run in the NVT ensemble. The S-PEG system was taken from a previous simulation study [61] that was simulated in the NVT ensemble; in this previous work, the large water box was equilibrated in the NPT ensemble, and then the average volume was set for the NVT run and the star polymer was added (by deleting waters). Although the pressure is higher, we do not expect it to be more than 10 atm. Because water is so incompressible, the PV term between 10 atm and 1 atm is tiny, ~ 0.005 kcal/mole $\ll k_BT$, and thus it will have a negligible effect on results. In addition, our study covers a range of temperatures, including high temperatures to improve sampling, although these temperatures are above the boiling point of the water model. As a precaution we set the pressure to 10 atm for the L-PEG at 450K and L-PC1 at 400K and 450K, but this will not significantly impair the comparisons to 1 atm as explained in above. After the 50 ns of equilibration, production simulations for each of the systems at each given temperature were at least 50 ns (Table 3.3).

Previous work by Huynh et al. simulated for at least 200 ns per star polymer system at 300K in which they found that most observables were stable after about 15 ns of sampling [76]. Since we are concerned that our systems may be sluggish at 300K for the large polymers, we also considered higher temperatures (350 K, 400 K, and 450 K) to sample more adequately due to the shorter correlation times at these temperatures. All of our results below show stable and systematic trends with temperature, and the uncertainty estimates we have plotted appear to be realistic. Thus we are certain that our simulation timescales are adequate.

Star Polymer	Ensemble	Pressure (atm)	Temp (K)	Mass density (g/cm^3)	Production Time (ns)
$A[PVL_8\text{-}PEG_6]_{16}$	NVT	-	300	0.9949	57.5
$A[PVL_8\text{-}PEG_6]_{16}$	NVT	-	350	0.9949	54.5
$A[PVL_8\text{-}PEG_6]_{16}$	NVT	-	400	0.9949	53.5
$A[PVL_8\text{-}PEG_6]_{16}$	NVT	-	450	0.9949	59.5
$A[PVL_8\text{-}POXA_6]_{16}$	NPT	1	300	0.9982	48.8
$A[PVL_8\text{-}POXA_6]_{16}$	NPT	1	350	0.9704	53.8
$A[PVL_8\text{-}POXA_6]_{16}$	NPT	1	400	0.9279	56.6
$A[PVL_8\text{-}POXA_6]_{16}$	NVT	-	450	0.9296	64.7
$A[PVL_{16}\text{-}PEG_{24}]_{16}$	NPT	1	350	0.9734	53.4
$A[PVL_{16}\text{-}PEG_{24}]_{16}$	NPT	10	400	0.9308	51.3
$A[PVL_{16}\text{-}PEG_{24}]_{16}$	NPT	10	450	0.8749	54.0
$A[PVL_{16}\text{-}PC1_{12}]_{16}$	NPT	1	350	0.8925	54.0
$A[PVL_{16}\text{-}PC1_{12}]_{16}$	NPT	10	400	0.8885	50.4
$A[PVL_{16}\text{-}PC1_{12}]_{16}$	NPT	10	450	0.8367	57.6

Table 3.3: *Simulation details for star polymer systems.*

Analysis

During the simulation runs, the coordinates of all atoms in each system were recorded every 40 picoseconds, allowing for approximately 1250 snapshots for post-processed analysis. As with the previous study [61], structural analysis was performed using in-house software on each star polymer using a variety of shape descriptors, radially averaged mass density, dynamical descriptors, including time orientational autocorrelation functions, and molecular shape information [77] derived from the eigenvalues of the gyration tensor, such as the radius of gyration and anisotropy. When ordered by magnitude from largest (λ_1) to smallest (λ_3), the radius of gyration (R_g), the asphericity (A_{sp}), the acylindricity (A_{cyl}) and anisotropy (A) are computed as follows:

$$R_g = \sqrt{\lambda_1^2 + \lambda_2^2 + \lambda_3^2} \tag{3.1}$$

$$A_{sp} = \lambda_1 - \frac{\lambda_2 + \lambda_3}{2} \tag{3.2}$$

$$A_{cyl} = \lambda_2 - \lambda_3 \tag{3.3}$$

$$A = \sqrt{\frac{A_{sp}^2 + \frac{3}{4}A_{cyl}^2}{R_g^2}} \tag{3.4}$$

A molecule-centered frame of reference was defined from the adamantane core, allowing the polymer system to be characterized without the effect of overall star polymer molecular rotation affecting calculations; thus for each coordinate set, the polymer site vectors and orientations were computed with respect to the molecule-centered reference frame.

Voronoi analyses, as described in the previous study [61], were also performed for each system. A Voronoi analysis [78, 79] uses the Cartesian coordinates of every molecule in the system to construct a set of polyhedra, one surrounding each molecule, that collectively fill the volume of the system. The space enclosed by a molecule's associated polyhedron is closer to that atom that to any other in the system. Polyhedron features shared by multiple polyhedra (faces, edges and vertices) thus represent points equidistant to the molecules corresponding to the polyhedra containing those features. Voronoi analyses are conducted using no additional information besides the Cartesian coordinates of the molecules. However, all the atoms in the system were partitioned into different classes (representing molecular identity, chemical nature, etc.). This allowed us to calculate the volume filled by each class (by summing the volumes of all the polyhedra corresponding to atoms in that class) and the interfacial area between different classes, since neighboring molecules can be easily identified because their associated Voronoi polyhedra share a face. For example, water molecules were grouped into clusters with each cluster representing a contiguous set of neighboring polyhedra, in which the largest of these clusters represents the bulk solvent, while all remaining clusters represent water molecules that have penetrated the interior of the polymer. Similar definitions can be defined for the hydrophobic and hydrophilic segments of the star polymer arms. Because each star polymer was comprised of different chemistry, their total accessible surface areas were not directly comparable. To correct for this fact, a normalization scheme was developed, wherein a fully extended polymer was solvated and initial surface contact areas were calculated between water and each region of the polymer. This number was averaged across all sixteen arms and used as a normalization factor. By normalizing each interfacial area, we could directly compare interfaces between polymers on a range from zero to one. In Table 3.4, we have reported the normalization factor for each component of the star polymers examined in this paper.

Orientational time correlation functions (OTCF) were computed as follows, and also as described in the previous study [61]. First, a local orientational unit vector, u, was defined for each monomeric unit on each arm of each star polymer. These vectors were directed between specific pairs of atomic sites on each monomeric unit. For PVL the vectors were

Polymer region	Normalization factor (Å²)	Uncertainty (Å²)
PVL_8	1224.7	17.9
PVL_{16}	2471.6	52.8
PEG_6	413.2	9.7
PEG_{24}	1742.7	30.0
$POXA_6$	708.9	15.5
$PC1_{12}$	3217.3	41.2

Table 3.4: *Factors utilized in normalization of polymer regions for use in Voronoi interfacial analysis.* Normalization factors were created from a fully extended and solvated star polymer of 16 arms. A Voronoi analysis was performed on the extended structure for each star arm to obtain the total interfacial area between water and each star arm. This value was then averaged to obtain a normalization factor. All uncertainties are ±1 standard deviation.

directed between an alkoxy oxygen site and the first carbon site immediately opposite the nearest carbonyl group. For PEG, the vectors were directed between pairs of carbon sites, the first and third heavy atoms of each PEG monomer. (Only three vectors were selected within the six-unit PEG part of the chain.) For POXA and PC1, orientational vectors were directed between the first and last heavy atom (non-hydrogen) along the polymer's backbone. Second, for each saved set of coordinates, these vectors were measured and projected from the lab frame onto the molecule-centered reference frame. Third, the time evolution of these vectors in the molecule frame was determined at 40 ps resolution over the 50 ns of the production simulations, and then an autocorrelation function ($\langle u(0) \cdot u(t) \rangle$) was computed for each monomeric unit. Next, groups of 16 of these functions that correspond to monomeric units at the same position along each of the 16 star polymer arms were averaged. We note that we do not report correlation times, but simply trends, since some of the OTCF profiles decay on timescales not accessible from our simulation.

Monomer-Monomer orientational correlation functions were computed in a similar manner to the OTCFs. The same local orientational unit vectors described above were utilized to compute a correlation function ($\langle u(n_0) \cdot u(n_i) \rangle$), where n_0 corresponds to a given reference monomer and n_i corresponds to the i^{th} monomer from monomer n0 along the polymer arm. Finally, the functions were averaged across all polymer arms and across time. For many applications in polymer physics, this correlation may be described with an exponential function that decays with a characteristic length scale, known as the persistence length [80]. Due to the highly structured nature of the polymers studied, we found that the correlations did not fit an exponential decay and we therefore report monomer-monomer orientational correlations.

Hydrogen bonds for the S-PEG and L-PEG system were computed using the HBonds Plugin of Visual Molecular Dynamics (VMD) [81]. The plugin computes the total number of hydrogen bonds between specified types of atoms in the system, in this case between water molecules (hydrogen bond donors) and PEG oxygen (hydrogen bond acceptors) within a cutoff distance of 3.0 Å and a cutoff angle of 20 degrees.

Results

From the principal moments of the gyration tensor, we determined that the shape of all star polymers at all temperatures were found to be nearly spherical, with asphericity measured to be 0.05 or less. Appendix Figure 3.10 reports the temperature trends in the radius of gyration, Rg, for both the inner hydrophobic arms as well as the entire star polymer, for all 4 star polymers considered here. We find that the radius of gyration scales nearly quantitatively based on Flory's mean field approximation in a poor solvent [82], i.e. $Rg \sim N^{1/3}$ when compared between PVL_8PEG_6 and $PVL_{16}PEG_{24}$. The radius of gyration of the hydrophobic segments of the PEG star polymers scale as 21/3, consistent with the observed values of 13.2 to 13.5 for the smaller star polymer compared to the larger star values of 16.7 to 17.2 , over the complete temperature range. Although the hydrophobic regions are the same between S-PEG and S-POXA and L-PEG and L-PC1, respectively, the hydrophobic regions are slightly more expanded for the POXA and PC1 star polymers.

Correspondingly, the Rg of the complete PEG star polymers scale approximately as $(40/14)^{1/3}$, providing agreement between the measured values of 15.5 Å and 22.0 Å seen for S-PEG and L-PEG, although L-PEG has a weak temperature dependence that is absent for S-PEG that gives deviations of ∼2% to larger Rg from the predicted value at 350 K and 450 K. When fully extended, S-POXA should be ∼3.8% longer than S-PEG, and its Rg is consistent with that at the coldest temperature, however the POXA polymer shows a temperature trend that increases the Rg beyond the expected scaling. By contrast, while the L-PC1 polymer is expected to be more expanded by ∼2.5% compared to L-PEG based on extended length considerations, instead its Rg is smaller by up to ∼6% when compared to the large PEG star polymer. These variations in Rg would indicate that the polymer arms have specific chemical interactions that are influencing the observed deviations from idealized polymer behavior.

Voronoi analyses provide an effective method for exploring the frequency of observed contacts made between the hydrophobic and hydrophilic segments of the arms, and the exposure of polymer segments to bulk water. The presence of water clusters separated from the bulk, i.e., interior to the star polymer can also be identified as quantified in Figure 3.3. If there are multiple water molecules inside the polymer, they may be connected, to form a single cluster, or they may be separate, forming separate interior water clusters. At any given time, a polymer could have no interior water clusters, or it could have one or more interior water clusters, each comprised of a varying number of water molecules. When considering the interior water cluster results, we find that S-PEG does not have any absorbed water

∼75% of the time (at 350K), similar to all polymers studied in previous work [61], and when water was absorbed, it was in only 1 or 2 interior clusters. In contrast, S-POXA and L-PEG have some internal water present at least 70% of the simulated time, while L-PC1 always has some internal waters, although for all star polymers the clusters are typically very small, ranging from 1 to 6 water molecules at most. The higher presence of individual water clusters within L-PC1 compared to the other star polymers arises from a complex interaction network of the branched star arms that create small pockets for water to cluster in.

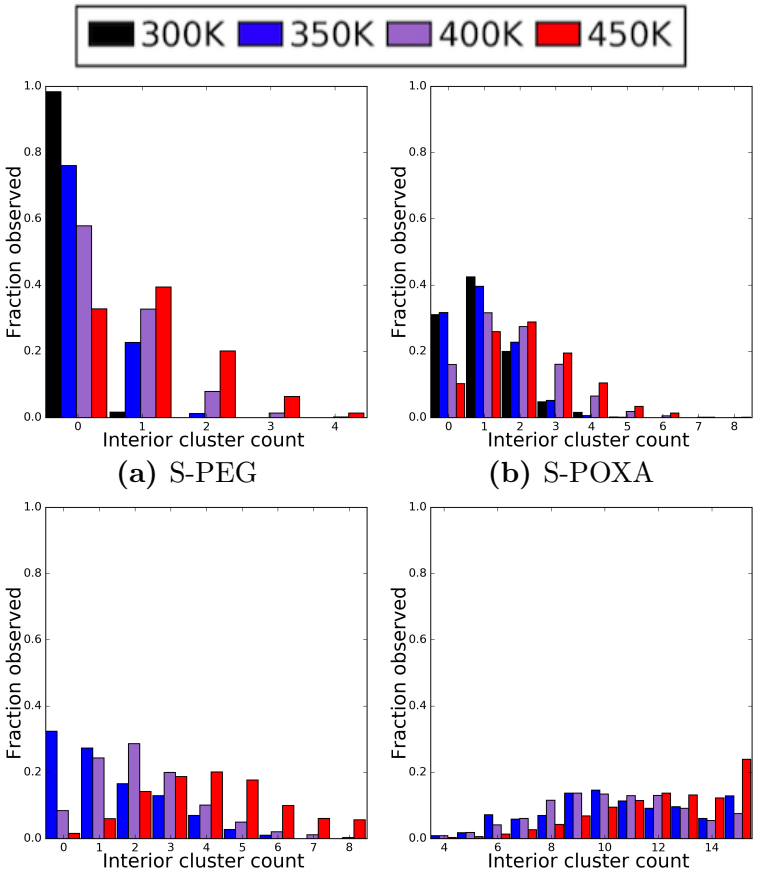

(a) S-PEG **(b)** S-POXA

(c) L-PEG **(d)** L-PC1

Figure 3.3: *Histogram of the number of interior water clusters at a given temperature* (a) S-PEG, (b) S-POXA, (c) L-PEG, and (d) L-PC1.

However what is most interesting is where the water clusters reside in the polymer (Figure 3.4). In contrast to the previous work [61], we present the location of the interior water with respect to the location of the center of mass polymer's adamantane core (previously, the penetration of interior waters was given by a depth, taken with respect to the bulk water; see Appendix Figure 3.12). Given the fact that the polymer regions are on average spherical, we are able to compare water cluster location to the average boundaries of the hydrophobic

Star type	Fraction of surface area shared with hydrophobic neighbors			
	300 K	**350 K**	**400 K**	**450 K**
S-PEG	0.76	0.88	0.84	0.89
S-POXA	0.55	0.64	0.68	0.74
L-PEG	-	0.88	0.80	0.82
L-PC1	-	0.37	0.42	0.52

Table 3.5: *Average fraction of interior cluster surface area shared by hydrophobic neighbors for an interior water cluster.* For each interior water cluster, the voronoi analysis provided a list of all neighboring atoms. These neighboring atoms were then sorted into hydrophobic and hydrophilic groups and their interfacial areas between both polymer types were summed and averaged over all interior water clusters observed.

PVL region and the entire polymer radius, R, computed for a spherical particle as a direct function of our simulated value of Rg. i.e. $R = (5/3)^{1/2} R_g$. Surprisingly, and regardless of size, the PEG polymers have water clusters that intercalcate mostly in the hydrophobic PVL interior, while S-POXA has water at the hydrophobic-hydrophilic interface, whereas L-PC1, which has the most internal water, is concentrated primarily in the hydrophilic outer block. Temperature does not change the trend in where the interior water is found for any of the star polymers, although higher temperature does increase the frequency of observance of interior water clusters and the corresponding cluster sizes become larger on average (see Figure 3.3). Although the rough topology of the star polymer may lead one to conclude that the absolute distance of the interior water from the adamantine core could be misleading, we also provide the water cluster neighbor types obtained from the Voronoi analysis, summarized in Table 3.5, which supports the location of water clusters in each polymer block type.

By contrast, when comparing the degree of interaction of the different star polymers with bulk water, we find that both the hydrophilic arms of S-PEG and L-PEG star polymers are better solvated than the more branched S-POXA and L-PC1 polymers at any temperature, even though the latter star polymers were designed to be more soluble (Figure 3.5). The PEG star polymers preference for solvent is also manifest in the fact that it increases the PVL-PVL interactions, and shares the least surface area contact with the PVL hydrophobic core, compared to the other star polymers. On the other extreme, PC1 shows significantly stronger polymer-polymer associations, as measured by an increased Voronoi surface area between hydrophilic segments, and evidence that the hydrophilic block overlays and coats the hydrophobic core, likely explaining its reduced Rg relative to L-PEG (Figure 3.5). In addition both PEG-based star polymers show evidence for decreasing interactions with aqueous solvent and increasing interaction of the hydrophilic arms as temperature in-

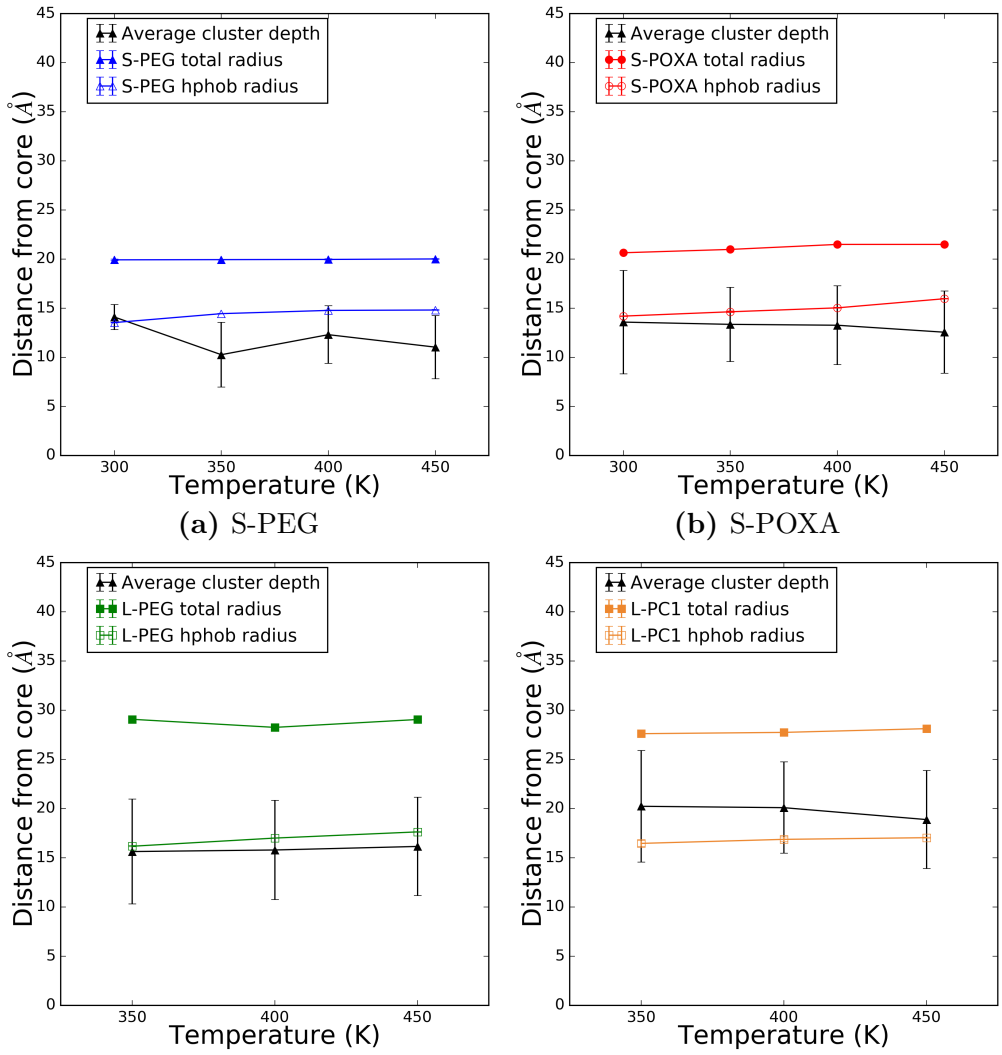

(a) S-PEG **(b)** S-POXA **(c)** L-PEG **(d)** L-PC1

Figure 3.4: *The average radius of the complete star polymer (solid marker) and of the hydrophobic core only (smaller value/white marker) as a function of temperature.* The black line shows the average water cluster distance from the adamantane core at each temperature (a) S-PEG, (b) S-POXA, (c) L-PEG, and (d) L-PC1. Uncertainty estimates are ±1 standard deviation.

creases, supporting the fact that PEG-based star polymers may also be thermo-sensitive like their linear analogues, although we return to this point below. By contrast, the POXA and PC1 polymers have at most a weak temperature dependence, with solubility increasing ever so slightly, over the 350 K to 450 K range (Figure 3.5a).

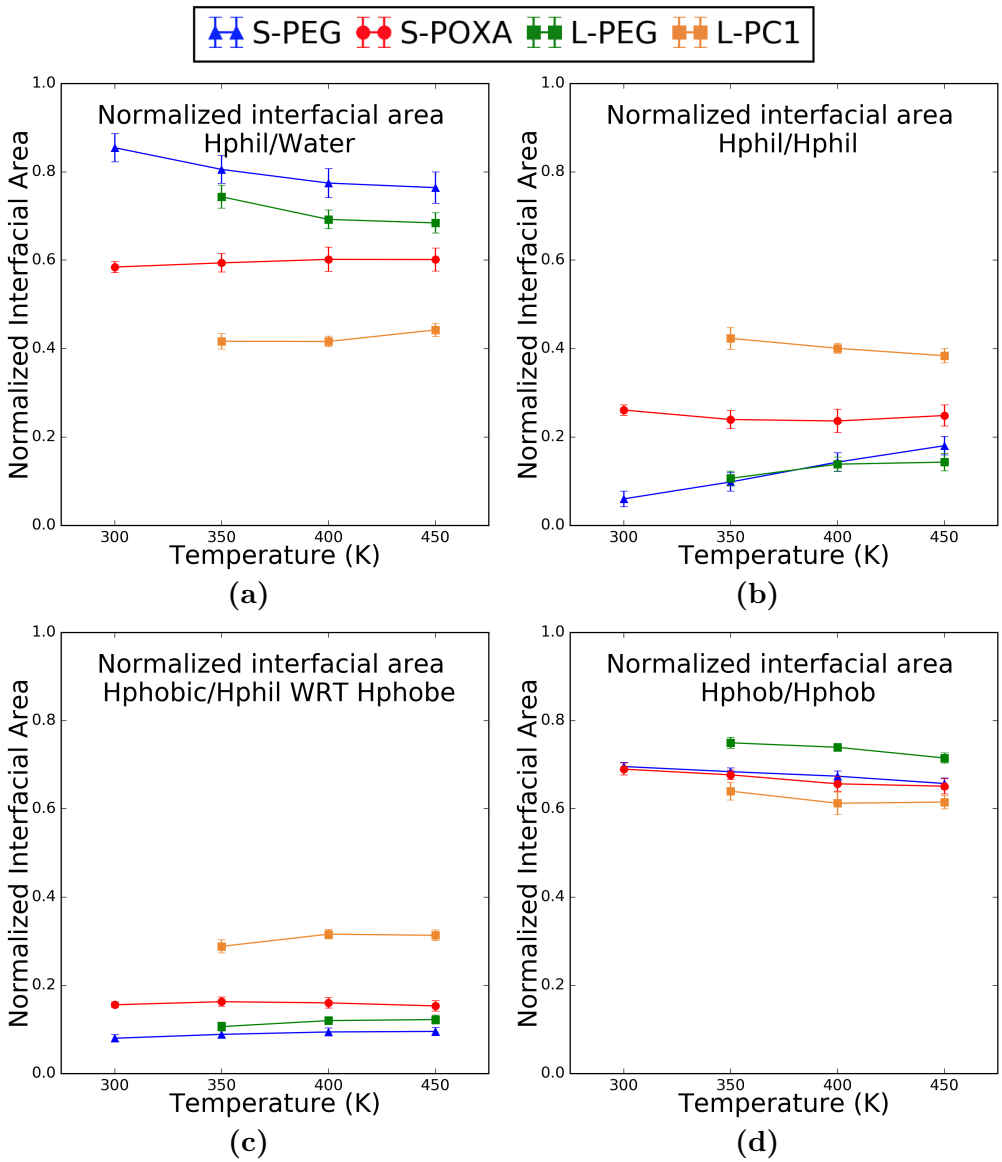

Figure 3.5: *Interfacial area as a function of temperature measured by Voronoi analysis of different diblock regions of the star polymers and water.* (a) Interfacial area between the hydrophilic arms and bulk water. (b) Interfacial area within and between hydrophilic arms. (c) Interfacial area between the hydrophilic and hydrophobic (PVL) blocks of the star arms. (d) Interfacial area within and between the hydrophobic (PVL) arms. Uncertainty estimates are ±1 standard deviation.

Further insight into domain areas of rigidity and flexibility of the four star polymers,

and their temperature dependence, is evident in their orientational time correlation function (OTCF) (Figure 3.6) and orientational correlation function (OCF) between different pairs of monomer units along the polymeric arms. For monomers close to the adamantane core the OTCFs do not decay at all for any star polymer, however monomer units further out along the arms show rates of decay of their orientational memory that are distinct for each of the star polymers. While the most distant PEG group decays very rapidly for both the small and large polymer, supporting the fluidity of the PEG polymeric block, the monomer ends of POXA and PC1 do not decay on the 2 ns upper bound placed on the measured correlation time from our simulations, with POXA showing glassy behavior while PC1 appears to behave as a solid. Furthermore, the OTCF for monomers at the transitional interface between hydrophobic-hydrophilic polymer blocks for both POXA (the 8th PVL and 1st POXA) and PC1 (the 16th PVL and 1st PC1 monomers) remain strongly coupled for all temperatures; in fact the relaxation time for the 1st PC1 monomer is nearly as slow as the 1st PVL monomer near the adamantane core, limiting the reorientations allowed for the central hydrophobic beads of the PVL hydrophobic core. In contrast, we find that for the PEG star polymers that the PVL and PEG monomers, including the transitional regions, are decoupled such that each region along the arm is decaying on its own timescale.

When we analyze the OCF between different pairs of monomer units of the star polymers, we considered two monomer reference points: the hydrophobic bead attached to the adamantane core to measure correlations out to the last hydrophilic bead (Figure 3.7) and the last hydrophilic bead at the end of the diblock arm to measure correlations back toward the adamantane core (Figure 3.8). Qualitatively all four star polymers exhibit negative correlations in the hydrophobic arms near the adamantane core, and the oscillations in bond vector directions indicate a complicated folding pattern that never relaxes to the exponential decay of a worm-like-chain model in the hydrophobic region regardless of temperature and length of the PVL block we examined here. However, beyond the transitional region the bond correlations of the 1st PVL monomer with the hydrophilic region shows a decay to zero that is temperature dependent for each star polymer. For S-PEG and S-POXA we find that the OCF with respect to the 1st PVL monomer over the hydrophilic section decays to zero above 300K, whereas for L-PEG the bond correlations decay to zero above 350K. In contrast to the other three systems, over the 350-450K temperature range we simulated for PC1, the bond vectors retain some degree of correlation even at the highest temperature.

These trends are even more dramatic when considering the hydrophilic bead as the reference monomer (Figure 3.8). In this case both PEG polymers exhibit a OCF that closely approximates 1-2 bond vectors consistent with a freely joined chain above their transition temperature of 300K for S-PEG and 350K for L-PEG, and in the case of L-PEG the temperature transition to uncorrelated bond vectors is striking. However, the OCF for S-POXA is somewhat longer ranged (extending in cases almost to the farthest hydrophilic monomer unit from the arm terminus) than found for the PEG polymers, and furthermore the bond vectors are still weakly correlated in the hydrophilic region even at the highest temperatures. Finally for L-PC1, the evidently strong hydrogen-bonding interactions among the branched hydrophilic arms, and the solid-like nature of motions of the hydrophilic block of the L-PC1

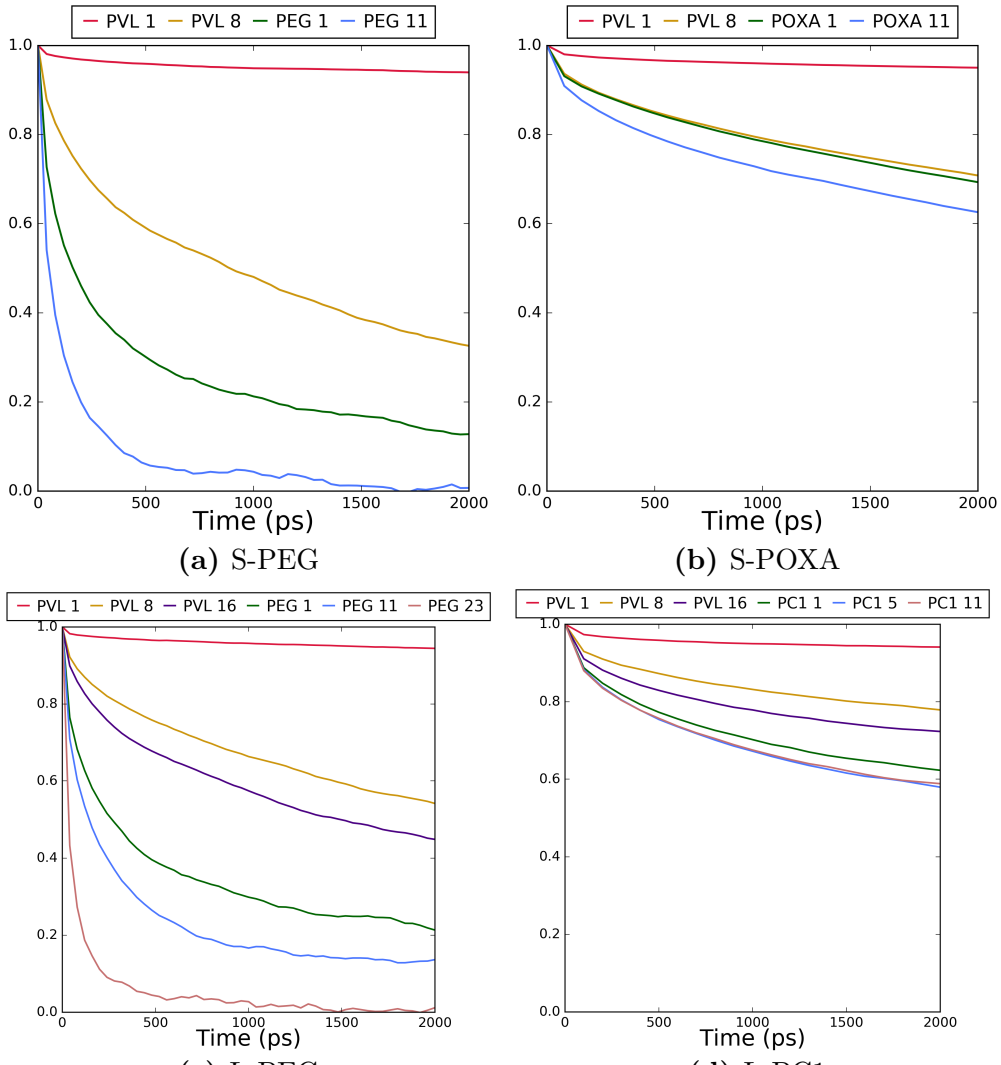

(a) S-PEG **(b)** S-POXA

(c) L-PEG **(d)** L-PC1

Figure 3.6: *Orientational time correlation functions as a function of temperature* (a) S-PEG, (b) S-POXA, (c) L-PEG, and (d) L-PC1.

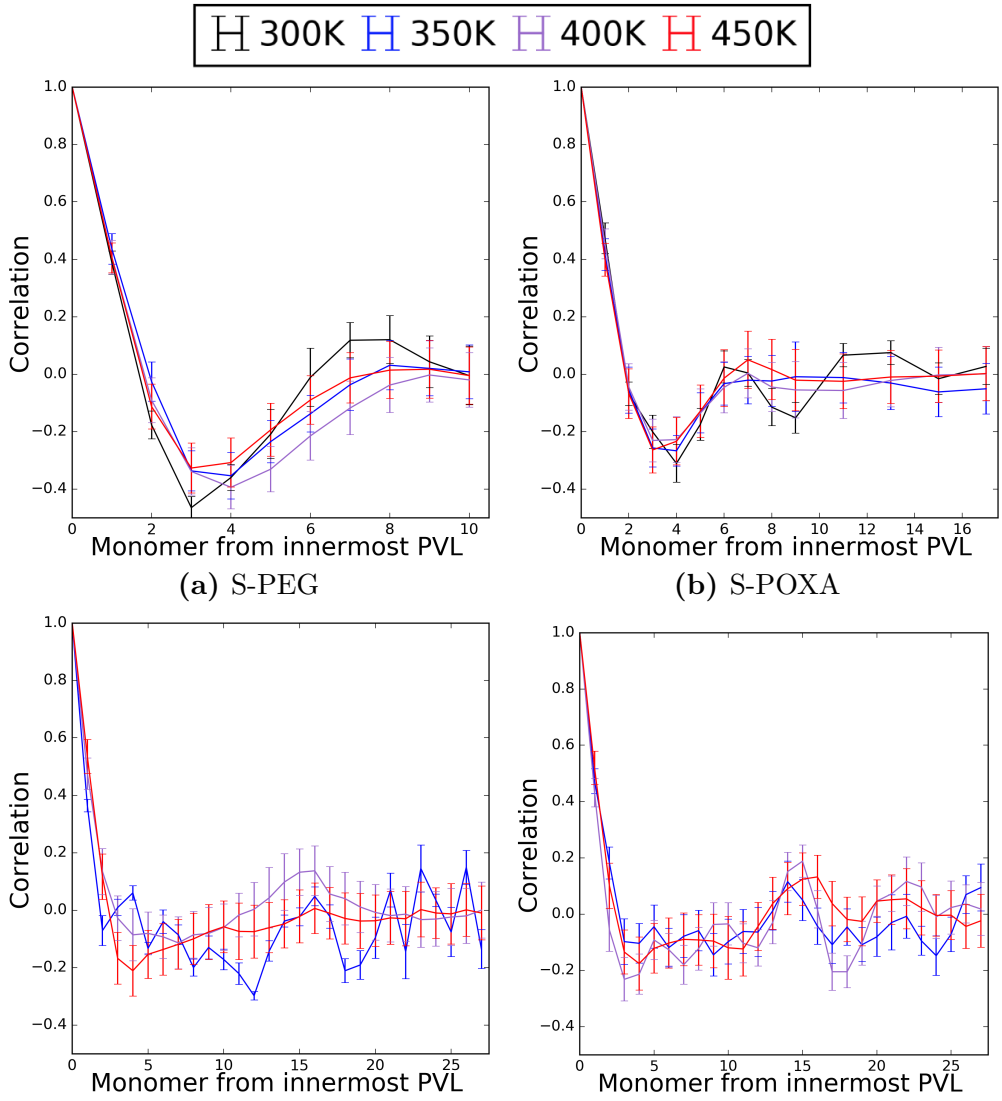

(a) S-PEG **(b)** S-POXA

(c) L-PEG **(d)** L-PC1

Figure 3.7: *Orientational correlation between pairs of monomers as a function of temperature with respect to the reference PVL monomer attached to the adamantane core.* (a) S-PEG, (b) S-POXA, (c) L-PEG, and (d) L-PC1. Uncertainty estimates are based on the standard deviation in the mean exhibited by the behavior of corresponding repeat units among the 16 arms of each star polymer.

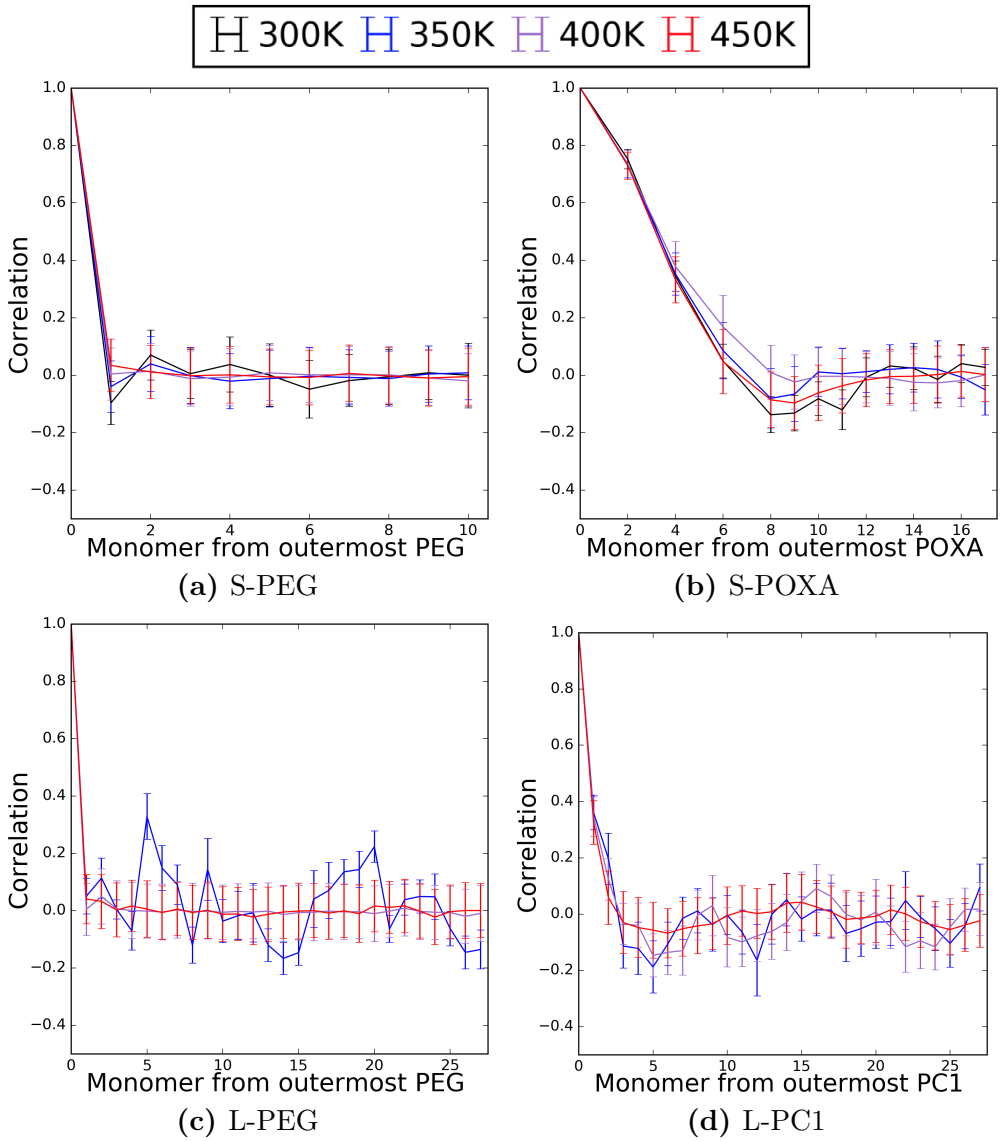

(a) S-PEG **(b)** S-POXA **(c)** L-PEG **(d)** L-PC1

Figure 3.8: *Orientational correlation between pairs of monomers as a function of temperature with respect to the reference hydrophilic monomer at the end of each polymer arm and moving in toward the adamantane core.* (a) S-PEG, (b) S-POXA, (c) L-PEG, and (d) L-PC1. Uncertainty estimates are based on the standard deviation in the mean exhibited by the behavior of corresponding repeat units among the 16 arms of each star polymer.

star polymer, shows that the bond vectors remain highly correlated at all temperatures, making the PVL-PC1 diblock combination the least thermosensitive of the star polymers examined here.

The underlying structural origin of the order-to-disorder transition at the melting temperature for the PEG polymers, i.e. as observed in the bond correlation vectors in Figure 3.8, can be explained by analysis of the dihedral angle populations and PEG-water hydrogen bonding as a function of temperature for S-PEG (Figure 3.9a) and L-PEG (Figure 3.9b). The dominant conformation in the aqueous phase is trans (C-O-C-C), gauche (O-C-C-O) and trans (C-C-O-C), TGT, which strongly favors complexation with water and overcomes the unfavorable conformational entropy of this dominant structure and the ordered water network around the polymeric arms. As temperature increases the TGT populations decreases by $\sim 10\%$ while all other conformations (TTT and TGG in particular) increase, resulting in the release of the more ordered water near the PEG surface and a broader distribution in PEG conformations, and a decreased number of PEG-water hydrogen bonds (Figure 3.9c).

Discussion and conclusions

Biomedical applications of star polymers as a drug delivery system rely on the design of its polymer block chemistries and architectures to be thermosensitive and biocompatible, with the additional ability to be biodegradable over suitable time scales. We note that our star polymer system sizes are relevant for the biomedical applications for which they are designed. Below 400 Da, PEG chains are toxic in humans as a result of sequential oxidation to acid metabolites by dehydrogenases [83]. At the same time, the molar mass should not exceed the renal clearance threshold for complete excretion of the polymer, this limit being in the range of 20-60 kDa for nondegradable polymers [83]. Our systems studied have masses that range from 16-16.5 kDa, and considering that experimental stars have a nanogel core as well, they are at the border of the renal clearance threshold. This means that size effects and degradation studies are quite important as research into star polymers proceeds in the future.

Contrary to our initial hypotheses, increased side-chain branching of the hydrophilic monomers did not increase the hydrophilicity of the POXA and PC1 polymer system, but in fact, decreases polymer-water interactions due to stronger polymer-polymer interactions in the hydrophilic domain. Voronoi interfacial surface area data combined with strong dynamical correlations of POXA and PC1 monomers support these conclusions. With regards to water cluster penetration events, PEG polymers exhibited the most water penetration into the hydrophobic domains, while the extensive level of polymer networking in the PC1 domains provides regions in which small water clusters may reside, and POXA serves as an intermediate between these two extremes. This suggests that the PEG polymers, with their better solvent exposure and greater number of water penetration events into the PVL region compared to the PC1 and POXA polymers, may more readily degrade by hydrolysis, although that degradation may be more limited at higher temperatures. Such analysis is

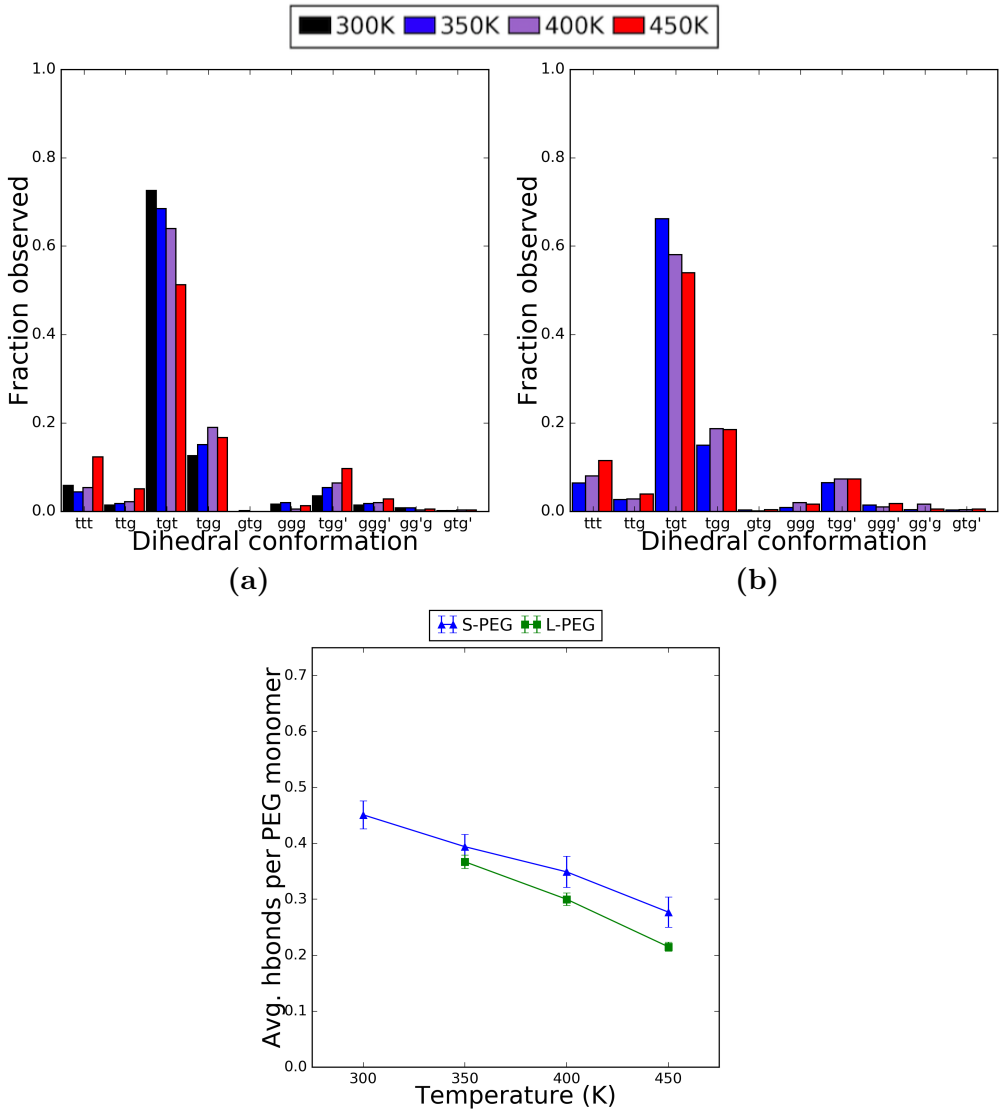

Figure 3.9: *Dihedral angle distributions for PEG as a function of temperature.* (a) S-PEG, (b) L-PEG and (c) Average number of hydrogen bonds per PEG monomer as a function of temperature for both PEG stars.

vital considering current research [83, 84] on the biocompatibility of PEG and the search for alternatives.

Although PEG-based polymers have been a long industry standard, there are known limitations in synthetic functionalization, and adverse accumulation in the body [85], which drive the search for new and competitive biocompatible polymers such as poly-oxazoline [60]. One of the primary conclusions presented here is that the PEG-based star polymers have structural and dynamical properties that are more sensitive over physiological temperatures than what is observed for the POXA and PC1 star polymers analyzed here. Based on the integrated structural data presented in the results section, we find that the thermodynamic origins of the order-to-disorder transition we observe as temperature increases for PEG star polymers is consistent with entropy-driven dehydration. PEG block regions mix well with water at low temperatures, but exhibit signs of phase separation at higher temperatures, indicating the possibility of a LCST transition, which is observed for linear PEG polymers. At low temperatures the polymeric arms of PEG are dominated by an enthalpically favored TGT conformation, which is stabilized through formation of strong water-ether hydrogen bonds. As temperature increases the entropically favorable release of the ordered water and increased conformational entropy of dihedral angle configurations of the PEG backbone dominate to create a disordered form of the PEG star polymer (see Figure 3.9).

Although other POXA chemistries have been reported to experience a LCST [86], our analysis of Poly-2-methyl-2-oxazoline agrees with studies indicating the short aliphatic methyl side chain of POXA polymers is insufficient for exhibiting a phase transformation3, and thus future studies will consider an optimal length for the aliphatic side chains of POXA in the future. POXA is also sensitive to pH which provides another "handle" for structural and dynamical investigations [87]. PC1 is so highly branched and structured that its conformation and interactions with water remain the same across a range of physiological temperatures, indicating that it is least promising in regards drug delivery, and is likely not biocompatible due to hydrogen bond donors that are known to enhance undesirable interactions with surfaces and blood proteins [88], although it may be suitable for alternative applications such as polymer coatings.

While initial theoretical studies in the field of star polymers has begun [61, 76, 89, 90], harnessing the power of various polymer chemistries for use in drug delivery applications will need to explore areas such as drug loading, drug release and biotoxicity. We believe that the LCST in linear and star PEG polymers and certain POXA polymers may be manipulated for drug delivery systems for finely targeted delivery and degradation mechanisms. Other properties, such as branching and hydrogen bonding sites may also be manipulated to tune polymer behavior for other applications.

Acknowledgements

This work was supported by the Laboratory Directed Research and Development Program of Lawrence Berkeley National Laboratory under U.S. Department of Energy Contract No. DE-

AC02-05CH11231. This research used resources of the National Energy Research Scientific Computing Center, which is supported by the Office of Science of the U.S. Department of Energy under Contract No. DE-AC02-05CH11231. LF was supported by the National Science Foundation Graduate Research Fellowship under Grant No. DGE 1106400. We also thank the National Science Foundation grant CHE-1265731 for undergraduate training support for DHB.

Appendix

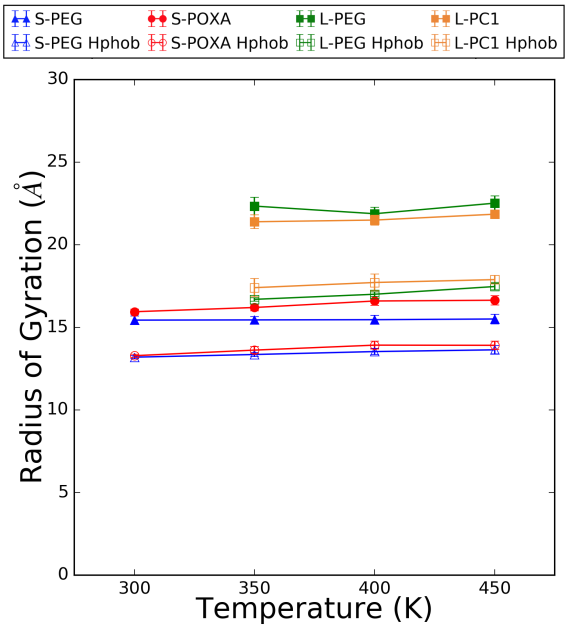

Figure 3.10: *The average radius of gyration of the complete star polymer (solid marker) and of the hydrophobic core only (smaller value/white marker) as a function of temperature.* Uncertainty estimates are ±2 standard deviations and are approximately the size of the symbols.

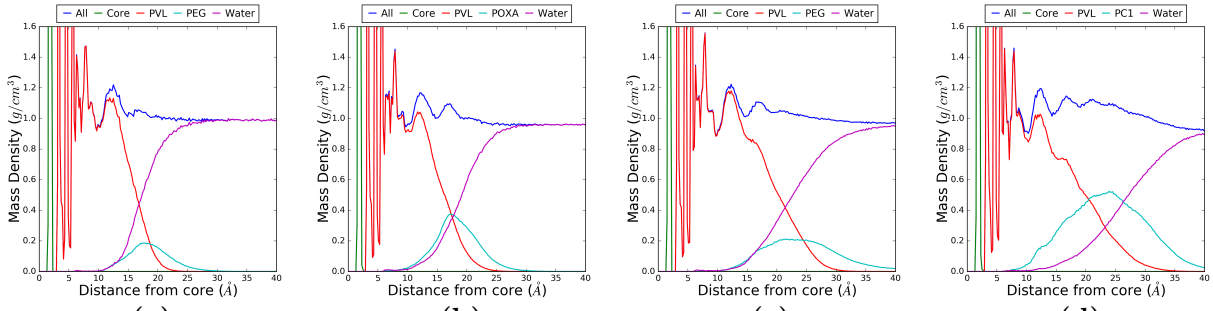

(a) **(b)** **(c)** **(d)**

Figure 3.11: *Orientationally averaged mass density curves for each star polymer at 350 K as a function of distance from the center of mass of the adamantane core.* (a) S-PEG, (b) S-POXA, (c) L-PEG, and (d) L-PC1.

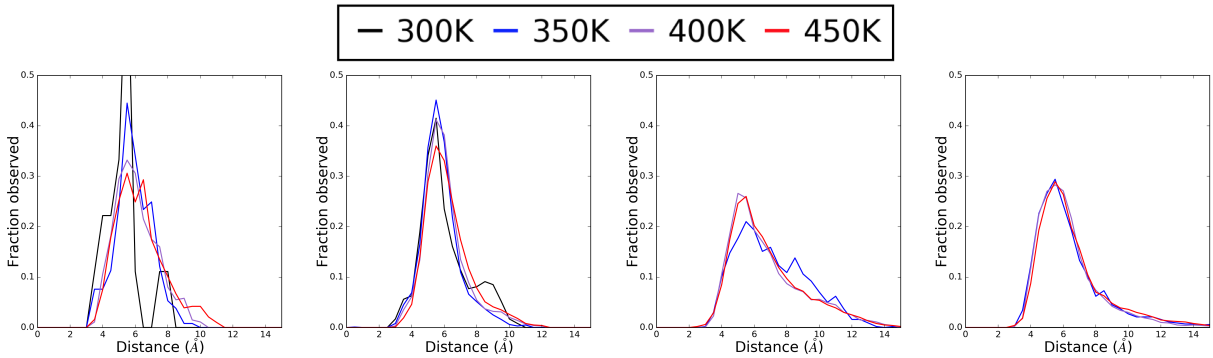

Figure 3.12: *Depth profiles for water molecules penetrating into the interior of the star polymers.* (a) S-PEG, (b) S-POXA, (c) L-PEG, and (d) L-PC1.

Chapter 4

Structural Transition of Nanogel Star Polymers with pH by Controlling PEGMA Interactions with Acid or Base Copolymers

We use small angle x-ray scattering (SAXS) to characterize a class of star diblock polymers with a nanogel core on which the outer block arms are comprised of random co-polymers of temperature sensitive PEGMA with pH sensitive basic (PDMAEMA) and acidic (PMAA) monomers. The acquired SAXS data shows that many of the nanogel star polymers undergo a sharp structural transition over a narrow range of pH, but with unexpectedly large shifts in the apparent pK_a with respect to that of the acidic or basic monomer unit, the linear polymer form, or even an alternate star polymer with a tightly cross-linked core chemistry. We have demonstrated a distinct and quantifiable structural response for the nanogel star copolymers by altering the core or by pairing the monomers PDMAEMA-PEGMA and PMAA-PEGMA to achieve structural transitions that have typically been observed in stars through changes in arm length and number. [1]

Introduction

The use of nanoparticle delivery vehicles such as liposomes [92], dendrimers [93], micelles [94], and star polymers [95–97] offer great promise for medical applications that require

[1] Reproduced from [91] with permission.

in vivo delivery of functional materials such as pharmaceuticals and imaging agents [98, 99]. Of specific importance to biomedical applications is the development and characterization of poly(ethylene glycol) (PEG) nanoparticles, since their high water solubility, thermosensitivity, and low immunogenicity have made it the most recognized polymer chemistry exhibiting biocompatibility and increased circulation time in vivo. [92–94, 100–102] Although PEG-based polymers have been widely used in biomedical applications, there are known limitations in its synthetic functionalization, for example to create sensitivity to pH changes. Smart polymers that exhibit a pH induced structural response are important since different tissue environments and cell compartments exhibit a wide variation in pH, and thus offer the potential for a more targeted delivery of therapeutic drugs [99, 103].

Recently, the use of non-metal organocatalysis for ring opening polymerization has allowed for great ease in synthesis of novel nanogel star polymers, in which polymer arms are connected to a cross-linked polymer core [104, 105], with high uniformity (polydispersity indices <1.1) and with the ability to control for size (15 - 40 nm) [18, 106, 107]. Given this early promise there is nonetheless a large unexplored chemical landscape of possible star polymers of varied size and chemical composition which require characterization under physiological conditions of aqueous solvent, and how they respond to relevant stimuli such as temperature, pH, and buffers.

Here we present a systematic Small Angle X-ray Scattering (SAXS) study to characterize a series of polyelectrolyte star polymers composed of a divinylbenzene (DVB) crosslinked nanogel core, and diblock copolymer arms consisting of a hydrophobic block of poly-styrene (PS) followed by a hydrophilic block of (1) neutral poly(ethylene glycol) methacrylate (PEGMA): DVB-PS-PEGMA, (2) acidic poly(methacrylic acid) (PMAA): DVB-PS-PMAA, (3) basic poly(2-dimethylaminoethyl methacrylate) (PDMAEMA): DVB-PS-PDMAEMA, (4) 50% PMAA and 50% PEGMA distributed randomly in the outer block: DVB-PS-$PMAA_{50\%}$/ $PEGMA_{50\%}$, and (5) 50% PDMAEMA and 50% PEGMA distributed randomly in the outer block: DVB-PS-$PDMAEMA_{50\%}$/ $PEGMA_{50\%}$,. While there are a number of studies on the behavior of linear and weak polyelectrolyte star polymers, they have been largely confined to homopolymers and have focused on a thermal response and the position of the LCST. [24]

While the DVB-PS-PEGMA and the DVB-PS-PMAA star polymers do not undergo structural transitions over the evaluated pH range, we show that the DVB-PS-$PMAA_{50\%}$/ $PEGMA_{50\%}$, DVB-PS-$PDMAEMA_{50\%}$/ $PEGMA_{50\%}$, and DVB-PS-PDMAEMA star polymers undergo a sharp structural transition over a narrow range of pH, consistent with their titration curves, but with unexpectedly large shifts in the apparent pK_a when compared to the linear polymer form or even a star polymer with a more tightly cross-linked core. Our studies provide a molecular level understanding for pairing of PEGMA with acidic and basic substituents, and the effect of pH, on copolymer nanogel star architectures. This work illustrates the ability to fine-tune a structural transition response to desired pH through control of chemical composition of the arms and nanogel star polymer architecture.

Experimental Methods

General procedures

^{1}H NMR spectra were obtained on a Bruker Avance 2000 spectrometer (^{1}H, 400 MHz), and were referenced to internal solvent residue (CDCl3: ^{1}H = 7.26 ppm). All NMR spectra were recorded at ambient temperature using standard Bruker library pulse programs and are reported as the fully proton-decoupled spectra. Analytical Gel Permeation Chromatography (GPC) using Waters high resolution columns HR1, HR2, HR4E and HR5E (flow rate 1 mL / min, THF) in conjunction with a waters 996 photodiode array and/or a waters 411 differential refractometer was used to determine molecular weight distributions, Mw/Mn, of polymer samples with respect to linear polystyrene standards. Light Scattering measurements were made to determine Mw, Mw/Mn, using the aforementioned column set with a Wyatt DAWN EOS multi-angle light-scattering detector, QELS quasi elastic light scattering detector and Optilab (intraferometric refractometer). Deuterated solvents were purchased from Cambridge Isotopes, Inc. and used as received. 3-(tert-Butyldimethylsilyloxy)-1-propyl lithium (20 wt% solution in cyclohexane) was purchased from FMC Lithium Division and used as received. Styrene (S), 2-(dimethylamino)ethyl methacrylate (DMAEMA), tert-butyl methacrylate (tBuMA) and N, N, N', N", N" - Pentamethyldiethylenetriamine (PMDETA) were purchased from Sigma-Aldrich and purified by vacuum distillation over CaH_2. Poly(ethylene glycol) methyl ether methacrylate (PEGMA) was also obtained from Sigma-Aldrich and purified by passing through basic alumina column. Para-divinylbenzene (p-DVB), Cu(I)Cl and dry solvents were purchased from Sigma-Aldrich and used as received.

Synthesis of DVB-PS-PDMAEMA

Nanogel core Polystyrene star macroinitiators and Poly (N,N-dimethyl-aminoethyl meth acrylate)-b-Polystyrene Star Polymer (PS-PDMAEMA Star) were synthesized as reported earlier. [19]

Synthesis of DVB-PS-PEGMA

ATRP-macroinitiator nanogel star polymer (2.0 g, Mn arm = 2.8 kDa, 35 arms), PEGMA (34.3g) and PMDETA (0.12g) were dissolved in anisole (65 mL). Three freeze-pump-thaw cycles were performed and then Cu(I)Cl (0.07g) was added under positive Ar flow. The reaction mixture was sealed under Ar atmosphere before being heated to 45°C. After 60 min, the reaction mixture was cooled down in liquid N_2, opened to air and precipitated into hexanes twice. Obtained white gooey solid was freeze-dried from dioxane. Yield: 18% (6.5 g). ^{1}H NMR (400 MHz, $CDCl_3$, δ) = 7.27-6.30 (br. m, 135 H), 4.5-4.05 (br. s, 41H), 4.05-3.45 (br. m, 383H), 3.45-3.05 (br. s, 62H), 2.20-1.55 (br. s, 28H), 1.55-0.9 (br. m, 95H), DLS (THF): Mw = 315 kDa (1.37), DP (PEGMA) = 20 (6.1 kDa)

Synthesis of DVB-PS-PMAA

ATRP-macroinitiator nanogel star polymer (0.27 g, Mn arm = 3.7 kDa), tBuMA (1.65 g) and PMDETA (0.012g) were dissolved in anisole (11 mL). Three freeze-pump-thaw cycles were performed and then Cu(I)Cl (0.007g) was added under positive Ar flow. The reaction mixture was sealed under Ar atmosphere before being heated to 45°C. After 1 hour, the reaction mixture was cooled down in liquid N_2, opened to air and precipitated into hexanes twice. Obtained white solid was dried under vacuum for 24 hours. Yield: 31% (0.6g). DP (tBuMA) = 65 as determined by 1H NMR. Resulted polymer (0.5 g), was dissolved in 12 mL of dioxane and 0.45 mL of concentrated HCl was added to the polymer solution. Reaction mixture was stirred for 20h at 90°C, upon completion, reaction mixture was cooled down and precipitated into hexanes. Yield: 56% (0.28g).^{1}H NMR (400 MHz, CD_3OD, δ in ppm) = 7.5-6.16 (br. m., 178 H), 3.2-1.7 2.63 (br. m., 193H), 1.70-0.5 (br. m., 230H). DLS (water): Mw = 294 kDa (1.31).

Synthesis of DVB-PS-PMAA$_{50\%}$/PEGMA$_{50\%}$

ATRP-macroinitiator nanogel star polymer (2.0 g, Mn arm = 3.2 kDa, 31 arms), tBuMA (8.0 g), PEGMA (16.9 g) and PMDETA (0.10g) were dissolved in anisole (70 mL). Three freeze-pump-thaw cycles were performed and then Cu(I)Cl (0.06g) was added under positive Ar flow. The reaction mixture was sealed under Ar atmosphere before being heated to 45°C. After 90 min, the reaction mixture was cooled down in liquid N2, opened to air and precipitated into hexanes twice. Obtained white gooey solid was dried under vacuum for 24 hours. Yield: 23% (6.1g). Resulted polymer, 5 g was dissolved in 120 mL of dioxane and 4.5 mL of concentrated HCl was added to the polymer solution. Reaction mixture was stirred for 20h at 90°C, upon completion, the reaction mixture was cooled down and precipitated into hexanes. Yield: 63% (3.15g). ^{1}H NMR (400 MHz, $CDCl_3$, δ) = 7.25-6.25 (br. m, 153 H), 4.32-3.97 (br. s, 44H), 3.57 (s, 46H), 3.77-3.62 (br. m, 305H), 3.4 (s, 67H), 2.10-1.75 (br. s, 113H), 1.7 (s, 115H), 1.43 (s, 308H), 1.2-0.6 (br. m, 171H). DLS (THF): Mw = 285 kDa (1.25), DP (PEGMA) = 22, DP (PMAA) = 23 based on 1H NMR

Synthesis of DVB-PS-PDMAEMA$_{50\%}$/PEGMA$_{50\%}$

ATRP-macroinitiator nanogel star polymer (2.0 g, Mn arm = 2.8 kDa, 35 arms), DMAEMA (8.5g), PEGMA (17.1g) and PMDETA (0.12g) were dissolved in anisole (65 mL). Three freeze-pump-thaw cycles were performed and then Cu(I)Cl (0.07g) was added under positive Ar flow. The reaction mixture was sealed under Ar atmosphere before being heated to 45°C. After 90 min, the reaction mixture was cooled down in liquid N2, opened to air and precipitated into hexanes twice. Obtained white gooey solid was dried under vacuum for 24 hours. Yield: 24% (6.7 g). ^{1}H NMR (400 MHz, $CDCl_3$, $\delta\delta$) = 7.25-6.25 (br. m, 135 H), 4.11 (br. s, 63H), 3.80-3.62(br. s, 50H), 3.62-3.55 (br. s, 15H), 3.4 (s, 34H), 2.85-2.55 (br. s, 23H), 2.55-2.30 (br. s, 61H), 2.3-1.7 (br. m, 76H), 1.7-1.2 (br. m, 68H), 1.15-0.68 (br.

m, 56H). DLS (THF): Mw = 300 kDa (1.22), DP (PEGMA) = 11, DP (DMAEMA) = 19 based on ^{1}H NMR

SAXS Experiments

In this work, X= and/or Y= PEGMA, PMAA (acidic), or PDMAEMA (basic) (see insets of Figures 4.2- 4.6 and further details are given in Table 4.1). We have quantified the size and shape as a function of pH using small angle X-ray scattering (SAXS) of the following series of star nanoparticles which differ in their outer block chemical composition: DVB-PS-PEGMA, DVB-PS-PDMAEMA, DVB-PS-PMAA and statistical compositions of basic and acidic units, DVB-PS-PDMAEMA$_{50\%}$/ PEGMA$_{50\%}$ and DVB-PS-PMAA$_{50\%}$/ PEGMA$_{50\%}$.

The SAXS experiments were conducted on the SIBYLS beamline (12.3.1) at the Advanced Light Source synchrotron [108, 109]. For each SAXS experiment, samples were prepared in a standard 25 μl 96-well plate to examine each star polymer as a function of pH at two or more concentrations (somewhere between 1.0 mg/ml and 5.0 mg/ml). Incident X-rays were tuned to a wavelength (λ) of 1.03 Å at a sample-to-detector distance of 1.5 m, resulting in scattering data collected continuously with the momentum transfer, $Q = 4\pi sin(\theta/2)/\lambda$ (where 2θ is the scattering angle), over a range from 0.007 to 0.324 Å^{-1} with exposures of 0.5, 1, 2 and 6 seconds. All experiments were performed at 20°C. All data were scaled and buffer subtracted, and then averaged with the ScÅtter 2.0 package. Radii of gyration (R_g) were evaluated using the Guinier approximation, and analytical form factors were fit using SasView 3.1.1. [110]

SAXS Theory

The scattering intensity of a monodisperse system of particles can be described as follows:

$$I(Q) = NP(Q)S(Q) \tag{4.1}$$

Where I(Q) is the experimental scattering intensity, N is the number of particles, P(Q) is the single particle scattering function, also known as the form factor, and S(Q) is the inter-particle scattering function that accounts for interactions between particles. In this work we are primarily interested in the shape and size of the individual star polymers as a function of pH given potential applications such as drug delivery; hence we are interested in P(Q) and not S(Q). Therefore to ascertain the presence of intermolecular correlations (such as aggregation or particle repulsions) for each member of the pH series for each star polymer, we scaled the intensity of the different concentrations to each other. The intensity profiles matched exactly for DVB-PS-PEGMA, DVB-PS-PDMAEMA, DVB-PS-PDMAEMA$_{50\%}$/PEGMA$_{50\%}$ and DVB-PS-PMAA$_{50\%}$/ PEGMA$_{50\%}$, so that for these star polymers we can assume that S(Q)=1 and that any intensity features arise from the form factor of the individual particles. However the intensities for the DVB-PS-PMAA star polymer at different concentrations, for all pH values, did not scale to each other, indicating that there are interparticle correlations.

Star Polymer	**PEGMA**	**PDMAEMA**	**PMAA**	**PDMAEMA$_{50\%}$/ PEGMA$_{50\%}$**	**PMAA$_{50\%}$/ PEGMA$_{50\%}$**
Total Molecular Weight (kDa)	315	233	294	300	285
PS block weight (kDa)	2.8	3.3	3.7	2.8	3.2
PDI	1.37	1.27	1.31	1.22	1.25
AAN	35	32	29	35	27
	Hydrophilic Block				
Block weight (kDa)	6.1	4.7	5.6	6.0	8.9
PEGMA Weight Fraction (DP)	1.00 (20)	0.00	0.00	0.53 (11)	0.78 (22)
PMMA Weight Fraction (DP)	0.00	0.00	1.00 (65)	0.00	0.22 (23)
PDMAEMA Weight Fraction (DP)	0.00	1.00 (30)	0.00	0.47 (19)	0.00

Table 4.1: *Details of the nanogel star polymers.* The nanogel core is a cross-linked DVB core, and all star polymers have a common inner block of polystyrene. The star polymers differ in their outer block hydrophilic chemistry, composed of either pure PEGMA, pure PDMAEMA, pure PMAA, or the 50-50 series which are statistical compositions of the PMAA acidic or PDMAEMA basic groups with PEGMA.

Therefore for the 100% acid star polymer series we extrapolated the intensity of each Q-value to zero concentration in order to generate intensity curves in which S(Q)=1 is a good approximation, thus allowing us to fit the star polymer form factor and to perform a Guinier analysis for a single DVB-PS-PMAA star polymer.

The initial model-free analysis of the SAXS intensity data for the DVB-PS-PX_nPY_m star polymers using a Kratky plot of $I * Q^{5/3}$ vs. Q is presented in Figure 4.1. With the exception of the 100% acidic star polymer, all of the remaining star polymers at any pH value exhibit an overall globular shape, i.e. a peak at low Q (Figure 4.1a- 4.1d). Since the intensity does not decay after the first maximum, it supports a structural model of swollen chain statistics consistent with polymeric arms in a good solvent. It is interesting to note that the Kratky plot for the DVB-PS-PMAA is markedly different from the others, with no intensity maximum. Given the initial model-free analysis, we sought to find analytical functions that fit the SAXS data for the different DVB-PS-PX_nPY_m star polymers to gain more information about the size and structure in their response to changes in pH. The SAXS data did not fit several basic shapes such as uniform spheres, cylinders and ellipses, while the block copolymer micelle model was a slightly better fit than those shapes, but

still could not adequately fit all regions of the plot. However, we were able to identify three particle scattering functions, each of which performs well depending on pH or polymer series considered: the Dozier star polymer model [111, 112], the poly-disperse core shell (PCS) model [113, 114] or the Gaussian coil excluded volume (GCEV) model [115],

The star polymer form factor due to Dozier and coworkers [111, 112] is based on the Cotton and Daoud blob polymer model [116] that describes the star polymer as a succession of concentric rings of blobs of size, ξ, and within each blob, the polymer chain is described as a random coil. The resulting Dozier form factor:

$$P(Q, I_0, R_g, \alpha, \nu, \xi) = P_0 exp\left(\frac{-Q^2 R_g^2}{3}\right) + \frac{4\pi\alpha}{Q\xi}\Gamma(\mu)\frac{sin(\mu arctan(Q\xi))}{(1+Q^2\xi^2)^{\mu/2}} \tag{4.2}$$

was developed to fit to two separate Q-regions of scattering. The first term accounts for the overall size and shape of the star particle and determines its R_g, where P_0 is an intensity scale parameter that adjusts the fit at small Q. The second term accounts for the scattering at large Q, and corresponds to the Fourier transform of the structural correlations within the star polymer arms, where both α (an intensity scale factor) and ξ are used to adjust the fit to the data at large Q. The intensity at large Q should decay like $e - \mu - 1$, where $\mu = (1/\nu) - 1$, ν is the Flory exponent, and $\Gamma(\mu)$ is the gamma function. Given the nature of the star polymers investigated here, ν was fixed at a value of 2/3 to represent the polymer arms as chains in a good solvent.

The PCS model [113, 114], in contrast to the Dozier model, does not take into account the structural correlations in the star polymers explicitly, but instead considers the polymer as a core-shell structure, in which multiple concentric shells of different densities are considered. We also took into account the size distribution of the scattering particles by modeling the intensity scattered from a poly-disperse system:

$$I_{PCS}(Q) = I_0 \int_0^\infty D_n(R) P(Q, R) dR \tag{4.3}$$

where I_0 is an intensity scaling factor and $D_n(R)$ is a Gaussian distribution:

$$D_n(R) = exp\left[-\left(\frac{R - \langle R\rangle^2}{2\sigma^2}\right)\right] \tag{4.4}$$

where $\langle R\rangle$ is the average radius that accounts for the poly-dispersity in size (not mass), $\delta = \sigma/\langle R\rangle$. The form factor for the core shell model is:

$$\begin{aligned} P(Q,R) = \Bigg[&\frac{4\pi R_C^3}{3}(\rho_C - \rho_{S1})\Phi(QR_C) + \\ &\frac{4\pi R_{S1}^3}{3}(\rho_{S2} - \rho_{S2})\Phi(QR_{S1}) + \\ &\frac{4\pi R_{S2}^3}{3}(\rho_{S2} - \rho_{solv})\Phi(QR_{S2})\Bigg]^2 \end{aligned} \tag{4.5}$$

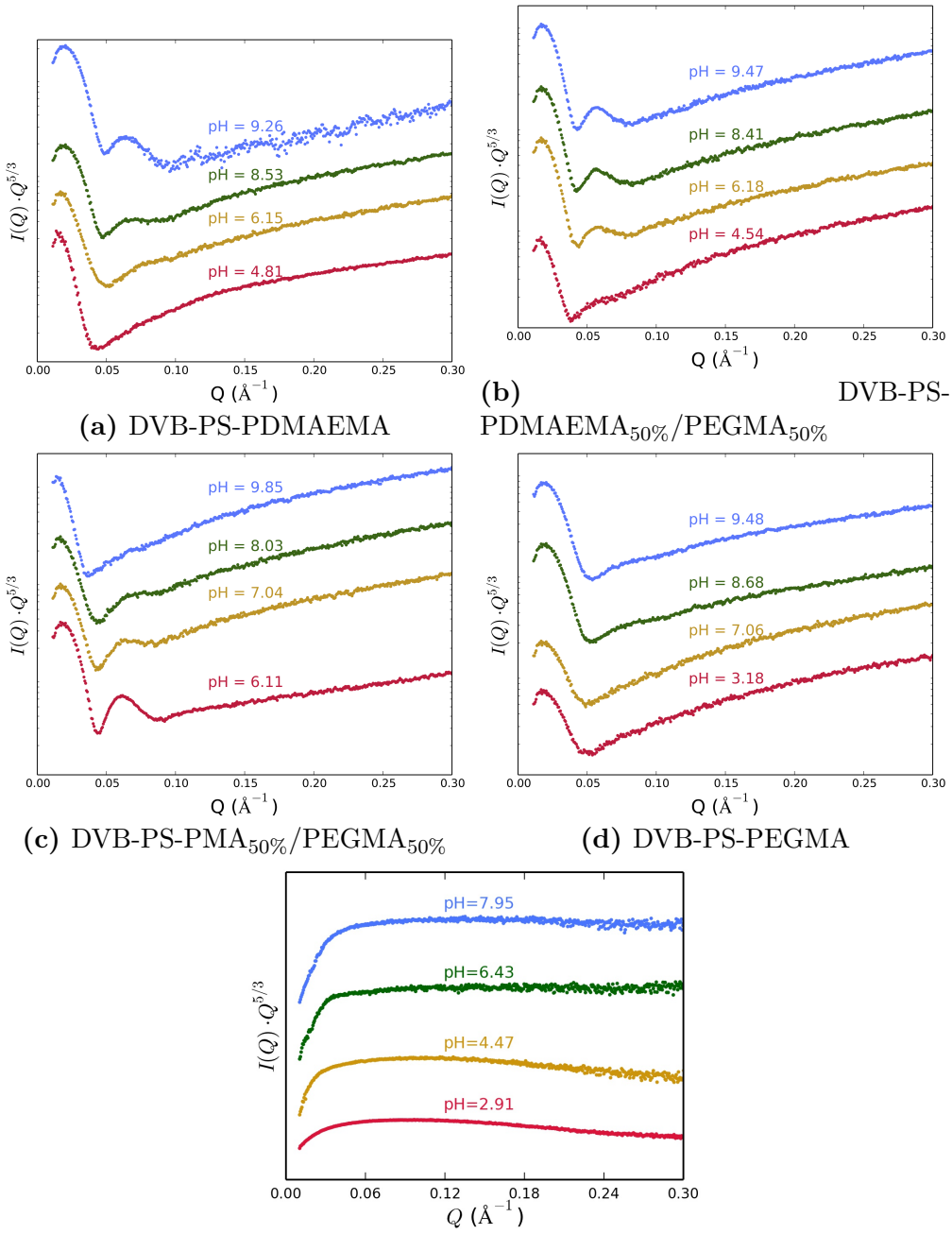

(a) DVB-PS-PDMAEMA **(b)** DVB-PS-PDMAEMA$_{50\%}$/PEGMA$_{50\%}$

(c) DVB-PS-PMA$_{50\%}$/PEGMA$_{50\%}$ **(d)** DVB-PS-PEGMA

(e) DVB-PS-PMAA

Figure 4.1: The Kratky plot of I*$Q^{5/3}$ vs. Q for selected stars at four pH values for (a) DVB-PS-PDMAEMA, (b) DVB-PS-PDMAEMA$_{50\%}$/PEGMA$_{50\%}$ (c) DVB-PS-PMA$_{50\%}$/PEGMA$_{50\%}$ (d) DVB-PS-PEGMA (e) DVB-PS-PMAA. Data are shifted by a multiplication factor for clarity.

where RC is the radius of the core, RS_i the radius of the i^{th} shell from the core, ρ_C is the scattering length density of the core, ρS_i is the scattering length density of the i^{th} shell from the core, ρ_{solv} is the scattering length density of the solvent, and Φ, the normalized amplitude scattered by a sphere, is computed as follows:

$$\Phi(QR) = 3\left[\frac{sin(QR) - QRcos(QR)}{QR^3}\right] \tag{4.6}$$

We used 9.4*10^{-6} Å^{-2} for the scattering length density (SLD) of H_2O when fitting the data with the PCS model. The NIST calculator (https://www.ncnr.nist.gov/resources/sldcalc.html) was used to obtain initial estimates of the SLD for each polymer core or shell region.

Finally, the GCEV model for the scattering of an isolated ideal Gaussian coil in solution [117] involves a semi-analytical functional form:

$$P(Q, R_g, z) = \frac{1}{zU^{1/2z}}\gamma\left(\frac{1}{2z}, U\right) - \frac{1}{zU^{1/z}}\gamma(\frac{1}{z}, U) \tag{4.7}$$

where z is the excluded volume parameter, $\gamma(x, U)$ is the incomplete gamma function:

$$\gamma(x, U) = \int_0^U dt\, exp(-t)t^{x-1} \tag{4.8}$$

and the variable U is a function of Q and the fit parameters z and R_g :

$$U(Q, R_g, z) = \frac{Q^2R_g^2(2z+1)(2z+2)}{6} \tag{4.9}$$

For all of the series studied, with the exception of DVB-PS-PMAA, there is an evident transition at a particular pH that depends on the absence or presence of a peak in the data at Q $\sim$ 0.04 - 0.06 Å^{-1}, which corresponds to a better fit obtained with a Dozier or PCS model, respectively. By contrast, the DVB-PS-PMAA series was instead fit solely by the GCEV model since no structural transition is evident, and furthermore the intensity is dominated by repulsive intermolecular correlations.

Results

Figure 4.2 shows the trend in the SAXS intensity for the DVB-PS-PEGMA star polymer when titrated over a large pH range; the inset shows the trend in R_g as a function of pH based on the fits to the SAXS data using the analytical Dozier model (Table 4.2). Although PEGMA is well known to be temperature sensitive, it is expected that it will be unresponsive to any pH changes, and this is born out in Figure 4.2 inset that shows that the R_g remains constant throughout the titration.

It is interesting to note that the DVB-PS-PEGMA star is well-fit by the Dozier model of a swelled star polymer - a model which is better able to resolve the smaller scale structure

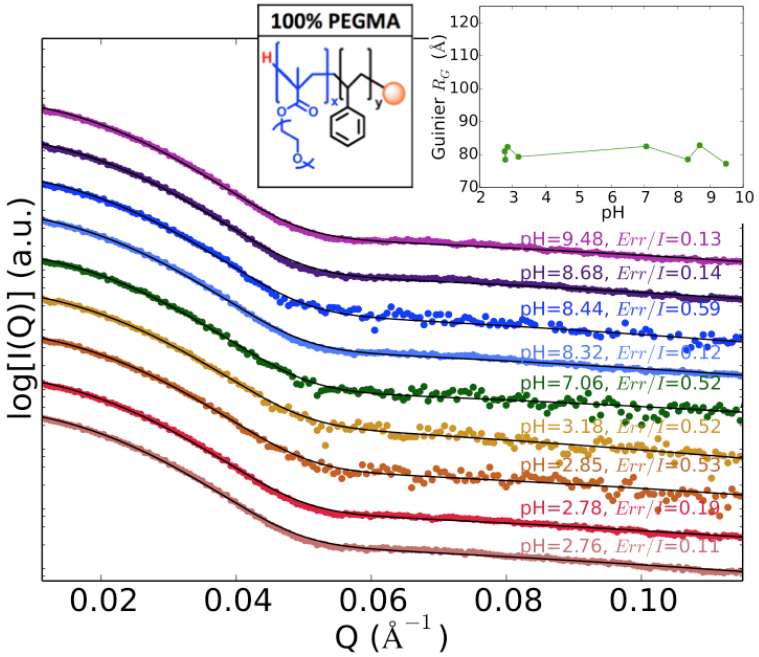

Figure 4.2: *Measured scattering curves for DVB-PS-PEGMA series in water from pH 9.48 (top) to pH 2.76 (bottom).* Experimental data are shown by colored dots and are shifted by a multiplication factor for clarity. Black solid lines are fits to the Dozier model, with the parameters given in Table 4.2. A metric of the experimental error is given by max(Err(Q)/I(Q)). The insert depicts the measured Guinier R_g for the 100% PEGMA series as a function of pH. The DVB-PS-PEGMA star polymer is composed of a cross-linked DVB core (orange), with diblock arm chemistries comprised of an inner hydrophobic polystyrene block (black with y = 33), and outer hydrophilic PEGMA region (blue with x=30).

in the higher Q regions manifested as blob scattering from individual arm chains that are more solvent exposed. This property of DVB-PS-PEGMA is well appreciated, and we have shown previously [59] using molecular dynamics on a related PEG star polymer, that the thermodynamic origins of a structural transition as temperature increases is consistent with entropy-driven dehydration such that below the lower critical solution temperature the PEG arms act like a Gaussian random coil. Thus the DVB-PS-PEGMA star polymer serves as a reference point for introduction of monomer units that are in fact sensitive to pH.

Figure 4.3a shows the trend in the SAXS intensity when titrated over a pH range from 3.18-9.26 for the basic star polymer in which 100% of the PEGMA units are replaced by PDMAEMA; the inset shows the trend in R_g as a function of pH for DVB-PS-PDMAEMA based on the fits to the SAXS data using the analytical models (Table 4.3). It is seen that there is a relatively sharp transition in the size of the basic star polymer as pH decreases near pH$\sim$5.5-6.0, in line with estimates of the apparent pK_a shown in the titration curve in Figure 4.3b. While the $pK_{a,app}$ of the DMAEMA monomer is $\sim$8.4, previous studies have indicated a greater ease in deprotonation for linear forms of the PDMAEMA polymer

relative to the DMAEMA monomer due to electrostatic repulsions between charged groups along the chain that shifts the $pK_{a,app}$ to a smaller value of ∼7.0-7.2 [118, 119]. This $pK_{a,app}$ shifts to even smaller values for a reported PDMAEMA star polymer (5.8-6.3) [24] due to greater electrostatic repulsion between the arms imposed by the star polymer architecture.

However, Figure 4.4a shows that random replacement of half of the PEGMA monomers with DMAEMA results in a sharp structural transition (as measured by R_g values) at even lower pH than measured for the 100% DMAEMA substituted polymers. This is supported by two independent pieces of evidence. First is that the intensity is well fit by the PCS form factor above pH∼4.5, while below this pH value the polymer swells as evidenced by the need to reproduce the high-Q intensity data with the Dozier form factor (Table 4.4). In addition, based on the main equivalence point in Figure 4.4b, we estimate the $pK_{a,app} \sim 4.5$. Therefore any available hydronium ions merely contribute to lowering the pH of the solution, until a pH of 4.5 when the PDMEAMA now becomes protonated and causes significant swelling of the star polymer. This would be consistent with the study conducted on the linear form of the random PDMAEMA-PEGMA co-polymer that showed an increase in the LCST as the proportion of PEGMA increased at any pH, which disappeared entirely at a pH=4 for the linear $PDMAEMA_{50\%}/PEGMA_{50\%}$ polymer [120].

The 50% acidic star polymer, DVB-PS-$PMAA_{50\%}/PEGMA_{50\%}$, shows the opposite trend in the SAXS intensity profile and fits (Figure 4.5a and Table 4.5) as a function of pH relative to any of the basic series of polymers when titrated over a pH range from 5.18-9.6. We would expect the acidic star polymer to become negatively charged at pH values above the usual estimate of the $pK_{a,app}$ ∼4 for polymethacrylate acid, but the introduction of PEGMA clearly has modulated this response so that the conjugate base form of PMAA is not realized until much larger pH values above ∼7.5; this again is supported by the titration curve in Figure 4.5b. To put this remarkable result into perspective, for the linear polymer architecture the hydrogen bonding between the protonated form of PMAA with PEG results in weakly stable interpolymer complexes [121, 122], that dissemble just above the usual $pK_{a,app}$ for PMAA. When PMAA and PEG are put together as a diblock linear polymer the intramolecular interactions stabilize the protonated form to slightly larger pH values up to ∼5.5. [123] However, when PMAA and PEGMA are placed onto a star polymer architecture, the effective increase in functional group concentration contributes to multiple hydrogen-bonding interactions that act to resist deprotonation of the PMAA over a much larger pH range, with a structural transition to the extended form delayed until well into the high pH values.

By contrast, the DVB-PS-PMAA star polymer shows no distinct structural transition as a function of pH in either the SAXS intensity (Figure 4.6) or fit to the GCEV model (Table 4.6). There is overall no clear trend in the R_g of the polymer as a function of increasing pH, which is partly due to numerical noise arising from the extrapolation of each Q point to zero concentration to remove the stronger repulsive intermolecular correlations that dominate the SAXS intensity. Nonetheless, the overall size of the 100% acidic star polymer is greatly expanded at all pH values relative to the 50% acidic star polymer, and further supports the conclusion that PEGMA modulates the structural transition by complexation with PMAA.

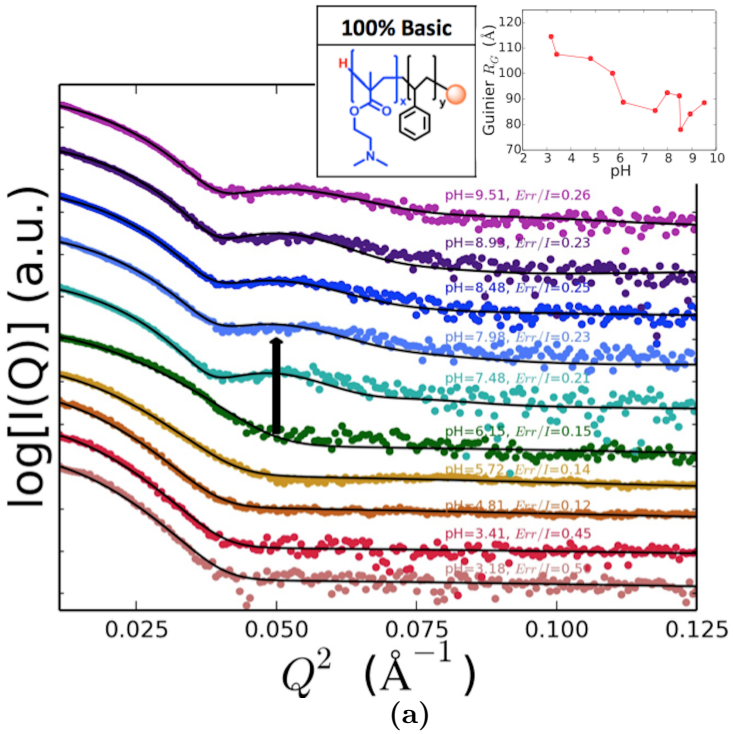

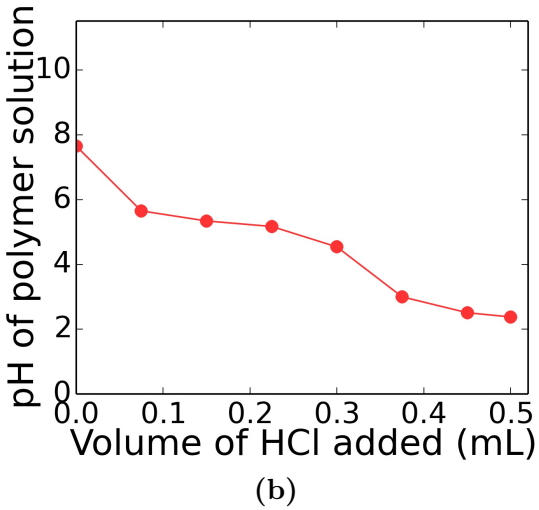

Figure 4.3: *(a) Measured scattering curves for DVB-PS-PDMAEMA series in water from pH 9.26 (top) to pH 3.18 (bottom) and (b) corresponding titration curve for DVB-PS-PDMAEMA.* Black solid lines are fits to Dozier or PCS model, with the parameters given in Table 4.3. The arrow indicates the transition from the Dozier to PCS model fit with increasing pH. The insert depicts the measured Guinier R_g for the 100% Basic series as a function of pH. The outer hydrophilic block is PDMAEMA (blue with x=30); see Figure 4.2 caption for other details.

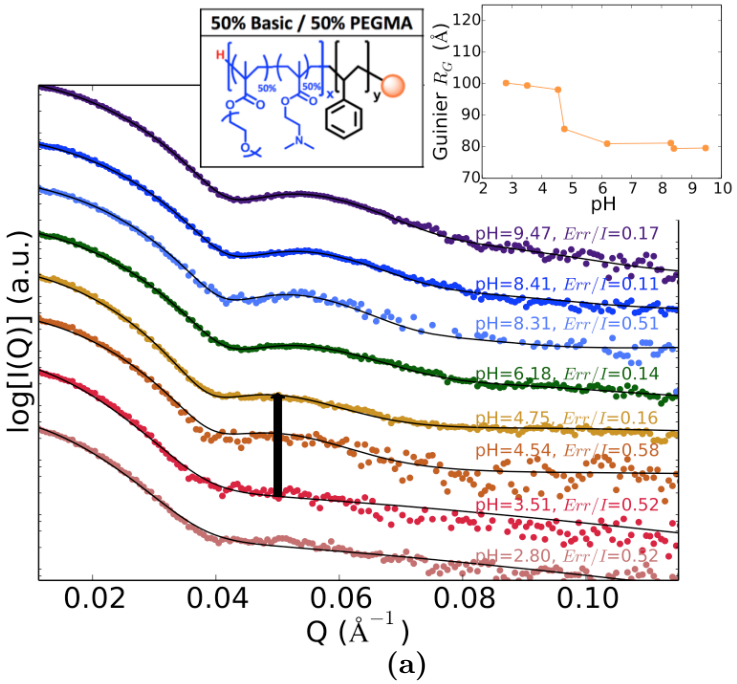

(a)

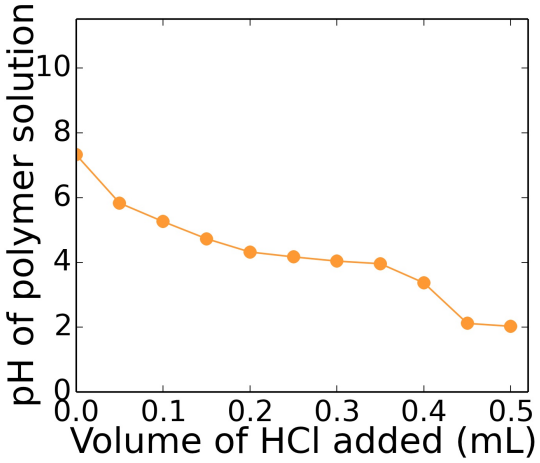

(b)

Figure 4.4: *(a) Measured scattering curves in water from pH 9.47 (top) to pH 2.80 (bottom) and (b) corresponding titration curve for DVB-PS-PDMAEAA$_{50\%}$/PEGAA$_{50\%}$ series* Black solid lines are fits to Dozier or PCS model, with the parameters given in Table 4.4. The arrow indicates the transition from the Dozier to PCS model fit with increasing pH. The insert depicts the measured Guinier R_g for the 50% basic series as a function of pH. The outer block is a random copolymer with PDMAEAA$_{50\%}$/PEGAA$_{50\%}$ region (blue with x=30); see Figure 4.2 caption for other details.

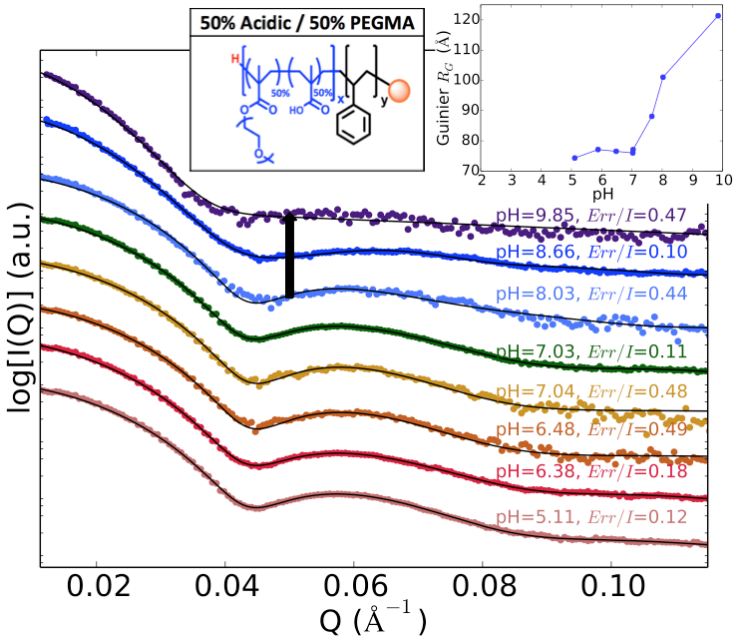

(a)

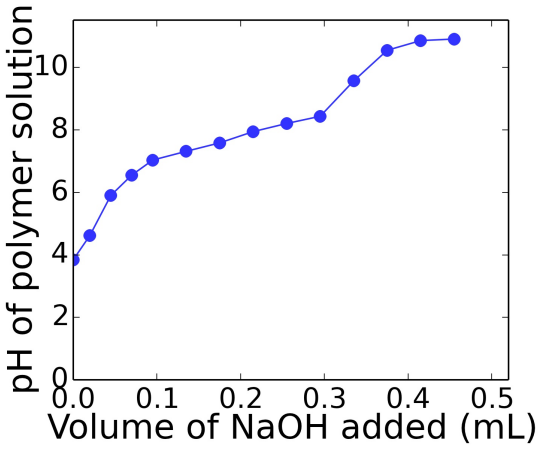

(b)

Figure 4.5: *(a) Measured scattering curves from pH 9.85 (top) to pH 5.11 (bottom), and (b) corresponding titration curve for DVB-PS-PMAA$_{50\%}$/PEGAA$_{50\%}$ series in water.* Black solid lines are fits to Dozier or PCS model, with the parameters given in Table 4.5. The arrow indicates the transition from the PCS to Dozier model fit with increasing pH. The insert depicts the measured Guinier R_g for the 50% Acidic series as a function of pH. The outer block is a random copolymer with PMAA$_{50\%}$/PEGAA$_{50\%}$ region (blue with x=30); see Figure 4.2 caption for other details.

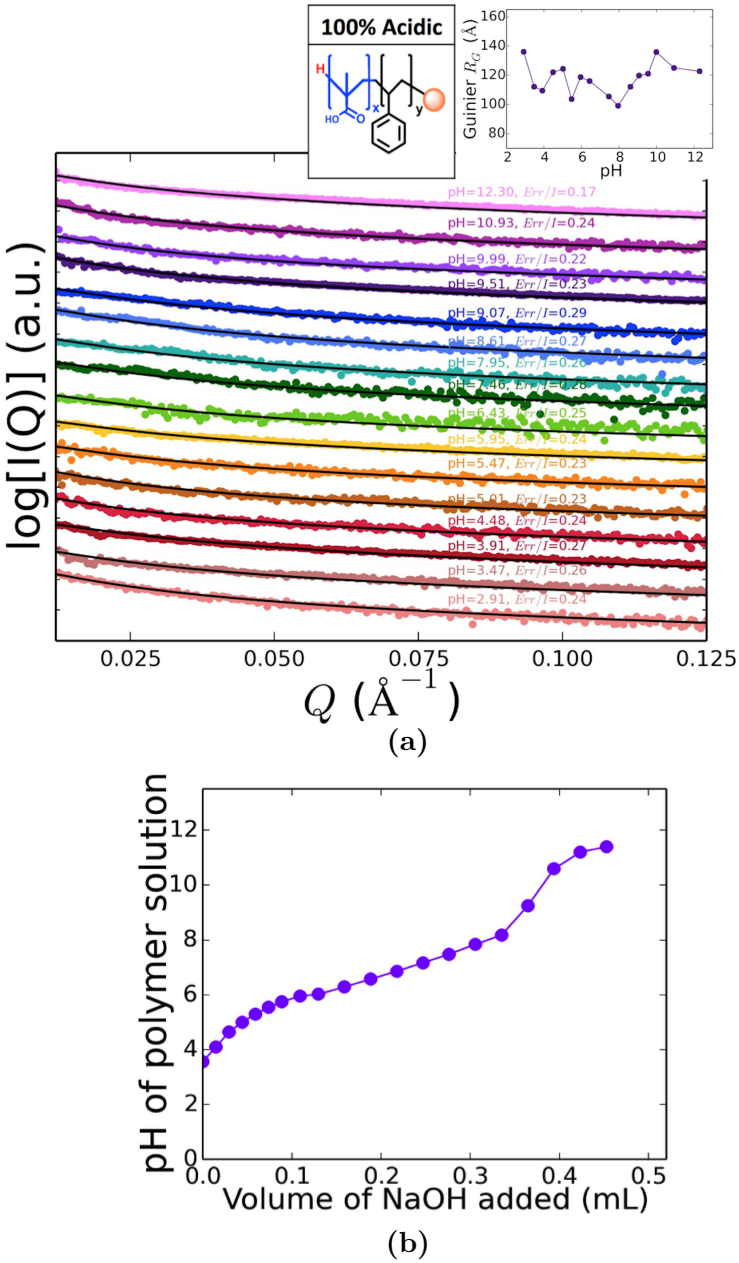

Figure 4.6: *(a) Measured scattering curves from pH 12.30 (top) to pH 2.91 (bottom), and (b) corresponding titration curve for DVB-PS-PMAA series in water.* Black solid lines are fits to Dozier or PCS model, with the parameters given in Table 4.5. The arrow indicates the transition from the PCS to Dozier model fit with increasing pH. The insert depicts the measured Guinier R_g for the 50% Acidic series as a function of pH. The outer block is a random copolymer with $PMAA_{50\%}/PEGAA_{50\%}$ region (blue with x=30); see Figure 4.2 caption for other details.

Discussion and Conclusions

While the DVB-PS-PEGMA and DVB-PS-PMAA polymers showed no structural transition as a function of pH, we found that a pH sensitive change was observed in the SAXS intensity that indicate the collapse or expansion of the polymeric arms for DVB-PS-PDMAEMA, DVB-PS-$PMAA_{50\%}$/$PEGMA_{50\%}$, and DVB-PS-$PDMAEMA_{50\%}$/$PEGMA_{50\%}$. What is surprising is that the structural transition is triggered at pH values that can be quite different when compared to the pK_a of the monomer unit or pK_a of the linear forms of highly similar polymer compositions or even star architectures.

One interesting aspect of the nanogel stars investigated here relative to these other stars of traditional core structure is that the presence of a hydrophobic block (PS) connected to the DVB core results in an expanded hydrophobic region, presumably with a larger surface area from which the corona arms extend. The increased surface area of the core should lead to less interaction between the arms than would be encountered if instead they would be connected at a point as is the case with the tight cross-linked core PDMAEMA star polymer [24]. Therefore, it is reasonable to expect that the apparent pK_a value for the nanogel core DVB-PS-PDMAEMA star polymer should be somewhere in between the values reported for linear PDMAEMA (7.0-7.2) [118, 119] and the small core PDMAEMA star polymer (5.8-6.3) [24]. The fact that we measure the structural transition to larger R_g between pH$\sim$6.0-7.0, illustrates the interesting result that one can dial in pH-induced structural transitions through properties of the star polymer core.

The shift in apparent pK_a for the PDMAEMA-PEGMA is particularly unexpected. In principle, the dilution of the amine in the polymer by the PEGMA unit should have the effect of slightly increasing the $pK_{a,app}$ which means that the size change should occur at higher pH, which it clearly does not. If there was a stabilizing complexation between the protonated amine and the PEG, this also should have the effect of raising the apparent $pK_{a,app}$ relative to the homopolymer; this also doesn't seem to happen since the size transition occurs below pH 5. There is no direct evidence of complexation reported between PEGMA and DMAEMA units at higher pHs which would result in a decrease in the apparent basicity and a shift in the pH curve. There is literature evidence of complexation between quaternary amine functionality and PEG units [124] and hence presumably also between protonated amino substituents, but this would result in an increase of the apparent basicity of the dimethylamino substituted polymer, and again a curve shift to more basic pHs which is not observed by the SAXS dimensional changes nor the titration curves. Instead we can only attribute our observations to an indirect effect based on the preference of the highly hydrophilic PEGMA for the basic form of PDMAEMA since both can form good hydrogen-bonding interactions with water.

The direct stabilization of the neutral form of PMAA by PEGMA up to very high pH values is reminiscent of the large shifts in pK_a observed for amino acids such as histidine ($pK_a\sim6$), whose protonated acidic form is stabilized by ion-dipole interactions with aspartic acid, thereby shifting histidines pK_a to $\sim$12, to create a so-called his-asp dyad that can serve as a catalytic base for many enzymes. Similarly, this has been observed previously in studies

that report the contraction of a PMAA membrane as a function of increasing PEG content [125]; as the PEG content increased, the PMAA membrane contracted more extensively over a shorter period of time. For the 100% acidic series on the other hand, there is no notable collapse, only an increase in repulsion between star polymers as a function of increasing pH, emphasizing that compositional changes in PEGMA fraction can further fine tune the desired pH at which the structural transition occurs.

It should be noted that these experiments were performed at room temperature, whereas for the targeted application of these systems, the polymers will be at physiological temperatures of approximately 37°C. The interplay between temperature and pH may have a complex effect on the pK_as reported here. The dual sensitivity of systems to temperature and pH has been studied before [126, 127], some systems resulting in independent influences of the two system parameters [128], others suggesting interplay between the two stimuli [129]. Of the polymer systems included in this study, both PDMAEMA and PEGMA are known to have lower critical solution temperatures (LCST), a temperature above which the polymer condenses out of solution. The LCST of linear PDMAEMA has been reported as 50°C [130] and that of linear PEGMA may be modulated in the range of $80 - 90$°C as a function of PEG side-chain length [131]. Generally, as the temperature is increased room temperature to that of physiological conditions, the extent of the pH collapse of the reported polymers may be modulated, for as the polymer nears its LCST, the polymer will be less solvated and therefore smaller. However, these effects are quite varied and have high dependence on several factors including polymer architecture and the length of polymer chain. It is recommended that the interaction between temperature and pH sensitivity be considered for future studies.

In summary, we find that properties of the star polymer core and/or arm chemistry can be used to induce a sharp structural transition over a narrow range of pH, an interpretation that is supported by the corresponding titration curves of all star polymers investigated. While the effect is often easily understood by complexation between the monomer components at lower (higher) pHs and an increase (decrease) in the apparent pK_a, this has not been demonstrated previously in a star polymer.

Acknowledgements

This work was supported by the Director, Office of Science, Office of Basic Energy Sciences, of the U.S. Department of Energy under Contract No. DE-AC02-05CH11231. LF was supported by the National Science Foundation Graduate Research Fellowship under Grant No. DGE 1106400 and AD was supported by the Amgen scholars program. The SAXS work was conducted at the Advanced Light Source (ALS), a national user facility operated by Law-rence Berkeley National Laboratory on behalf of the Department of Energy, Office of Basic Energy Sciences, of the U.S. DOE under Contract No. DE-AC02-05CH11231, as well as through the Integrated Diffraction Analysis Technologies (IDAT) program, supported by DOE Office of Biological and Environmental Research, with additional support comes from

the National Institute of Health project MINOS (R01GM105404). This work benefited from SasView software, originally developed by the DANSE project under NSF award DMR-0520547.

Appendix

	Form Factor			
	Guinier	Star Polymer		Fit
pH	Rg (Å)	α	ξ (Å)	ξ^2/Npts
2.76	80.98	2.19	12.09	0.95
2.78	82.33	1.99	11.26	0.94
2.85	78.45	1.98	11.47	0.38
3.18	79.31	2.11	11.75	0.38
7.06	78.50	1.95	11.23	0.49
8.32	82.47	2.06	11.38	0.97
8.44	77.21	2.01	11.55	0.78
8.68	82.82	2.21	11.84	1.00
9.48	84.65	2.13	12.11	0.93

Table 4.2: *The form factor and fitting parameters for DVB-PS-PEGMA series.* The Guinier region was fit to Q*I(Q) <1.3.

	Form Factor							
	Guinier	Star Polymer		Polydisperse Core Shell				Fit
pH	Rg (Å)	α	ξ (Å)	R_C (Å)	R_{S1} (Å)	R_{S2} (Å)	Rg (Å)	ξ^2/Npts
3.18	114.51	2.10	13.20					0.65
3.41	107.55	2.01	12.37					0.60
4.81	105.91	2.03	12.83					0.97
5.72	100.12	2.00	15.84					0.56
6.15	88.78	1.83	10.34					0.78
7.48	85.49			52.30	30.10	28.90	83.31	0.80
7.98	92.47			56.15	30.50	28.70	91.93	1.01
8.48	91.25			53.00	34.40	36.65	89.47	0.98
8.93	84.16			50.06	30.49	32.01	80.66	0.88
9.51	88.57			49.15	30.72	36.52	84.11	0.70

Table 4.3: *The form factors and their fitting parameters for the 100% basic DVB-PS- PDMAEMA series.* The Guinier region was fit to Q*I(Q) <1.3. When fitting the data with the PCS model, we used $SLD = 9.4 \times 10^{-6}$ Å^{-2} for water. The scattering length density (SLD) was determined to be <SLD RC >=9.94; <SLD RS1>=8.48; <SLD RS2>=10.32.

	Form Factor							
	Guinier	**Star Polymer**		**Polydisperse Core Shell**				**Fit**
pH	**Rg (Å)**	α	ξ (Å)	$\mathbf{R_C}$ (Å)	$\mathbf{R_{S1}}$ (Å)	$\mathbf{R_{S2}}$ (Å)	**Rg (Å)**	ξ^2**/Npts**
2.80	100.22	1.91	14.69					1.00
3.51	99.42	1.89	15.45					0.99
4.54	98.11	1.83	15.33					0.98
4.75	85.65			55.79	33.81	46.48	80.19	0.99
6.18	80.99			59.85	29.31	45.14	76.51	0.45
8.31	81.17			46.43	39.93	46.12	76.12	0.79
8.41	79.45			51.13	22.23	41.62	73.76	0.82
9.85	79.60			56.19	19.94	30.41	74.23	0.42

Table 4.4: *The form factors and their fitting parameters for the 50% basic* $DVB - PS - PDMAEMA_{50\%}/PEGMA_{50\%}$ *series.* The Guinier region was fit to Q*I(Q) <1.3. When fitting the data with the PCS model, we used $SLD = 9.4 \times 10^{-6}$ Å^{-2} for water. The scattering length density (SLD) was determined to be <SLD RC >=9.96; <SLD RS1>=8.55; <SLD RS2>=10.25.

	Form Factor							
	Guinier	**Star Polymer**		**Polydisperse Core Shell**				**Fit**
pH	**Rg (Å)**	α	ξ (Å)	$\mathbf{R_C}$ (Å)	$\mathbf{R_{S1}}$ (Å)	$\mathbf{R_{S2}}$ (Å)	**Rg (Å)**	ξ^2**/Npts**
5.11	74.33			38.71	46.45	38.52	71.17	0.43
6.38	77.12			41.69	39.20	41.88	72.56	0.97
6.48	76.54			37.26	47.49	42.52	75.55	0.35
7.03	76.00			38.08	47.49	40.79	74.60	0.56
7.04	77.10			43.30	38.28	43.89	73.12	0.44
8.03	88.10			36.62	44.41	42.72	82.01	0.88
8.66	101.04	2.22	13.01	41.57	41.48	56.83	139.88	1.14
9.85	121.35	2.24	11.13					0.86

Table 4.5: *The form factors and their fitting parameters for the 50% acidic* $DVB - PS - PMAA50_{50\%}/PEGMA_{50\%}$ *series.* The Guinier region was fit to Q*I(Q) <1.3. When fitting the data with the PCS model, we used $SLD = 9.4 \times 10^{-6}$ Å^{-2} for water. The scattering length density (SLD) was determined to be <SLD RC>=9.90; <SLD RS1>=8.43; <SLD RS2>=10.15.

	Form Factor			
	Guinier	**Excluded volume polymer**		**Fit**
pH	**Rg (Å)**	**Rg (Å)**	ν	ξ^2**/Npts**
2.91	136.10	127.75	0.588	0.98
3.47	112.14	102.42	0.588	0.83
3.91	109.45	95.23	0.588	0.75
4.48	122.06	132.00	0.588	0.99
5.01	124.42	123.05	0.588	0.94
5.47	103.66	102.45	0.588	0.91
5.95	118.76	97.23	0.588	0.95
6.43	116.04	102.13	0.588	0.89
7.13	124.64	101.13	0.654	0.99
7.46	105.46	100.21	0.588	0.95
7.95	99.12	103.42	0.588	0.92
8.61	112.13	107.21	0.588	0.84
9.07	119.81	112.34	0.588	0.99
9.55	121.04	125.19	0.588	0.65
9.99	135.86	135.61	0.588	0.74
10.93	125.04	119.91	0.588	0.84
12.30	122.74	111.68	0.588	0.88

Table 4.6: *The form factors and their fitting parameters for the 100% acidic DVB-PS-PMAA series.* The Guinier region was fit to Q*I(Q) <1.3.

Chapter 5

PB-AM: An Open-Source, Fully Analytical Linear Poisson-Boltzmann Solver

We present the open source distributed software package Poisson-Boltzmann Analytical Method (PB-AM), a fully analytical solution to the linearized Poisson Boltzmann equation, for molecules represented as non-overlapping spherical cavities. The PB-AM software package includes the generation of outputs files appropriate for visualization using VMD, a Brownian dynamics scheme that uses periodic boundary conditions to simulate dynamics, the ability to specify docking criteria, and offers two different kinetics schemes to evaluate biomolecular association rate constants. Given that PB-AM defines mutual polarization completely and accurately, it can be refactored as a many-body expansion to explore 2- and 3-body polarization. Additionally, the software has been integrated into the Adaptive Poisson-Boltzmann Solver (APBS) software package to make it more accessible to a larger group of scientists, educators and students that are more familiar with the APBS framework. [1]

Introduction

The preferential association of biomolecules in the cell, ranging from proteins to nucleic acids to small metabolites, is crucial for cellular function. The first events in the molecular

[1] Reproduced from [132] with permission.

recognition process among multiple molecular constituents involve long-range diffusional association over large spatial scales. However, these dynamical encounters have proved difficult to model at an atomistic level since molecular dynamics is too computationally intensive to capture the large spatial and temporal scales over which many macromolecule associations occur. Fortunately coarse graining of the participating biomolecules and their environment, combined with simulations using stochastic dynamics, can be just as insightful as the all-atom deterministic dynamics. At these scales electrostatic interactions dominate, such that the coarse-graining strategy can rely on the popular Poisson-Boltzmann (PB) continuum mean field treatment that forms the basis of Gouy-Chapman theory [133, 134] in electrochemistry, Derjaguin-Landau-Verwey-Overbeek (DLVO) theory in colloid chemistry [135, 136], and under the low field linearized PB (LPB) approximation, the Debye-Hckel theory in solution chemistry [137].

There is a range of software packages currently available for solving the linearized Poisson-Boltzmann equation (LPBE). Numerical methods, such as finite-difference (FD) and finite-element (FE) packages including APBS [138], DelPhi [139], MEAD [140], UHBD [141], ZAP [142], and modules in Amber [143, 144] and CHARMM [145, 146], handle arbitrary dielectric boundaries by solving the PBE on a grid or mesh. Due to their numerical challenges, many essential features of the PBE were are not treated robustly in these software packages; e.g., the point charge singularity and the enforcement of electrostatic continuity across the dielectric boundary. Another limiting factor of these methods is the tradeoff between grid refinement and accuracy given the $O(m^3)$ scaling for 3D electrostatics, where m is the number of grid points in one dimension. Some of these issues have been mitigated for the energy: charge singularities have been treated with regularization schemes [147], induced surface charges [148] and other decomposition methods [149], molecular surface definitions and discontinuities across that boundary have been addressed with the matched interface and boundary (MIB) method [150] and advanced grid methods are also implemented [144, 151]. However, unlike the energetic terms, force calculations still pose many numerical issues for FE and FD methods. The most definitive method, known as the virtual work approach [152] has been implemented to account for full mutual polarization in FD and FE methods, but is limited by computational efficiency since gradients are calculated numerically, requiring a recalculation for the electrostatic energy after small displacements in each Cartesian direction.

Another approach is the boundary element method (BEM) that is the main feature of software packages such as AFMPB [153], PyGBe [154, 155] and TABI [156]. BEM approaches offer some advantages over FE and FD methods since there is an analytical treatment of singular charges, and explicit treatment of the dielectric discontinuity and boundary conditions. However, BEMs also have some limitations, including an increasingly large dense matrix that scales with system size and has severe memory requirements, singular surface integrals, and issues with mesh generation. In contrast to FD and FE methods, BEMs can efficiently compute forces, but they only include self-polarization as opposed to full mutual polarization, and have yet to be demonstrated as efficient enough for dynamical simulations. An alternative to the numerical FE, FD, and BEM methods is to consider analytical so-

lutions instead. As far as we are aware, the first analytical LPBE solution was solved by Kirkwood for one spherical macromolecule [157]. However the treatment to describe mutual polarization requires at least two distinct spheres, and many different partial and approximate solutions to the mutual polarization of two or more macromolecules using the LPBE have been proposed [158–162]. In 2006 Lotan and Head-Gordon derived the first completely general analytical solution to the LPBE [1], including the forces and torques due to this potential, that permits analytical calculations to arbitrary large assemblies of interacting molecules. While the primary drawback of the analytical solutions are that they are restricted to idealized geometries such as spheres, they do have the benefit that the boundary conditions are solved completely, and for the Poisson-Boltzmann analytical model (PB-AM) [1] the mutual polarization is accounted for accurately.

While the PB-AM model [1] is computationally efficient, we believe that the models theoretical formalism has made it inaccessible to many and inhibited its potential use for application on a large scale. Here we present an expanded, open-source software implementation of PB-AM, as well as a number of python-based utilities for creating files for multi-dimensional visualization for the electrostatic potential and forces and torques, a Brownian Dynamics simulation module that models the stochastic dynamics of multiple macromolecule interactions [163–165], the ability for users to define docking criteria and to simulate biomolecular association rate constants, as well as exploration of the many-body expansion (MBE) for the mutual polarization [166]. The PB-AM open source software is easy to download and install and has a simple input file structure and modular design to encourage both ease of use and extensibility to other software packages. Additionally, the PB-AM model has been integrated into the Adaptive Poisson-Boltzmann Solver (APBS) (http://www.poissonboltzmann.org/) to allow accessibility of the PB-AM capabilities to a larger group of scientists, educators and students.

The paper is organized as follows. After a brief review of the PB-AM theory developed by Lotan and Head-Gordon in Section 2, we describe the software framework of the PB-AM stand-alone code and its integration into the APBS software package in Section 3. In Section 4 we demonstrate the PB-AM softwares visualization outputs for the electrostatic potential using 2D cross-sections as well as 3D isosurfaces that feed into the Visual Molecular Dynamics [81] (VMD) program. In Section 5 we introduce the dynamics capabilities using PB-AM that utilizes a standard Brownian dynamics scheme, permits users to define docking criteria, and offers two distinct ways to calculate bimolecular rate constants, one of which is especially suited to simulations involving large number of molecules. In Section 6 we introduce the many-body expansion (MBE) that allows the mutual polarization to be deconstructed into a direct polarization model, as well as approximate mutual polarization models. Finally we provide a brief summary in Section 7 and plans for future work.

PB-AM Theory

The derivation details of PB-AM have been reported previously [1], but the main points can be summarized as follows. The electrostatic potential of the system at any point $\mathbf{t}$ is governed by the linearized form of the Poisson-Boltzmann equation

$$\nabla \cdot [\epsilon(\mathbf{t})\nabla\Phi(\mathbf{t})] - \epsilon(\mathbf{t})\kappa^2\Phi(\mathbf{t}) = 4\pi\rho(\mathbf{t}) \tag{5.1}$$

For the case of spherical cavities, we can solve Equation 5.1 by dividing the system into inner sphere and outer sphere regions, and enforcing a set of boundary conditions that stipulate the continuity of the electrostatic potential and the electrostatic field at the surface of each sphere. The electrostatic potential inside molecule i is described by:

$$\Phi_{in}^{(i)}(\mathbf{t}) = \sum_{n=0}^{\infty}\sum_{m=-n}^{n}\left(\frac{E_{n,m}^{(i)}}{\epsilon_p r^{n+1}} + B_{n,m}^{(i)} r^n\right) Y_{n,m}(\theta,\phi) \tag{5.2}$$

where ϵ_p is the interior dielectric, $B^{(i)}$ is a vector of unknowns that will be determined through the application of the boundary conditions, $E^{(i)}$ is the multipole expansion of the charges inside molecule i.

$$E_{n,m}^{(i)} = \sum_{j=1}^{M_i} q_j^{(i)} \left(\rho_j^{(i)}\right)^n \overline{Y_{n,m}}\left(\nu_j^{(i)}, \phi_j^{(i)}\right) \tag{5.3}$$

where M_i is the number of charges in molecule i, q_j is the magnitude of the j-th charge, and $p_j^{(i)} = [\rho_j^{(i)}, \nu_j^{(i)}, \phi_j^{(i)}]$ is its position in spherical coordinates and $Y_{n,m}$ are the spherical harmonics. The general form of the potential outside all molecules (in a coordinate frame whose origin is the center of molecule i) is:

$$\Phi_{out}^{(i)}(\mathbf{t}) = \frac{1}{\epsilon_s}\sum_{n=0}^{\infty}\sum_{m=-n}^{n}\left(\frac{A_{n,m}^{(i)}}{r^{n+1}} e^{-\kappa r}\hat{k}_n(\kappa r) + L_{n,m}^{(i)} r^n \hat{i}_n(\kappa r)\right) Y_{n,m}(\theta,\phi) \tag{5.4}$$

where the coefficients $L^{(i)}$ in Equation 5.4 are a re-expansion of the external potential coefficients $A^{(j)}), j \neq i$ of all other molecules in the system. It is defined as:

$$L^{(i)} = \sum_{j=1, j\neq i}^{N} T^{(i,j)} \cdot A^{(j)} \tag{5.5}$$

where $T^{(i,j)}$ is the linear re-expansion operator that transforms a multipole expansion at $c^{(j)}$ to a local (Taylor) expansion at $c^{(i)}$. This operator is described in detail in our previous work [1]. The use of the $T^{(i,j)}$ operators allows us to represent the potentials due to all molecules in the coordinate frame of a single molecule, a mathematical feature that is central

to obtaining an analytical solution. Since the $B^{(i)}$ depend on $A^{(i)}$, the application of the boundary conditions leads to the following compact solution

$$A = \Gamma \cdot (\Delta \cdot T \cdot A + E) \tag{5.6}$$

Where A is a matrix of vectors, one for each molecule in the system, representing the effective multipole expansion of the charge distributions of each molecule, the Γ matrix is a dielectric boundary-crossing operator, and the Δ matrix is a cavity polarization operator.

Using this formalism, physical properties of the system, such as interaction energy, forces and torques may be computed. The interaction energy of each molecule, $\Omega^{(i)}$, is the product of the molecules total charge distribution (from fixed and polarization charges) with the potential due to external sources. This is computed as the inner product between the molecules multipole expansion, $A^{(i)}$, and the multipole expansions of the other molecules in the system, $L^{(i)}$ as follows:

$$\Omega^{(i)} = \frac{1}{\epsilon_s}\langle L^{(i)}, A^{(j)}\rangle \tag{5.7}$$

which allows us to define the force which is computed as the gradient of the interaction energy with respect to the position of the center of molecule i:

$$F^{(i)} = -\nabla\Omega^{(i)} = -\frac{1}{\epsilon_s}(\langle \nabla L^{(i)}, A^{(i)}\rangle + \langle L^{(i)}, \nabla A^{(i)}\rangle) \tag{5.8}$$

By definition, the torque on a charge in the molecule is the cross product of its position relative to the center of mass of the molecule with the force it experiences. The total torque on the molecule is a linear combination of the torque on all charges of the molecule.

$$\tau^{(i)} = \frac{1}{\epsilon_s}\left[H^{(i),x}, H^{(i),y}, H^{(i),z}\right] \times \left[\nabla_i L^{(i)}\right] \tag{5.9}$$

Please see previous publication [1] for details on the PB-AM solver.

Software Architecture

The stand-alone PB-AM code has been completely re-written from the original code base development [1] in C++11 to include a modular interface, simplified input files, expanded examples, unit testing, and an automated build system (CMake). It also includes a set of utilities, written in Python, to aid in visualization tasks and perform additional simulations. The new Application Programming Interface (API) has been designed to focus on four important utilities of the program: 1) electrostatic potential visualization, 2) energy, force, and torque calculation for molecule-molecule interactions, 3) use of the many-body expansion (MBE) to formulate direct and mutual polarization models, 4) dynamical simulations using Brownian dynamics. The input file structure is simple; each line containing a keyword value pair, in most cases, and for most basic usage, the program can be

run with an input file of 3 lines. Additionally, the outputs have been expanded to formats readable in VMD [81], such as dx and xyz files. Finally, an extensive user manual and website (https://davas301.github.io/pb_solvers/) have been developed with examples and post-processing examples. PB-AM is available for download through the GitHub site: https://github.com/davas301/pb_solvers. Figure 5.1 shows the workflow of the software and its components.

In addition to the stand-alone code, the PB-AM code has been integrated into the Adaptive Poisson-Boltzmann Solver (APBS) software package that solves the equations of continuum electrostatics for large biomolecular assemblages. This software is the central computational element for computational research involving the Poisson-Boltzmann equation and is, a unique software package that solves the equations of continuum electrostatics for large biomolecular assemblages. APBS plays an important role in the structural and computational biology research community and the proposed research ensures its continued availability and support. Specifically, APBS addresses three key technology challenges for understanding solvation and electrostatics in biomedical applications: (1) accurate and efficient theories and models for biomolecular solvation and electrostatics, (2) robust and scalable software for applying those theories to biomolecular systems, and (3) mechanisms for sharing and analyzing biomolecular electrostatics data in the scientific community. PB-AM has been fully integrated into the APBS software. The user invokes the code with a keyword in the ELEC section of an APBS input file. Some additional keywords are required and are documented on the APBS website. The incorporation of PB-AM into APBS will allow for PB-AM to be available to an audience of thousands of users, and is made available through the APBS site: http://www.poissonboltzmann.org/.

Electrostatic Potential Visualization

One of the most popular uses of PBE solvers is to provide rapid analysis of the electrostatic potentials around macromolecules and their assemblies. Therefore, like many other PBE solvers, our PB-AM approach has the capability of producing output files for visualizing the electrostatic potential (ESP) of a system of arbitrary complexity. To this end we have provided several visualization options that a user may select, including two-dimensional ESP cross-sections and isosurface potentials (Figure 5.2), which may be loaded and viewed in the program Visual Molecular Dynamics [81] (VMD). In addition to the electrostatic potentials it is also quite straightforward to visualize of forces and torques on and around the center-of-mass.

Dynamical Trajectories and Analysis Tools

In addition to electrostatics calculations, the PB-AM software includes dynamics capabilities. The computed expressions for force and torque have been incorporated into a Brownian

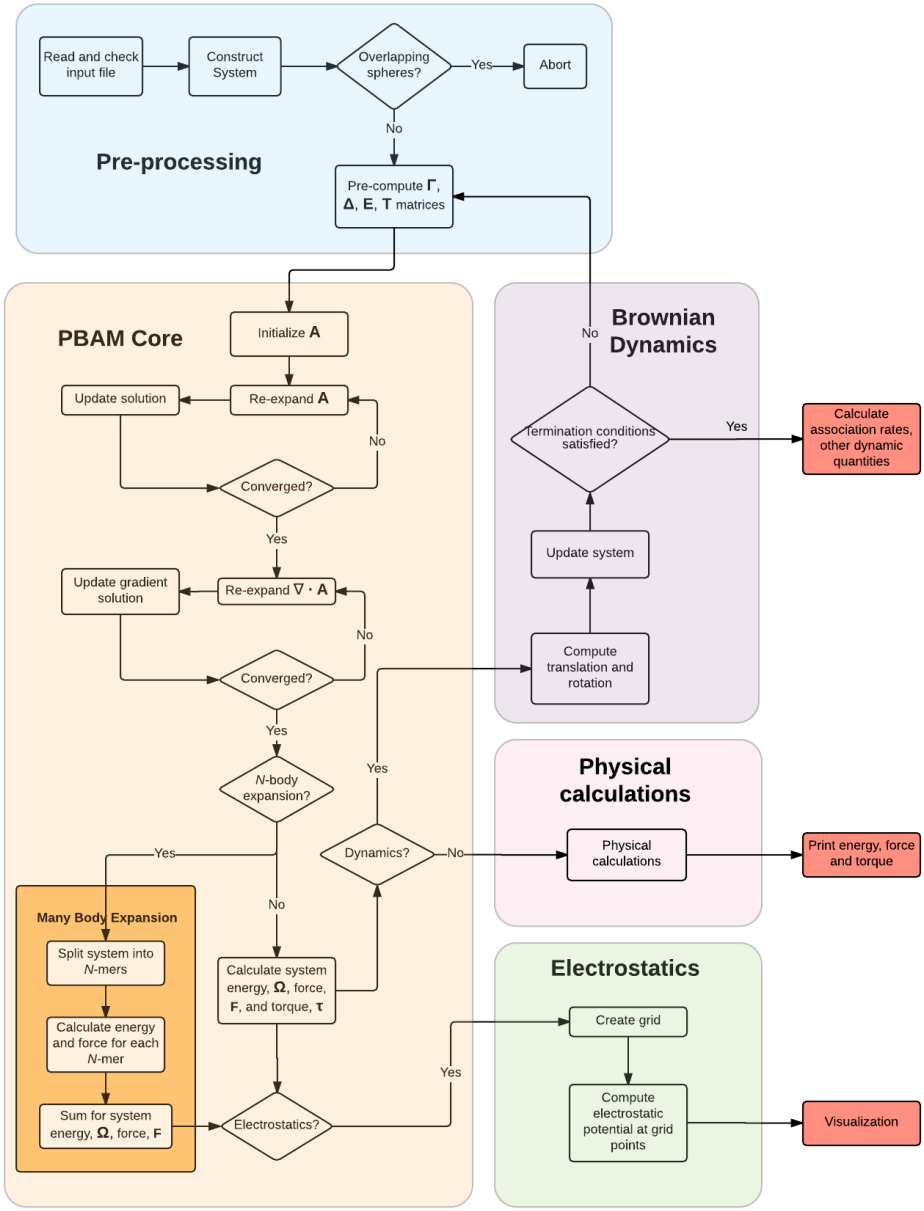

Figure 5.1: *Software workflow for the PB-AM model and its utilities.* The stand alone PB-AM code has been completely re-written from the original development [1] in C++11, and has four important utilities: electrostatic potential visualization, energy, force, and torque calculations for molecule-molecule interactions, use of the many-body expansion to formulate approximate direct and mutual polarization models, dynamical simulations using Brownian dynamics, which can generate many interesting outputs, for example, different ways to calculate rate constants for biomolecule association.

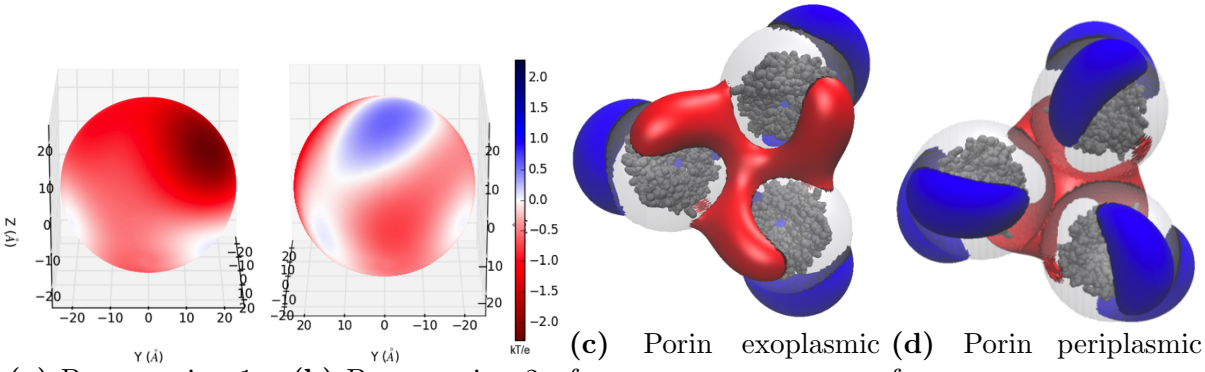

(a) Barnase view 1 **(b)** Barnase view 2 **(c)** Porin exoplasmic face **(d)** Porin periplasmic face

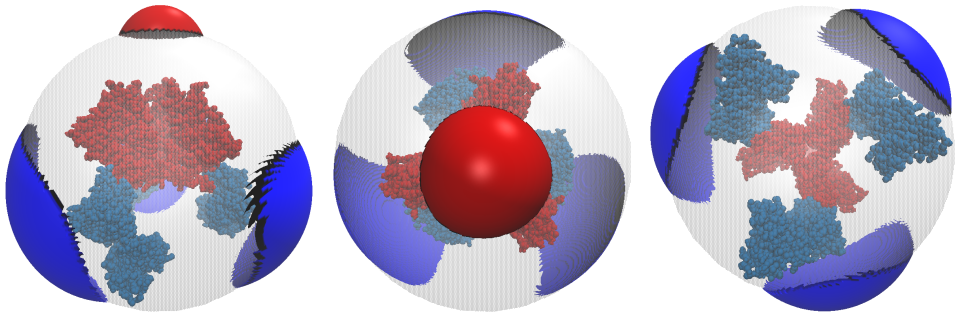

(e) HIV glycoprotein **(f)** HIV glycoprotein **(g)** HIV glycoprotein

Figure 5.2: *Different visualizations of the electrostatic potentials from the PB-AM model.* All systems are at 0.0M salt concentration, 7 pH, with protonation states calculated using PROPKA [167], interior dielectric of 2, and solution dielectric of 78. The blue isosurfaces are drawn at 1.0 k_BT/e and the red at -1.0 k_BT/e. (a, b) 3D surface potential from two different vantage points of the coarse-grained Barstar protein. The molecule has been coarse-grained into a single sphere of radius 21.8 Å that encompasses all molecule atoms, and the potential is depicted at the surface of the coarse-grain sphere. The color scale for each image is given by color bar on the right, in units of k_BT/e. (c,d) 3D isosurfaces for Omp32 Porin trimer from the view of (c) the exoplasmic face (channel entrance). The negative isosurface (red) forms a funnel that can direct anions from the environment towards the channel, (d) The periplasmic face (channel exit). The positive surface (blue) at the channel exit may further enhance anion transport through the channel. The channel proteins are represented by a grey solvent-excluded surface. (e-g) The HIV glycoprotein binds to CD4 proteins (PDB structure 4NCO44) from three vantage points. The upper hemisphere is a virus membrane-spanning portion, while the lower hemisphere is connected to 3 CD4 proteins that extend from the surface of the cell wall. These two distinct binding regions of the protein are distinguished here by the location of the electrostatic potential isosurfaces, with the CD4 creating a positive potential, and the portion attached to virus membrane creating a negative potential.

dynamics simulation protocol adapted from Ermak and McCammon [163]. Each molecule in the system is treated as an independent rigid particle, and molecule-molecule overlap is not allowed. Assuming no hydrodynamic effects, the translational and rotational displacement, Δr_i and $\Delta\theta_i$ respectively, are computed as:

$$\Delta r_i = \frac{D_{trans}\Delta t}{k_B T} f_i + S_i(\Delta t) \tag{5.10}$$

$$\Delta\theta_i = \frac{D_{rot}\Delta t}{k_B T} \tau_i + \Theta_i(\Delta t) \tag{5.11}$$

Where S_i is the stochastic displacement, and Θ_i is the stochastic rotation, have the following properties in dimension $\alpha = x, y, z$:

$$\Delta r_i = \frac{D_{trans}\Delta t}{k_B T} f_i + S_i(\Delta t) \tag{5.12}$$

$$\Delta\theta_i = \frac{D_{rot}\Delta t}{k_B T} \tau_i + \Theta_i(\Delta t) \tag{5.13}$$

The PB-AM software allows a generalized simulation procedure for a variety of terminations conditions, including a) time: the simulation will terminate when it has run for t picoseconds, b) coordinates: the simulation will terminate when a specified particle has diffused beyond a certain point in space specified by the user, c) docking: the simulation will terminate when a pair of specified atoms in the simulated molecules are within a specified cutoff; this docking criteria is specified by the user as a contact list at the start of the simulation. For details on BD simulation in PB-AM, please see our user manual.

One application of dynamics of particular interest is the calculation of bimolecular association rate constants and the ability to specify the docking criteria when association is complete. For the case of PB-AM, which represents each molecule as one hard spherical object, the boundary of the sphere prevents the physical proximity of contact pairs to be defined based on an atomistic geometry. Instead, the locations of the atomistic contact points, from the contact list, are projected onto the surface of the sphere to create a reactive surface patch, and the BD simulation terminates at the docking criteria when these surface patches are within 0.1Å.

For calculations of the rate constants, we have incorporated into the PB-AM software package two independent approaches. The first is the Northrup-Allison-McCammon (NAM) method [168, 169]. The NAM method is based on the Smoluchowski equation, and its underlying assumption is that the mobile molecule B only experiences forces from stationary molecule A; i.e., concentration effects that modulate intra-species interactions A:A and B:B are not taken into account. The NAM method models the rate calculation as an analysis across a series of flux surfaces: an inner region, bounded by a radial distance b, is defined where inter-molecular forces are anisotropic and must be evaluated explicitly with BD. In this region we can numerically evaluate the docking frequency, δ, i.e. the ratio of successfully docked trajectories to total trajectories simulated. For simulated distances outside b, any

inter-molecular forces are approximately centrosymmetric and the diffusion rate constant $k_D(b)$ can be evaluated analytically using the Smoluchowski equation [168].

$$k(R) = \left[\frac{1}{4\pi D_{trans}} \int_R^\infty \frac{exp\left(\frac{U(r)}{k_B T}\right)}{r^2} dr \right]^{-1} \tag{5.14}$$

Beyond the surface at R=b, a second surface at R=q is chosen such that $q >> b$, and the simulation can be truncated, and the diffusional rate beyond q can also be evaluated from the Smoluchowski equation, $k_D(q)$. By accounting for re-crossings across the two flux surfaces at b and q, we can evaluate intrinsic bimolecular collision rate, k, is as follows:

$$k = \left[\frac{k_D(b)\delta}{1 - (1-\delta)\frac{k_D(b)}{k_D(q)}} \right] \tag{5.15}$$

A more accurate rate constant calculation method must also simulate a system with multiple copies of A and B that are allowed to interact with each other. Given that such interactions are dominated by electrostatics at large distances, this demands an efficient algorithm capable of computing the electrostatic forces and torques for multiple molecules on the fly as in PB-AM. In this second approach it is possible to evaluate the mean first passage time (MFPT) under periodic boundary conditions, by considering the second-order rate equation of the association of molecules A and B:

$$\frac{d[AB]}{dt} = k[A][B] \tag{5.16}$$

In this case, the user can specify the concentrations [A] and [B] and the fraction of trajectories docked at time t is given by

$$P_{docked}(t) = \frac{\text{No. of systems with } t_i \leq t}{N} \tag{5.17}$$

At present one can use PB-AM to evaluate the pseudo-first order rate constant k by fitting the plotted data of $P_{docked}(t)$ against t, to the functional form

$$P_{docked}(t) = 1 - exp(-k'(t - \tau_d)) \tag{5.18}$$

where τ_d is the dead time required for the system to equilibrate, and the bimolecular rate constant is computed from

$$k = \frac{k'}{[A]_{t=0}} \tag{5.19}$$

The barnase-barstar association kinetics has been extensively characterized, both experimentally [170] and computationally using the NAM method [171]. We compare the NAM method versus a multi-molecular simulation involving multiple barnase and barstar proteins

Model and Rate Method	[Barnase] (conc [M]):[Barstar] (conc [M])	Rate constant values, k $[M^{-1}s^{-1}]$
Experiment [170]	N/A	$2.86 \pm 0.28 \times 10^8$
Gabdoulline and Wade [171]	1 (5.068×10^{-5}): 1 (5.068×10^{-5})	3.88×10^8
PB-AM using NAM	1 (5.068×10^{-5}): 1 (5.068×10^{-5})	$7.53 \pm 0.25 \times 10^7$
PB-AM using MFPT	124 (6.482×10^{-3}) : 1 (5.068×10^{-5})	$9.58 \pm 0.47 \times 10^7$

Table 5.1: *The barnase-barstar rate of association.* Comparison of estimated rate constants using different PBE models and rate constant protocols NAM and MFPT against experiment and using an atomistic docking criteria from Gabdoulline and Wade.

(125 proteins total). Both systems were performed under the following conditions: T = 298.15 K, dielectric constants of 78 (protein) and 4 (solvent), salt concentration of 0.05 M. A variable time step with a minimum of 2 ps was used. At each time step, the system is solved with a polarization cutoff of 10 Å and a force cutoff of 100 Å. The multi-molecular simulation was run with periodic boundary conditions with a box length of 320 Å to ensure that the minimum image conventions were obeyed. In Table 5.1 we compare these results against PB-AM using both NAM and the multi-protein MFPT simulations, showing that the simplified dielectric boundary is in very good qualitative agreement with past efforts, and thus a useful way to rapidly evaluate kinetics for biomolecule association. In comparison with the results of Gabdoulline and Wade, we believe that differences in computed rate constants are likely due to differences in molecular representations. All other system conditions held constant (protein model, force field, docking definition), the crowding conditions increase the docking rate by approximately ∼20%.

Many-body Expansion of the Electrostatic Energy

The formalism of the PB-AM model allows mutual polarization of all molecules in the system to be treated analytically, but as the number of molecules in the system increases, this N-body problem can become increasingly time intensive. The many-body expansion (MBE) allows us to expand the energy, and forces and torques as well, can be calculated in terms of simpler and independent 1-body, 2-body, 3-body etc. components.

$$U_N = U_1 + \Delta U_2 + \Delta U_3 + \cdots \tag{5.20}$$

where

$$U_1 = \sum_{i=1}^{N} U(i)\,; \quad \Delta U_2 = \sum_{i=1}^{N-1} \sum_{j=i+1}^{N} U(i,j) - U(i) - U(j) \tag{5.21}$$

$$\Delta U_3 = \sum_{i=1}^{N-2} \sum_{j=i+1}^{N-1} \sum_{k=j+1}^{N} U(i,j,k) - U(i,j) - U(i,k) - U(j,k) + U(i) + U(j) + U(k) \tag{5.22}$$

	Timings (s)		
[Barnase]:[Barstar]	**Full Mutual (4 cores)**	**3-body MBE (4 cores)**	**3-body MBE (64 cores)**
7:1	1.07	3.19	0.47
63:1	376.22	185.11	50.81
124:1	2307.71	1612.34	297.01

Table 5.2: *Comparison of timings for full mutual polarization and the MBA.* The systems are comprised of a cubic grid of barnase and barstar molecules, with the given ratio of Barnase to Barstar molecules.

We have shown that the MBE converges quickly at the 2-body level with small Debye lengths, whereas the 3-body truncation of Equation 5.22 is excellent for larger Debye lengths. [166] This allows for a different type of refactoring of the calculations while still leading to a highly accurate approximation to the PB-AM model. The computational benefits to the approach are evident from Table 5.2, using a cubic grid of barnase and barstar molecules, in similar configurations to the MFPT initialization. We can achieve a 2-3X speed-up over the full-calculation using only 4 cores, and if we take advantage of the independent nature of the dimer and trimer calculations and increase the core count to 64, we can increase the speedup to 8X.

Conclusion

We have described the release of the PBE solver, PB-AM, a complete analytical solution for both self- and full mutual polarization, which allows users to analyze electrostatics and stochastic dynamics of complex biomolecular systems, under the assumption of idealized spherical geometries. PB-AM can be downloaded stand-alone or as part of the distributed APBS software package.

Obviously the simple geometric shape of the low dielectric spherical cavity containing the complex charge distribution can result in differences with that of a more detailed molecular shape handled by other LPBE formulations. We have overcome this limitation using our semi-analytic solution to the PBE (PB-SAM) [2, 3] that expands the analytic formalism to describe molecular boundaries, and it will be made available in a future release of the PB-AM software package. Even so, we have demonstrated that meaningful rate constants can be evaluated under the idealized geometries inherent to the PB-AM model, as they were shown to be in good agreement with experiment and the PB-SAM solver that uses realistic geometric boundaries.

As a freely available, open-source package we hope that other users will find value in expanding the capabilities of the PB-AM code. In addition to the future release of PB-SAM, which describes more realistic molecular boundaries, there are other important additions that should be included such as hydrodynamic interactions and other kinetic schemes.

Acknowledgments

THG and DHB were supported by the Director, Office of Science, Office of Basic Energy Sciences, of the U.S. Department of Energy under Contract No. DE-AC02-05CH11231. LF was supported by the National Science Foundation Graduate Research Fellowship under Grant No. DGE 110640. APBS is supported by the National Biomedical Computation Resource, the National Institutes of Health under grant GM069702. Work benefited from VMD software, under award National Institutes of Health grants 9P41GM104601 and 5R01GM098243-02, directed by Klaus Schulten. This research used resources of the National Energy Research Scientific Computing Center, a DOE Office of Science User Facility supported by the Office of Science of the U.S. Department of Energy under Contract No. DE-AC02-05CH11231. THG wishes Charles Brooks III the best on the occasion of his 60th birthday. Since I worked on the Poisson Boltzmann problem as one of the first projects as a graduate student in his group I think it fitting that the current status on PBE solvers be included in his Festschrift!

Chapter 6

PB-SAM: Development of an Open-Source, Semi Analytical Linear Poisson-Boltzmann Solver

We present a software release of the Poisson-Boltzmann Semi Analytical method, a semi-analytical solution to the Poisson-Boltzmann equation (PBE). The updated software includes visualization and simulation methods to study systems of macromolecules in a salty (screened) environment. The software has been updated, and is available open source as a standalone package as well as part of the Adaptive Poisson-Boltzmann Solver (APBS) software package to make it more accessible to a larger group of scientists, educators and students.

Introduction

The representation of biomolecular systems in salty (screened) conditions is crucial for understanding cellular function. Often these initial interactions are driven by long-range, electrostatic forces, so representing these forces accurately with mathematical models can aid research in understanding and predicting the nature of these interactions. Often the scope of these interactions is beyond the computational limits of classical simulations, e.g. molecular dynamics (MD), so coarse-grain (CG) methods have been developed to describe this temporally and spatially long scales, inaccessible by MD. The CG method that this chapter focuses on is called the Poisson-Boltzmann equation (PBE), more specifically the linearized form of the PBE, the linearized Poisson-Boltzmann equation (LPBE).

There is a range of software packages available for solving the LPBE numerically, including finite-difference (FD) or finite-element (FE) methods (APBS [138], DelPhi [139], MEAD

[140], UHBD [141], ZAP [142], and modules in Amber [143, 144] and CHARMM [145, 146]), advantages and challenges of this methodology are given in the previous chapter. In addition to FD and FE methods, boundary element (BE) methods and softwares such as AFMPB [153], PyGBe [154, 155] and TABI [156] offer many advantages in dealing with issues such as charge singularities and explicit description of dielectric boundaries. But their challenge is computational expense. The boundary elements are described with dense matrices which increase in size with the system size.

Finally, fully analytical solutions to the LPBE are generally constrained to spherical and cylindrical domains, including PB-AM, a method previously introduced by Lotan and Head-Gordon [1], and reformulated by Felberg et al [132]. While these models are computationally efficient, they are limited in the complexity of molecular descriptions. For this reason, we have introduced a semi-analytical solution to the LPBE, PB-SAM, that leverages the analytical formalism and BE methods to create an efficient and accurate LPBE solver. The package has been re-written and includes a variety of user tools including electrostatic potential visualization, dynamics simulations and calculations of force and energies, all of which is performed with full mutual polarization.

This chapter is organized as follows. First, we overview the mathematical formalism of PB-SAM in the theory section, then we describe the software and its integration into the APBS package. In the electrostatic potential section we describe different visualization tools available in PB-SAM and in the next section we briefly describe the dynamic tools.

PB-SAM Theory

The derivation details of PB-SAM have been reported previously [2, 3], but the main points can be summarized as follows. The electrostatic potential of the system at any point $\mathbf{t}$ is governed by the linearized form of the Poisson-Boltzmann equation

$$\nabla \cdot [\epsilon(\mathbf{t})\nabla\Phi(\mathbf{t})] - \epsilon(\mathbf{t})\kappa^2\Phi(\mathbf{t}) = 4\pi\rho(\mathbf{t}) \tag{6.1}$$

For the case of spherical cavities, we can solve Equation 6.1 by dividing the system into inner sphere and outer sphere regions, and enforcing a set of boundary conditions that stipulate the continuity of the electrostatic potential and the electrostatic field at the surface of each sphere. The electrostatic potential outside the molecules is described by:

$$\Phi_{out}^{(i)}(\mathbf{t}) = \sum_{I=1}^{N_{mol}} \left(4\pi \int_{d\Omega^{(I)}} \frac{e^{-\kappa|r-r'|}}{|r-r'|} h^{(I)}(r')dr' \right) \tag{6.2}$$

where $h(r)$ is an effective surface charge that can be transformed into the unknown multipole expansion $H^{(I,k)}$ inside molecule I, sphere k. In a similar manner, the interior potential is given as

$$\Phi_{in}^{(i)}(\mathbf{t}) = \sum_{\alpha=1}^{N_C^{(I)}} \frac{1}{|r-r_\alpha^{(I)}|} \frac{q_\alpha^{(I)}}{\epsilon_{in}} + \frac{1}{4\pi} \int_{d\Omega^{(I)}} \frac{1}{|r-r'|} f^{(I)}(r')dr' \tag{6.3}$$

where $N_C^{(I)}$ is the number of charges in molecule I, q_α is the magnitude of the α-th charge, and $p_\alpha^{(I)} = [\rho_\alpha^{(I)}, \nu_\alpha^{(I)}, \phi_\alpha^{(I)}]$ is its position in spherical coordinates. $f(r)$ is a reactive surface charge that can be transformed into the unknown multipole expansion $F^{(I,k)}$. $F^{(I,k)}$ and $H^{(I,k)}$ are given as:

$$F_{n,m}^{(I,k)} \equiv \frac{1}{4\pi} \int_{d\Omega^{(I,k)}} f^{(I,k)}(r') \left(\frac{a^{(I,k)}}{r'} \right)^{n+1} \overline{Y_{n,m}^{(I,k)}}(\theta', \phi') dr' \tag{6.4}$$

$$H_{n,m}^{(I,k)} \equiv \frac{1}{4\pi} \int_{d\Omega^{(I,k)}} h^{(I,k)}(r') \left(\frac{r'}{a^{(I,k)}} \right)^{n} \hat{i}_n(\kappa r') \overline{Y_{n,m}^{(I,k)}}(\theta', \phi') dr' \tag{6.5}$$

$Y_{n,m}$ are the spherical harmonics and $a^{(I,k)}$ is the radius of sphere k of molecule I. These multipole expansions can be iteratively solved using:

$$F_{n,m}^{(I,k)} = \langle I_{E,n,m}^{(I,k)}, WF^{(I,k)} \rangle \tag{6.6}$$

$$H_{n,m}^{(I,k)} = \langle I_{E,n,m}^{(I,k)}, WH^{(I,k)} \rangle \tag{6.7}$$

Where $\langle\,\rangle$ denotes an inner product, and $WF^{(I,k)}, WH^{(I,k)}$ are scaled multipoles computed from fixed charges and polarization charges from other spheres (see [2, 3] for more details). $I_{E,n,m}^{(I,k)}$ is a matrix of the surface integrals over the exposed surface:

$$I_{E,n,m}^{(I,k)} \equiv \frac{1}{4\pi} \int_{\phi_E} \int_{\theta_E} d\theta' d\phi' \; Y_{l,s}^{(I,k)}(\theta', \phi') \overline{Y_{n,m}^{(I,k)}}(\theta', \phi') sin\theta' \tag{6.8}$$

Using this formalism, physical properties of the system, such as interaction energy, forces and torques may be computed. The interaction energy of each molecule, $\Omega^{(i)}$, is the product of the molecules total charge distribution (from fixed and polarization charges) with the potential due to external sources. This is computed as the inner product between the molecules multipole expansion, $H^{(I,k)}$, and the multipole expansions of the other molecules in the system, $LHN^{(I,k)}$ as follows:

$$\Omega^{(i)} = \frac{1}{\epsilon_s} \sum_{k}^{N_k^{(I)}} \langle LHN^{(I,k)}, H^{(I,k)} \rangle \tag{6.9}$$

which allows us to define the force which is computed as the gradient of the interaction energy with respect to the position of the center of molecule I:

$$F^{(I)} = -\nabla\Omega^{(I)} = -\frac{1}{\epsilon_s} \sum_{k}^{N_k^{(I)}} (\langle \nabla LHN^{(I,k)}, H^{(I,k)} \rangle + \langle LHN^{(I,k)}, \nabla H^{(I,k)} \rangle) \tag{6.10}$$

By definition, the torque on a charge in the molecule is the cross product of its position relative to the center of mass of the molecule with the force it experiences. The total torque

on the molecule is a linear combination of the torque on all charges of the molecule.

$$\tau^{(I)} = \frac{1}{\epsilon_s} \sum_{k}^{N_k^{(I)}} \left[H^{(I,k),x}, H^{(I,k),y}, H^{(I,k),z} \right] \times \left[\nabla_{I,k} LHN^{(I,k)} \right] \tag{6.11}$$

Please see previous publications [2, 3] for details on the PB-SAM solver.

Software Architecture

The stand-alone PB-SAM code has been completely re-written from the original code base development [2] in C++11 to include a modular interface, simplified input files, expanded examples, unit testing, and an automated build system (CMake). Most of its outputs are identical to the new release of PB-AM [132], and are compatible with the Python utilities included in the software package. The new Application Programming Interface (API) has been designed to focus on three important utilities of the program: 1) electrostatic potential visualization, 2) energy, force, and torque calculation for molecule-molecule interactions, 3) dynamical simulations using Brownian dynamics. The input file structure is simple; each line containing a keyword value pair, in most cases, and for most basic usage, the program can be run with an input file of 3 lines. Additionally, the outputs have been expanded to formats readable in VMD [81], such as dx and xyz files. Finally, an extensive user manual and website (https://davas301.github.io/pb_solvers/) have been developed with examples and post-processing examples. PB-SAM is available for download through the GitHub site: https://github.com/davas301/pb_solvers. Figure 6.1 shows the workflow of the software and its components.

In addition to the stand-alone code, the PB-AM code has been integrated into the Adaptive Poisson-Boltzmann Solver (APBS) software package that solves the equations of continuum electrostatics for large biomolecular assemblages. PB-SAM has been fully integrated into the APBS software. The user invokes the code with a keyword in the ELEC section of an APBS input file. Some additional keywords are required and are documented on the APBS website. The incorporation of PB-AM into APBS will allow for PB-AM to be available to an audience of thousands of users, and is made available through the APBS site: http://www.poissonboltzmann.org/.

Electrostatic Potential Visualization

One of the most popular uses of PBE solvers is to provide rapid analysis of the electrostatic potentials around macromolecules and their assemblies. Therefore, like many other PBE solvers, our PB-SAM approach has the capability of producing output files for visualizing the electrostatic potential (ESP) of a system of arbitrary complexity. To this end we have provided several visualization options that a user may select, including two-dimensional ESP

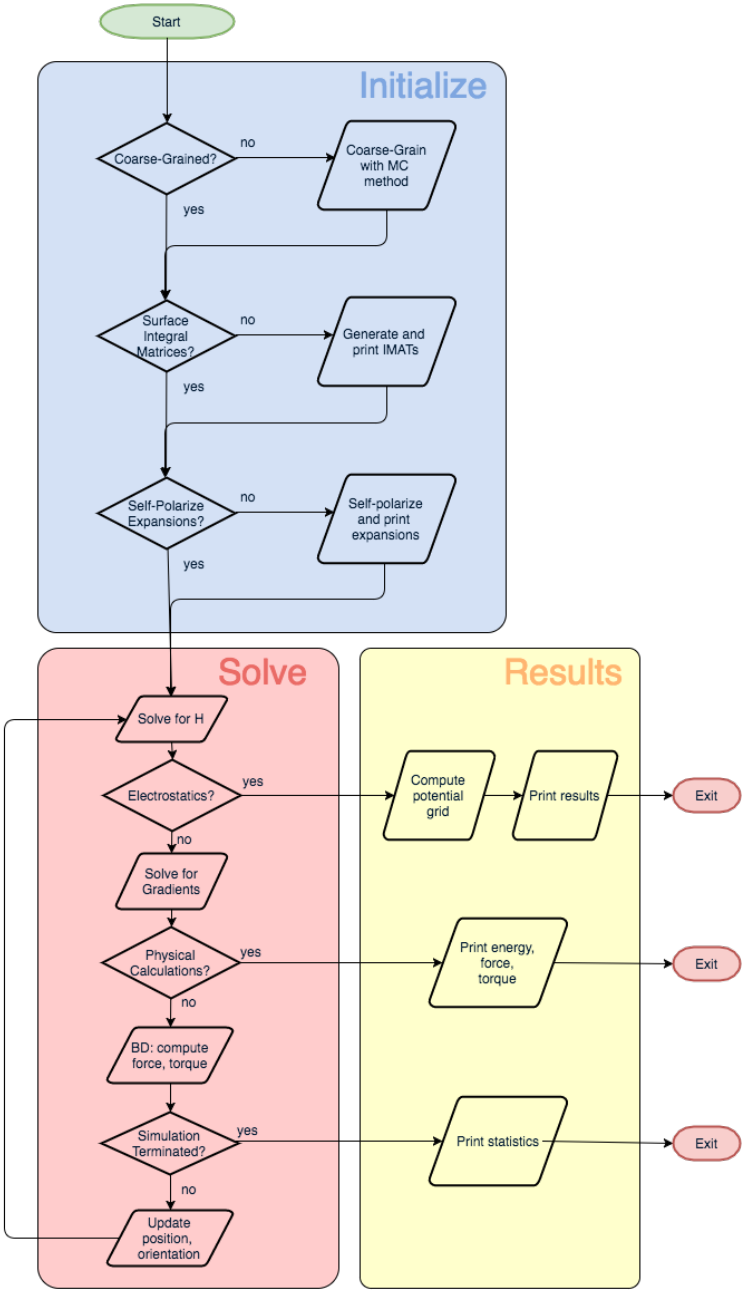

Figure 6.1: *Software workflow for the PB-SAM model and its utilities.* The stand alone PB-SAM code has been completely re-written from the original development [2] in C++11, and has three important utilities: electrostatic potential visualization, energy, force, and torque calculations for molecule-molecule interactions and mutual polarization models, dynamical simulations using Brownian dynamics, which can generate many interesting outputs, for example, different ways to calculate rate constants for biomolecule association.

cross-sections and isosurface potentials (Figure 6.2), which may be loaded and viewed in the program Visual Molecular Dynamics [81] (VMD). In addition to the electrostatic potentials it is also quite straightforward to visualize of forces and torques on and around the center-of-mass.

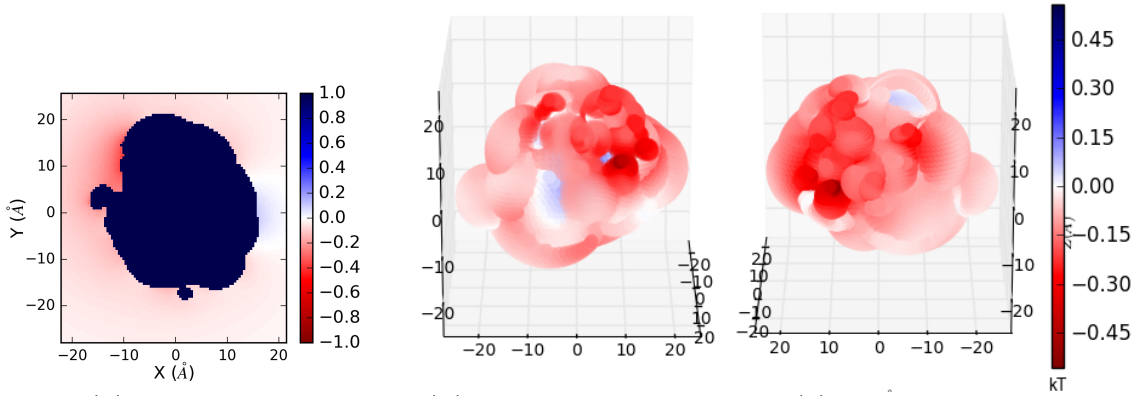

(a) Barstar 2D **(b)** Barstar 3D view 1 **(c)** Barstar 3D view 2

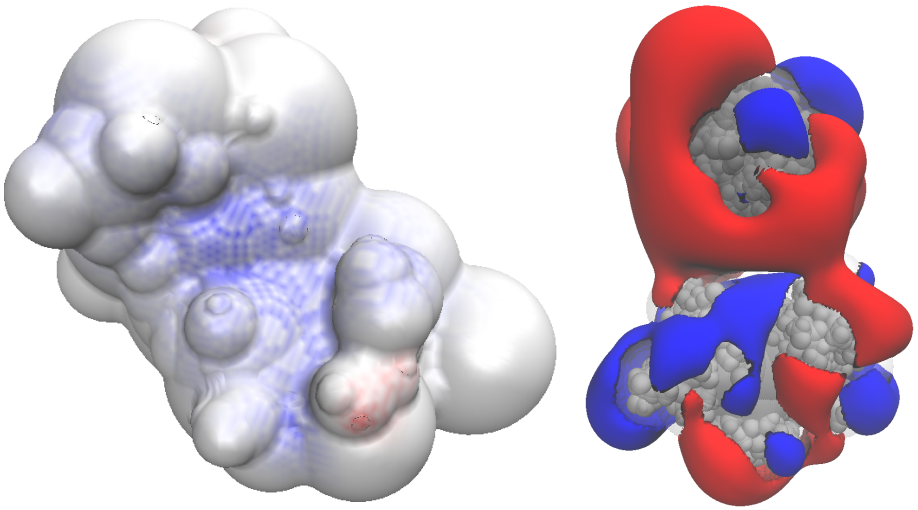

(d) Barnase **(e)** Barnase/barstar

Figure 6.2: *Different visualizations of the electrostatic potentials from the PB-SAM model.* All systems are 0.0M salt, 7 pH, dielectric 2 (protein), and 78 (solution). (a) Two-dimensional cross section of an isolated barstar molecule. (b,c) Three-dimensional surface potential from two different vantage points of the coarse-grained Barstar protein. The color scale for (a-c) is given by color bar on the right, in units of k_BT/e. (d) Surface potential of barnase molecule at barstar association face. (e) Isosurface around a barnase and barstar molecule association. Isosurfaces are drawn at 1.0 (blue) and -1.0 (red) k_BT/e.

Dynamical Trajectories and Analysis Tools

In addition to electrostatics calculations, the PB-SAM software includes dynamics capabilities. The computed expressions for force and torque have been incorporated into a Brownian dynamics simulation protocol adapted from Ermak and McCammon [163]. Each molecule in the system is treated as an independent rigid particle, and molecule-molecule overlap is not allowed. Assuming no hydrodynamic effects, the translational and rotational displacement, Δr_i and $\Delta\theta_i$ respectively, are computed as:

$$\Delta r_i = \frac{D_{trans}\Delta t}{k_B T} f_i + S_i(\Delta t) \tag{6.12}$$

$$\Delta\theta_i = \frac{D_{rot}\Delta t}{k_B T} \tau_i + \Theta_i(\Delta t) \tag{6.13}$$

Where S_i is the stochastic displacement, and Θ_i is the stochastic rotation, have the following properties in dimension $\alpha = x, y, z$:

$$\Delta r_i = \frac{D_{trans}\Delta t}{k_B T} f_i + S_i(\Delta t) \tag{6.14}$$

$$\Delta\theta_i = \frac{D_{rot}\Delta t}{k_B T} \tau_i + \Theta_i(\Delta t) \tag{6.15}$$

The PB-SAM software allows a generalized simulation procedure for a variety of terminations conditions, including a) time: the simulation will terminate when it has run for t picoseconds, b) coordinates: the simulation will terminate when a specified particle has diffused beyond a certain point in space specified by the user, c) docking: the simulation will terminate when a pair of specified atoms in the simulated molecules are within a specified cutoff; this docking criteria is specified by the user as a contact list at the start of the simulation. For details on BD simulation in PB-SAM, please see our user manual. Results from simulations of the association of barnase, a ribonuclease and barstar its intracellular inhibitor, have been published previously [3].

Conclusions

PB-SAM has been presented as a updated version of the model introduced by Yap and Head-Gordon in 2010 [2] and 2013 [3]. It is an extension of the PB-AM method [1, 132], wherein a macromolecule is represented as a single coarse-grain sphere. The semi-analytical method utilizes boundary element methods to extend the PB-AM representation of a molecule to a collection of overlapping spheres. This allows a user to recapture the description of the molecular surface while maintaining components of the analytical formalism.

Like PB-AM, the method has been rewritten in C++11 and has been build with user-friendly features, including an installation using the software CMake, as well as a new API

with a simple input file for easy program usage. Additionally, the outputs can be one of three calculations: 1. Electrostatic potential calculations for visualization, 2. Energy, force and torque calculations and 3. Brownian dynamics simulations with a variety of simulation options to enable the simulation of a wide range of systems. Additionally, the code has also been integrated into APBS, a distributed software widely used in the PBE community. This will provide access of PB-SAM to a broader scientific community.

Future improvements to the model may include additional simulation features, such as the inclusion of hydrodynamic forces, and further development of the software to improve performance, such as the extension of the software to MPI or GPU code.

Chapter 7

Conclusions

Computational methods provide a depth of insight into physical systems that can be used to complement, and interpret experimental results. Through this work, I have made important progress on two different areas of computational chemistry and engineering applications: the application of atomistic molecular dynamics simulations to study water in nanoscale confinement between graphene sheets and star di-block copolymers for drug delivery applications, and the development and implementation of an efficient method to solve the electrostatic potential in continuum-solvent calculations using the LPBE.

Due to the ubiquity of water in confinement in a variety of non-biological and biological systems, work elucidating the structure and properties of this form of water is crucial. Chapter 2 explores the out-of-plane and in-plane structure of water between two graphene sheets. By varying the 2D density of the water within the graphene sheets and the rigidity of the graphene walls, I observed a variety of different water phases in confinement, including liquid/vapor mixtures, ice/vapor mixtures and liquid states. The monolayer water formed square ice at high packing densities and the rigid systems had hexagonal AA stacked bilayer ice. The crucial difference between the flexible and rigid phases was that at densities that fell between well defined n and (n+1) interlayers, a coexistence was formed in the flexible systems between n and (n+1) layers, e.g. monolayer and bilayer coexistence.

For the desired application of drug and biomaterial delivery, it is crucial to have a complete understanding of these polymer systems and it is desirable to control the loading and release of material for fine-tuned applications. In chapter 3, I analyzed the effect that polymer chain length and hydrophilic group chemistry has on star polymer properties. I found that the shorter polymer chains did not reproduce longer chain properties, and are therefore not an accurate representation of experimental systems. Additionally, it was found that by increasing the hydrophilic sidechain length and complexity, the block polymer was less solvated and tended towards higher self-association. Furthermore, the only star polymer that showed indications of thermosensitivity was the poly-ethylene glycol (PEG) system, which displayed decreasing PEG-bulk water interactions, decreasing PEG-water hydrogen bonds and a depopulation of the trans-gauche-trans backbone dihedral conformer as a function of increasing temperature.

In chapter 4, small-angle X-ray scattering was used to access the pH-sensitivity of non-degradable nanogel star polymers with basic, acidic and neutral sidechain groups on the hydrophilic monomers. It was found that the acidic and basic polymers undergo a structural transition as a function of pH, but with large shifts in the apparent pKa with respect to that of the monomer unit. The transition was also modulated by the percentage composition of the hydrophilic region.

In the last two chapters, the development of theory and algorithms for modeling coarse-grain systems was addressed. Long-range interactions such as electrostatics Certain microscopic phenomena, such as molecular association occur over spatial and temporal scales inaccessible by all-atom molecular dynamics. In many cases, these long-time scale phenomena are electrostatically driven and insensitive to the atomistic details of the solvent. For this reason coarse graining and stochastic dynamics are used to study these interactions and can be just as insightful as all-atom deterministic dynamics. The linearized Poisson-Boltzmann equation (LPBE) describes the electrostatic potential of a continuum system as an approximation to the nonlinear PBE, and is used to model the electrostatic potential of many biological systems. Building on work previously developed in the Head-Gordon group [1–3], analytical and semi-analytical solutions to the LPBE Ire combined with Brownian dynamics to create software packages suitable for biomolecular simulations. Chapter 5 introduces the full implementation of the analytical solution to the LPBE, PB-AM. The fully analytical solution solves for the potential of a system of an arbitrary number of molecules with complex charge distributions in a salty (screened) solution, where each molecule is represented as a single coarse-grain spherical cavity. The code base was rewritten from the 2006 implementation [1] in C++11 and is available open source on GitHub. It features a new application programming interface and an automated installation with the software CMake. Several new outputs and scripts for visualizing the electrostatic potential are available with the software. Additionally, the solution has been integrated into a Brownian dynamics scheme for the simulation of a variety of systems. An extension of the analytical method, the Poisson-Boltzmann semi-analytical method (PB-SAM) is presented in chapter 6. It too was re-implemented from the original formulation [2, 3] in C++11, and implemented for electrostatic potential visualization and Brownian dynamics simulations. Both methods are also integrated into the APBS software package to provide visibility of the method to a larger group of scientists and to encourage collaboration within the community of computational chemists.

Bibliography

[1]I. Lotan and T. Head-Gordon, "An analytical electrostatic model for salt screened interactions between multiple proteins", Journal of Chemical Theory and Computation **2**, 541–555 (2006).

[2]E. H. Yap and T. Head-Gordon, "A new and efficient poisson-boltzmann solver for interaction of multiple proteins", J Chem Theory Comput **6**, 2214–2224 (2010).

[3]E. H. Yap and T. Head-Gordon, "Calculating the bimolecular rate of protein-protein association with interacting crowders", J Chem Theory Comput **9**, 2481–9 (2013).

[4]M. Karplus and J. A. McCammon, "Molecular dynamics simulations of biomolecules", Nat Struct Mol Biol **9**, 646–652 (2002).

[5]S. J. Marrink, A. H. de Vries, and A. E. Mark, "Coarse grained model for semiquantitative lipid simulations", The Journal of Physical Chemistry B **108**, 750–760 (2004).

[6]V. V. Chaban and O. V. Prezhdo, "Water boiling inside carbon nanotubes: toward efficient drug release", ACS Nano **5**, PMID: 21648482, 5647–5655 (2011).

[7]G. F. Schneider, S. W. Kowalczyk, V. E. Calado, G. Pandraud, H. W. Zandbergen, L. M. K. Vandersypen, and C. Dekker, "Dna translocation through graphene nanopores", Nano Letters **10**, PMID: 20608744, 3163–3167 (2010).

[8]S. Prakash, A. Piruska, E. N. Gatimu, P. W. Bohn, J. V. Sweedler, and M. A. Shannon, "Nanofluidics: systems and applications", IEEE Sensors Journal **8**, 441–450 (2008).

[9]P. Dhiman, F. Yavari, X. Mi, H. Gullapalli, Y. Shi, P. M. Ajayan, and N. Koratkar, "Harvesting energy from water flow over graphene", Nano Letters **11**, PMID: 21749100, 3123–3127 (2011).

[10]A. Siria, P. Poncharal, A.-L. Biance, R. Fulcrand, X. Blase, S. T. Purcell, and L. Bocquet, "Giant osmotic energy conversion measured in a single transmembrane boron nitride nanotube", Nature **494**, 455–458 (2013).

[11]J. Korb, A. Delville, S. Xu, G. Demeulenaere, P. Costa, and J. Jonas, "Relative role of surface interactions and topological effects in nuclear magnetic resonance of confined liquids", The Journal of Chemical Physics **101**, 7074–7081 (1994).

[12]G. Liu, Y. Li, and J. Jonas, "Confined geometry effects on reorientational dynamics of molecular liquids in porous silica glasses", The Journal of Chemical Physics **95**, 6892–6901 (1991).

[13]D. Laage and W. H. Thompson, "Reorientation dynamics of nanoconfined water: power-law decay, hydrogen-bond jumps, and test of a two-state model", The Journal of Chemical Physics **136**, 044513 (2012).

[14]Y. Maniwa, H. Kataura, M. Abe, A. Udaka, S. Suzuki, Y. Achiba, H. Kira, K. Matsuda, H. Kadowaki, and Y. Okabe, "Ordered water inside carbon nanotubes: formation of pentagonal to octagonal ice-nanotubes", Chemical Physics Letters **401**, 534 –538 (2005).

[15]G Algara-Siller, O Lehtinen, F. C. Wang, R. R. Nair, U Kaiser, H. A. Wu, A. K. Geim, and I. V. Grigorieva, "Square ice in graphene nanocapillaries", Nature **519**, 443–445 (2015).

[16]R. Zangi and A. E. Mark, "Monolayer ice", Phys. Rev. Lett. **91**, 025502 (2003).

[17]R. Zangi and A. E. Mark, "Bilayer ice and alternate liquid phases of confined water", The Journal of Chemical Physics **119**, 1694–1700 (2003).

[18]E. A. Appel, V. Y. Lee, T. T. Nguyen, M. McNeil, F. Nederberg, J. L. Hedrick, W. C. Swope, J. E. Rice, R. D. Miller, and J. Sly, "Toward biodegradable nanogel star polymers via organocatalytic rop", Chem Commun (Camb) **48**, 6163–5 (2012).

[19]V. Y. Lee, K. Havenstrite, M. Tjio, M. McNeil, H. M. Blau, R. D. Miller, and J. Sly, "Nanogel star polymer architectures: a nanoparticle platform for modular programmable macromolecular self-assembly, intercellular transport, and dual-mode cargo delivery", Adv Mater **23**, 4509–15 (2011).

[20]A. Heise, J. L. Hedrick, C. W. Frank, and R. D. Miller, "Starlike block copolymers with amphiphilic arms as models for unimolecular micelles", Journal of the American Chemical Society **121**, 8647–8648 (1999).

[21]L. Cosimbescu, J. W. Robinson, Y. Zhou, and J. Qu, "Dual functional star polymers for lubricants", RSC Adv. **6**, 86259–86268 (2016).

[22]P. Chytil, E. Koziolov, O. Janoukov, L. Kostka, K. Ulbrich, and T. Etrych, "Synthesis and properties of star hpma copolymer nanocarriers synthesised by raft polymerisation designed for selective anticancer drug delivery and imaging", Macromolecular Bioscience **15**, 839–850 (2015).

[23]Y. Q. Yang, B. Zhao, Z. D. Li, W. J. Lin, C. Y. Zhang, X. D. Guo, J. F. Wang, and L. J. Zhang, "Ph-sensitive micelles self-assembled from multi-arm star triblock co-polymers poly(-caprolactone)-b-poly(2-(diethylamino)ethyl methacrylate)-b-poly(poly(ethylene glycol) methyl ether methacrylate) for controlled anticancer drug delivery", Acta Biomaterialia **9**, 7679 –7690 (2013).

[24]F. A. Plamper, M. Ruppel, A. Schmalz, O. Borisov, M. Ballauff, and A. H. E. Muller, "Tuning the thermoresponsive properties of weak polyelectrolytes: aqueous solutions of star-shaped and linear poly(n,n-dimethylaminoethyl methacrylate)", Macromolecules **40**, 8361–8366 (2007).

[25]J. K. Holt, H. G. Park, Y. Wang, M. Stadermann, A. B. Artyukhin, C. P. Grigoropoulos, A. Noy, and O. Bakajin, "Fast mass transport through sub-2-nanometer carbon nanotubes", Science **312**, 1034–1037 (2006).

[26]D. Lucent, V. Vishal, and V. S. Pande, "Protein folding under confinement: a role for solvent", Proceedings of the National Academy of Sciences of the United States of America **104**, 10430–10434 (2007).

[27]N. E. Levinger, "Water in confinement", Science **298**, 1722–1723 (2002).

[28]R. R. Nair, H. A. Wu, P. N. Jayaram, I. V. Grigorieva, and A. K. Geim, "Unimpeded permeation of water through helium-leak-tight graphene-based membranes", Science **335**, 442–444 (2012).

[29]K. Koga, G. T. Gao, H. Tanaka, and X. C. Zeng, "Formation of ordered ice nanotubes inside carbon nanotubes", Nature **412**, 802–805 (2001).

[30]W. Zhou, K. Yin, C. Wang, Y. Zhang, T. Xu, A. Borisevich, L. Sun, J. C. Idrobo, M. F. Chisholm, S. T. Pantelides, R. F. Klie, and A. R. Lupini, "The observation of square ice in graphene questioned", Nature **528**, E1–E2 (2015).

[31]N. Giovambattista, P. J. Rossky, and P. G. Debenedetti, "Phase transitions induced by nanoconfinement in liquid water", Physical Review Letters **102**, 050603 (2009).

[32]S. Han, M. Y. Choi, P. Kumar, and H. E. Stanley, "Phase transitions in confined water nanofilms", Nat Phys **6**, 685–689 (2010).

[33]K. Mochizuki and K. Koga, "Solidliquid critical behavior of water in nanopores", Proceedings of the National Academy of Sciences **112**, 8221–8226 (2015).

[34]Y. Zhu, F. Wang, J. Bai, X. C. Zeng, and H. Wu, "Compression limit of two-dimensional water constrained in graphene nanocapillaries", ACS Nano **9**, 12197–12204 (2015).

[35]Y. E. Altabet, A. Haji-Akbari, and P. G. Debenedetti, "Effect of material flexibility on the thermodynamics and kinetics of hydrophobically induced evaporation of water", Proceedings of the National Academy of Sciences **114**, E2548–E2555 (2017).

[36]T. Head-Gordon and R. M. Lynden-Bell, "Hydrophobic solvation of gay-berne particles in modified water models", The Journal of Chemical Physics **128**, 104506 (2008).

[37]G. Hummer, J. C. Rasaiah, and J. P. Noworyta, "Water conduction through the hydrophobic channel of a carbon nanotube", Nature **414**, 188–190 (2001).

[38]S. Sharma and P. G. Debenedetti, "Evaporation rate of water in hydrophobic confinement", Proceedings of the National Academy of Sciences **109**, 4365–4370 (2012).

[39]D. Chandler, "Hydrophobicity: two faces of water", Nature **417**, 491–491 (2002).

[40]Y. Wei, B. Wang, J. Wu, R. Yang, and M. L. Dunn, "Bending rigidity and gaussian bending stiffness of single-layered graphene", Nano Letters **13**, 26–30 (2013).

[41]A Fasolino, J. H. Los, and M. I. Katsnelson, "Intrinsic ripples in graphene", Nat Mater **6**, 858–861 (2007).

[42]A. K. Geim and K. S. Novoselov, "The rise of graphene", Nat Mater **6**, 183–191 (2007).

[43]A. A. Chialvo and L. Vlcek, "Can we describe graphene confined water structures as overlapping of approaching graphene-water interfacial structures?", The Journal of Physical Chemistry C **120**, 7553–7561 (2016).

[44]G. Cicero, J. C. Grossman, E. Schwegler, F. Gygi, and G. Galli, "Water confined in nanotubes and between graphene sheets: a first principle study", Journal of the American Chemical Society **130**, 1871–1878 (2008).

[45]J. Chen, G. Schusteritsch, C. J. Pickard, C. G. Salzmann, and A. Michaelides, "Double-layer ice from first principles", Physical Review B **95**, 094121 (2017).

[46]F. Corsetti, P. Matthews, and E. Artacho, "Structural and configurational properties of nanoconfined monolayer ice from first principles", Scientific Reports **6**, 18651 (2016).

[47]V. Satarifard, M. Mousaei, F. Hadadi, J. Dix, M. Sobrino Fernandez, P. Carbone, J. Beheshtian, F. M. Peeters, and M. Neek-Amal, "Reversible structural transition in nanoconfined ice", Physical Review B **95**, 064105 (2017).

[48]H. Qiu, X. C. Zeng, and W. Guo, "Water in inhomogeneous nanoconfinement: coexistence of multilayered liquid and transition to ice nanoribbons", ACS Nano **9**, PMID: 26348704, 9877–9884 (2015).

[49]M. Neek-Amal, F. M. Peeters, I. V. Grigorieva, and A. K. Geim, "Commensurability effects in viscosity of nanoconfined water", ACS Nano **10**, 3685–3692 (2016).

[50]S. A. Deshmukh, G. Kamath, and S. K. R. S. Sankaranarayanan, "Comparison of the interfacial dynamics of water sandwiched between static and free-standing fully flexible graphene sheets", Soft Matter **10**, 4067–4083 (2014).

[51]M. Hamid, A. Saman, M. H. Kowsari, and N. Bijan, "Simulations of structural and dynamic anisotropy in nano-confined water between parallel graphite plates", The Journal of Chemical Physics **137**, 184703 (2012).

[52]F. H. Stillinger and T. Head-Gordon, "Perturbational view of inherent structures in water", Phys Rev E Stat Phys Plasmas Fluids Relat Interdiscip Topics **47**, 2484–2490 (1993).

[53]H. W. Horn, W. C. Swope, J. W. Pitera, J. D. Madura, T. J. Dick, G. L. Hura, and T. Head-Gordon, "Development of an improved four-site water model for biomolecular simulations: tip4p-ew", J Chem Phys **120**, 9665–78 (2004).

[54]N. Patra, B. Wang, and P. Kral, "Nanodroplet activated and guided folding of graphene nanostructures", Nano Letters **9**, PMID: 19852466, 3766–3771 (2009).

[55]S. Plimpton, "Fast parallel algorithms for short-range molecular-dynamics", Journal of Computational Physics **117**, 1–19 (1995).

[56]H. C. Andersen, "Rattle - a velocity version of the shake algorithm for molecular-dynamics calculations", Journal of Computational Physics **52**, 24–34 (1983).

[57]T. Schneider and E. Stoll, "Molecular-dynamics study of a three-dimensional one-component model for distortive phase transitions", Phys. Rev. B **17**, 1302–1322 (1978).

[58]G. J. Martyna, D. J. Tobias, and M. L. Klein, "Constant-pressure molecular-dynamics algorithms", Journal of Chemical Physics **101**, 4177–4189 (1994).

[59]L. E. Felberg, D. H. Brookes, T. Head-Gordon, J. E. Rice, and W. C. Swope, "Role of hydrophilicity and length of diblock arms for determining star polymer physical properties", J Phys Chem B **119**, 944–57 (2015).

[60]O. Sedlacek, B. D. Monnery, S. K. Filippov, R. Hoogenboom, and M. Hruby, "Poly(2-oxazoline)s–are they more advantageous for biomedical applications than other polymers?", Macromol Rapid Commun **33**, 1648–62 (2012).

[61]W. C. Swope, A. C. Carr, A. J. Parker, J. Sly, R. D. Miller, and J. E. Rice, "Molecular dynamics simulations of star polymeric molecules with diblock arms, a comparative study", Journal of Chemical Theory and Computation **8**, 3733–3749 (2012).

[62]S. Saeki, N. Kuwahara, M. Nakata, and M. Kaneko, "Upper and lower critical solution temperatures in poly (ethylene glycol) solutions", Polymer **17**, 685–689 (1976).

[63]W. L. Jorgensen, D. S. Maxwell, and J. TiradoRives, "Development and testing of the opls all-atom force field on conformational energetics and properties of organic liquids", Journal of the American Chemical Society **118**, 11225–11236 (1996).

[64]M. L. P. Price, D. Ostrovsky, and W. L. Jorgensen, "Gas-phase and liquid-state properties of esters, nitriles, and nitro compounds with the opls-aa force field", Journal of Computational Chemistry **22**, 1340–1352 (2001).

[65]G. Kaminski, E. M. Duffy, T. Matsui, and W. L. Jorgensen, "Free-energies of hydration and pure liquid properties of hydrocarbons from the opls all-atom model", Journal of Physical Chemistry **98**, 13077–13082 (1994).

[66]W. Damm, A. Frontera, J. Tirado Rives, and W. L. Jorgensen, "Opls allatom force field for carbohydrates", Journal of Computational Chemistry **18**, 1955–1970 (1997).

[67]D. J. Price, J. D. Roberts, and W. L. Jorgensen, "Conformational complexity of succinic acid and its monoanion in the gas phase and in solution: ab initio calculations and monte carlo simulations", Journal of the American Chemical Society **120**, 9672–9679 (1998).

[68]W. L. Jorgensen and N. A. McDonald, "Development of an all-atom force field for heterocycles. properties of liquid pyridine and diazenes", Theochem-Journal of Molecular Structure **424**, 145–155 (1998).

[69]N. A. McDonald and W. L. Jorgensen, "Development of an all-atom force field for heterocycles. properties of liquid pyrrole, furan, diazoles, and oxazoles", Journal of Physical Chemistry B **102**, 8049–8059 (1998).

[70]R. C. Rizzo and W. L. Jorgensen, "Opls all-atom model for amines: resolution of the amine hydration problem", Journal of the American Chemical Society **121**, 4827–4836 (1999).

[71]E. K. Watkins and W. L. Jorgensen, "Perfluoroalkanes: conformational analysis and liquid-state properties from ab initio and monte carlo calculations", Journal of Physical Chemistry A **105**, 4118–4125 (2001).

[72]J. C. Soetens, C. Millot, B. Maigret, and I. Bako, "Molecular dynamics simulation and x-ray diffraction studies of ethylene carbonate, propylene carbonate and dimethyl carbonate in liquid phase", Journal of Molecular Liquids **92**, 201–216 (2001).

[73]L. Gontrani, O. Russina, F. C. Marincola, and R. Caminiti, "An energy dispersive x-ray scattering and molecular dynamics study of liquid dimethyl carbonate", J Chem Phys **131**, 244503 (2009).

[74]W. C. Swope, H. C. Andersen, P. H. Berens, and K. R. Wilson, "A computer-simulation method for the calculation of equilibrium-constants for the formation of physical clusters of molecules - application to small water clusters", Journal of Chemical Physics **76**, 637–649 (1982).

[75]R. W. Hockney and J. W. Eastwood, *Computer simulation using particles* (Taylor and Francis, New York, 1989).

[76]L. Huynh, C. Neale, R. Pomes, and C. Allen, "Computational approaches to the rational design of nanoemulsions, polymeric micelles, and dendrimers for drug delivery", Nanomedicine **8**, 20–36 (2012).

[77]D. N. Theodorou and U. W. Suter, "Shape of unperturbed linear-polymers - polypropylene", Macromolecules **18**, 1206–1214 (1985).

[78]W. Brostow, J. P. Dussault, and B. L. Fox, "Construction of voronoi polyhedra", Journal of Computational Physics **29**, 81–92 (1978).

[79]J. L. Finney, "Procedure for the construction of voronoi polyhedra", Journal of Computational Physics **32**, 137–143 (1979).

[80]A. Grosberg and A. R. Khoklov, *Statistical physics of macromolecules* (AIP Press, New York, 1994).

[81]W. Humphrey, A. Dalke, and K. Schulten, "Vmd: visual molecular dynamics", J Mol Graph **14**, 33–8, 27–8 (1996).

[82]P. J. Flory, "Thermodynamics of heterogeneous polymer solutions", Journal of Chemical Physics **12**, 114–115 (1944).

[83]K. Knop, R. Hoogenboom, D. Fischer, and U. S. Schubert, "Poly(ethylene glycol) in drug delivery: pros and cons as well as potential alternatives", Angew Chem Int Ed Engl **49**, 6288–308 (2010).

[84]E. Markovsky, H. Baabur-Cohen, A. Eldar-Boock, L. Omer, G. Tiram, S. Ferber, P. Ofek, D. Polyak, A. Scomparin, and R. Satchi-Fainaro, "Administration, distribution, metabolism and elimination of polymer therapeutics", J Control Release **161**, 446–60 (2012).

[85]M. Barz, R. Luxenhofer, R. Zentel, and M. J. Vicent, "Overcoming the peg-addiction: well-defined alternatives to peg, from structureproperty relationships to better defined therapeutics", Polymer Chemistry **2**, 1900–1918 (2011).

[86]C. Diehl and H. Schlaad, "Thermo-responsive polyoxazolines with widely tuneable lcst", Macromol Biosci **9**, 157–61 (2009).

[87]R. Hoogenboom, "Poly(2-oxazoline)s: a polymer class with numerous potential applications", Angewandte Chemie International Edition **48**, 7978–7994 (2009).

[88]R. G. Chapman, E. Ostuni, S. Takayama, R. E. Holmlin, L. Yan, and G. M. Whitesides, "Surveying for surfaces that resist the adsorption of proteins", Journal of the American Chemical Society **122**, 8303–8304 (2000).

[89]H. Lee and R. G. Larson, "Molecular dynamics study of the structure and interparticle interactions of polyethylene glycol-conjugated pamam dendrimers", J Phys Chem B **113**, 13202–7 (2009).

[90]H. Lee and R. G. Larson, "Effects of pegylation on the size and internal structure of dendrimers: self-penetration of long peg chains into the dendrimer core", Macromolecules **44**, 2291–2298 (2011).

[91]L. E. Felberg, A. Doshi, G. L. Hura, J. Sly, V. A. Piunova, W. C. Swope, J. E. Rice, R. Miller, and T. Head-Gordon, "Structural transition of nanogel star polymers with ph by controlling pegma interactions with acid or base copolymers", Molecular Physics **0**, 1–11 (0).

[92]T. Wang, G. G. D'Souza, D. Bedi, O. A. Fagbohun, L. P. Potturi, B. Papahadjopoulos-Sternberg, V. A. Petrenko, and V. P. Torchilin, "Enhanced binding and killing of target tumor cells by drug-loaded liposomes modified with tumor-specific phage fusion coat protein", Nanomedicine (Lond) **5**, 563–74 (2010).

[93]C. Kojima, C. Regino, Y. Umeda, H. Kobayashi, and K. Kono, "Influence of dendrimer generation and polyethylene glycol length on the biodistribution of pegylated dendrimers", Int J Pharm **383**, 293–6 (2010).

[94]R. Gref, Y. Minamitake, M. T. Peracchia, V. Trubetskoy, V. Torchilin, and R. Langer, "Biodegradable long-circulating polymeric nanospheres", Science **263**, 1600–3 (1994).

[95]S. A. Bencherif, H. Gao, A. Srinivasan, D. J. Siegwart, J. O. Hollinger, N. R. Washburn, and K. Matyjaszewski, "Cell-adhesive star polymers prepared by atrp", Biomacromolecules **10**, 1795–803 (2009).

[96]K. Fukukawa, R. Rossin, A. Hagooly, E. D. Pressly, J. N. Hunt, B. W. Messmore, K. L. Wooley, M. J. Welch, and C. J. Hawker, "Synthesis and characterization of core-shell star copolymers for in vivo pet imaging applications", Biomacromolecules **9**, 1329–39 (2008).

[97]T. K. Georgiou, M. Vamvakaki, L. A. Phylactou, and C. S. Patrickios, "Synthesis, characterization, and evaluation as transfection reagents of double-hydrophilic star copolymers: effect of star architecture", Biomacromolecules **6**, 2990–2997 (2005).

[98]D. Schmaljohann, "Thermo- and ph-responsive polymers in drug delivery", Adv Drug Deliv Rev **58**, 1655–70 (2006).

[99]H. Almeida, M. H. Amaral, and P. Lobao, "Temperature and ph stimuli-responsive polymers and their applications in controlled and selfregulated drug delivery", Journal of Applied Pharmaceutical Science **06**, 1–10 (2012).

[100]G. Pasut and F. M. Veronese, "Peg conjugates in clinical development or use as anticancer agents: an overview", Advanced Drug Delivery Reviews **61**, 1177–1188 (2009).

[101]M. Longmire, P. L. Choyke, and H. Kobayashi, "Clearance properties of nano-sized particles and molecules as imaging agents: considerations and caveats", Nanomedicine **3**, 703–717 (2008).

[102]J. M. Harris and R. B. Chess, "Effect of pegylation on pharmaceuticals", Nat Rev Drug Discov **2**, 214–21 (2003).

[103]E. Fleige, M. A. Quadir, and R. Haag, "Stimuli-responsive polymeric nanocarriers for the controlled transport of active compounds: concepts and applications", Adv Drug Deliv Rev **64**, 866–84 (2012).

[104]A. Blencowe, J. F. Tan, T. K. Goh, and G. G. Qiao, "Core cross-linked star polymers via controlled radical polymerisation", Polymer **50**, 5–32 (2009).

[105]J.-G. Zilliox, P. Rempp, and J. Parrod, "Prparation de macromolcules structure en etoile, par copolymerisation anionique", Journal of Polymer Science Part C: Polymer Symposia **22**, 145–156 (1968).

[106]J. M. Ren, Q. Fu, A. Blencowe, and G. G. Qiao, "Organic catalyst-mediated ring-opening polymerization for the highly efficient synthesis of polyester-based star polymers", Acs Macro Letters **1**, 681–686 (2012).

[107]N. E. Kamber, W. Jeong, R. M. Waymouth, R. C. Pratt, B. G. Lohmeijer, and J. L. Hedrick, "Organocatalytic ring-opening polymerization", Chem Rev **107**, 5813–40 (2007).

[108]G. L. Hura, A. L. Menon, M. Hammel, R. P. Rambo, n. Poole, F. L., S. E. Tsutakawa, J. Jenney, F. E., S. Classen, K. A. Frankel, R. C. Hopkins, S. J. Yang, J. W. Scott, B. D. Dillard, M. W. Adams, and J. A. Tainer, "Robust, high-throughput solution structural analyses by small angle x-ray scattering (saxs)", Nat Methods **6**, 606–12 (2009).

[109]S. Classen, G. L. Hura, J. M. Holton, R. P. Rambo, I. Rodic, P. J. McGuire, K. Dyer, M. Hammel, G. Meigs, K. A. Frankel, and J. A. Tainer, "Implementation and performance of sibyls: a dual endstation small-angle x-ray scattering and macromolecular crystallography beamline at the advanced light source", Journal of Applied Crystallography **46**, 1–13 (2013).

[110]*Sasview for small angle scattering analysis*. 2015.

[111]H. Benoit, "On the effect of branching and polydispersity on the angular distribution of the light scattered by gaussian coils", Journal of Polymer Science **11**, 507–510 (1953).

[112]W. D. Dozier, J. S. Huang, and L. J. Fetters, "Colloidal nature of star polymer dilute and semidilute solutions", Macromolecules **24**, 2810–2814 (1991).

[113]S. R. Kline and E. W. Kaler, "Interactions in colloidal mixtures: partial structure factors in mixtures of colloidal silica and an anionic oil-in-water microemulsion", J Colloid Interface Sci **203**, 392–401 (1998).

[114]S. Ruthstein, A. M. Raitsimring, R. Bitton, V. Frydman, A. Godt, and D. Goldfarb, "Distribution of guest molecules in pluronic micelles studied by double electron electron spin resonance and small angle x-ray scattering", Phys Chem Chem Phys **11**, 148–60 (2009).

[115]B. Hammouda, "Sans from homogeneous polymer mixtures - a unified overview", Advances in Polymer Science **106**, 87–133 (1993).

[116]M. Daoud and J. P. Cotton, "Star shaped polymers - a model for the conformation and its concentration-dependence", Journal De Physique **43**, 531–538 (1982).

[117]P. Debye, "Molecular-weight determination by light scattering", Journal of Physical and Colloid Chemistry **51**, 18–32 (1947).

[118]B. S. Kim, H. F. Gao, A. A. Argun, K. Matyjaszewski, and P. T. Hammond, "All-star polymer multilayers as ph-responsive nanofilms", Macromolecules **42**, 368–375 (2009).

[119]H. Lee, S. H. Son, R. Sharma, and Y. Y. Won, "A discussion of the ph-dependent protonation behaviors of poly(2-(dimethylamino)ethyl methacrylate) (pdmaema) and poly(ethylenimine-ran-2-ethyl-2-oxazoline) (p(ei-r-eoz))", J Phys Chem B **115**, 844–60 (2011).

[120]D. Fournier, R. Hoogenboom, H. M. L. Thijs, R. M. Paulus, and U. S. Schubert, "Tunable ph- and temperature-sensitive copolymer libraries by reversible addition-fragmentation chain transfer copolymerizations of methacrylates", Macromolecules **40**, 915–920 (2007).

[121]K. Abe, M. Koide, and E. Tsuchida, "Selective complexation of macromolecules", Macromolecules **10**, 1259–1264 (1977).

[122]Y. Yokoyama and S. Yusa, "Water-soluble complexes formed from hydrogen bonding interactions between a poly(ethylene glycol)-containing triblock copolymer and poly(methacrylic acid)", Polymer Journal **45**, 985–992 (2013).

[123]S. Holappa, L. Kantonen, F. M. Winnik, and H. Tenhu, "Self-complexation of poly(ethylene oxide)-block-poly(methacrylic acid) studied by fluorescence spectroscopy", Macromolecules **37**, 7008–7018 (2004).

[124]T. Andersson, M. Sumela, L. Khriachtchev, M. Rasanen, V. Aseyev, and H. Tenhu, "Solution properties of an aqueous poly(methacryl oxyethyl trimethylammonium chloride) and its poly(oxyethylene) grafted analog", Journal of Polymer Science Part B-Polymer Physics **46**, 547–557 (2008).

[125]Y. Osada, "Effects of polymers and their chain lengths on the contraction of poly(methacrylic acid) network", Journal of Polymer Science Part C-Polymer Letters **18**, 281–286 (1980).

[126]G. H. Jiang, X. K. Sun, Y. Z. Zhu, and Y. Wang, "Ph- and thermo-sensitive co-polymers based on a hyperbranched polymers core as encapsulation and release carriers for guest molecules", Designed Monomers and Polymers **14**, 167–178 (2011).

[127]L. Ma, R. Liu, J. Tan, D. Wang, X. Jin, H. Kang, M. Wu, and Y. Huang, "Self-assembly and dual-stimuli sensitivities of hydroxypropylcellulose-graft-poly(n,n-dimethyl aminoethyl methacrylate) copolymers in aqueous solution", Langmuir **26**, 8697–703 (2010).

[128]S. H. Yuk, S. H. Cho, and S. H. Lee, "Ph/temperature-responsive polymer composed of poly((n,n-dimethylamino)ethyl methacrylate-co-ethylacrylamide)", Macromolecules **30**, 6856–6859 (1997).

[129]X. Han, X. X. Zhang, H. F. Zhu, Q. Y. Yin, H. L. Liu, and Y. Hu, "Effect of composition of pdmaema-b-paa block copolymers on their ph- and temperature-responsive behaviors", Langmuir **29**, 1024–1034 (2013).

[130]S. H. Cho, M. S. Jhon, and S. H. Yuk, "Temperature-sensitive swelling behavior of polymer gel composed of poly (n,n-dimethylaminoethyl methacrylate) and its copolymers", European Polymer Journal **35**, 1841–1845 (1999).

[131]C. R. Becer, S. Hahn, M. W. M. Fijten, H. M. L. Thijs, R. Hoogenboom, and U. S. Schubert, "Libraries of methacrylic acid and oligo(ethylene glycol) methacrylate copolymers with lcst behavior", Journal of Polymer Science Part a-Polymer Chemistry **46**, 7138–7147 (2008).

[132]L. E. Felberg, D. H. Brookes, E.-H. Yap, E. Jurrus, N. A. Baker, and T. Head-Gordon, "Pb-am: an open-source, fully analytical linear poisson-boltzmann solver", Journal of Computational Chemistry, n/a–n/a.

[133]D. Chapman, "A contribution to the theory of electrocapillarity", Philosophical Magazine Series 6 **25**, 475–481 (1913).

[134]G. Gouy, "The mutual action of two cathodes in a magnetic field", Comptes Rendus Hebdomadaires des Seances de l'Academie des Sciences **150**, 1652–1655 (1910).

[135]B. Derjaguin and L. Landau, "Theory of the stability of strongly charged lyophobic sols and of the adhesion of strongly charged-particles in solutions of electrolytes", Progress in Surface Science **43**, 30–59 (1993).

[136]E. Verwey, "Theory of the stability of lyophobic colloids", Phillips Research Reports **1**, 33–49 (1945).

[137]P. Debye and E. Hueckel, "The theory of electrolytes i. the lowering of the freezing point and related occurences", Physikalische Zeitscrift **24**, 185–206 (1923).

[138]N. A. Baker, D. Sept, S. Joseph, M. J. Holst, and J. A. McCammon, "Electrostatics of nanosystems: application to microtubules and the ribosome", Proc Natl Acad Sci U S A **98**, 10037–41 (2001).

[139]L. Li, C. Li, S. Sarkar, J. Zhang, S. Witham, Z. Zhang, L. Wang, N. Smith, M. Petukh, and E. Alexov, "Delphi: a comprehensive suite for delphi software and associated resources", BMC Biophys **5**, 9 (2012).

[140]D. Bashford, "An object-oriented programming suite for electrostatic effects in biological molecules an experience report on the mead project", in *Scientific computing in object-oriented parallel environments: first international conference, iscope 97 marina del rey, california, usa december 811, 1997 proceedings*, edited by Y. Ishikawa, R. R. Oldehoeft, J. V. W. Reynders, and M. Tholburn (Springer Berlin Heidelberg, Berlin, Heidelberg, 1997), pp. 233–240.

[141]M. E. Davis, J. D. Madura, B. A. Luty, and J. A. Mccammon, "Electrostatics and diffusion of molecules in solution - simulations with the university-of-houston-brownian dynamics program", Computer Physics Communications **62**, 187–197 (1991).

[142]J. A. Grant, B. T. Pickup, and A. Nicholls, "A smooth permittivity function for poisson-boltzmann solvation methods", Journal of Computational Chemistry **22**, 608–640 (2001).

[143]D. Case, R. Betz, W. Botello-Smith, C. D.S, T. I. Cheatham, T. Darden, R. Duke, T. Giese, H. Gohlke, A. Goetz, N. Homeyey, S. Izadi, P. Janowski, J. Kaus, A. Kovalenko, T. Lee, S. LeGrand, P. Li, C. Lin, T. Luchko, R. Luo, B. Madej, D. Mermelstein, K. Merz, G. Monard, H. Nguyen, H. Nguyen, I. Omelyan, A. Onufriev, D. Roe, A. Roitberg, C. Sagui, C. Simmerling, R. Swails, J. Walker, J. Wang, R. Wolf, X. Wu, L. Xiao, D. York, and P. Kollman, *Amber 16*, University of California, San Francisco, 2016.

[144]R. Luo, L. David, and M. K. Gilson, "Accelerated poisson-boltzmann calculations for static and dynamic systems", J Comput Chem **23**, 1244–53 (2002).

[145]W. Im, D. Beglov, and B. Roux, "Continuum solvation model: computation of electrostatic forces from numerical solutions to the poisson-boltzmann equation", Computer Physics Communications **111**, 59–75 (1998).

[146]B. R. Brooks, R. E. Bruccoleri, B. D. Olafson, D. J. States, S. Swaminathan, and M. Karplus, "Charmm - a program for macromolecular energy, minimization, and dynamics calculations", Journal of Computational Chemistry **4**, 187–217 (1983).

[147]W. Geng, S. Yu, and G. Wei, "Treatment of charge singularities in implicit solvent models", J Chem Phys **127**, 114106 (2007).

[148]W. Rocchia, S. Sridharan, A. Nicholls, E. Alexov, A. Chiabrera, and B. Honig, "Rapid grid-based construction of the molecular surface and the use of induced surface charge to calculate reaction field energies: applications to the molecular systems and geometric objects", Journal of Computational Chemistry **23**, 128–137 (2002).

[149]Q. Cai, J. Wang, H. K. Zhao, and R. Luo, "On removal of charge singularity in poisson-boltzmann equation", J Chem Phys **130**, 145101 (2009).

[150]Y. C. Zhou, S. Zhao, M. Feig, and G. W. Wei, "High order matched interface and boundary method for elliptic equations with discontinuous coefficients and singular sources", Journal of Computational Physics **213**, 1–30 (2006).

[151]M. J. Holst, "Multilevel methods for the poisson-boltzmann equation", Thesis (1993).

[152]M. E. Davis and J. A. Mccammon, "Electrostatics in biomolecular structure and dynamics", Chemical Reviews **90**, 509–521 (1990).

[153]B. Lu, X. Cheng, J. Huang, and J. A. McCammon, "Afmpb: an adaptive fast multipole poisson-boltzmann solver for calculating electrostatics in biomolecular systems", Comput Phys Commun **181**, 1150–1160 (2010).

[154]C. D. Cooper and L. A. Barba, "Poisson-boltzmann model for protein-surface electrostatic interactions and grid-convergence study using the pygbe code", Comput. Phys. Comm. **202**, 23–32 (2016).

[155]C. D. Cooper, J. P. Bardhan, and L. A. Barba, "A biomolecular electrostatics solver using python, gpus and boundary elements that can handle solvent-filled cavities and stern layers", Computer Physics Communications **185**, 720–729 (2014).

[156]W. H. Geng and R. Krasny, "A treecode-accelerated boundary integral poisson-boltzmann solver for electrostatics of solvated biomolecules", Journal of Computational Physics **247**, 62–78 (2013).

[157]J. G. Kirkwood, "Theory of solutions of molecules containing widely separated charges with special application to zwitterions", Journal of Chemical Physics **2** (1934) `Doi10.1063/1.1749489`.

[158]A. T. Fenley, J. C. Gordon, and A. Onufriev, "An analytical approach to computing biomolecular electrostatic potential. i. derivation and analysis", Journal of Chemical Physics **129** (2008) `Artn075101Doi10.1063/1.2956497`.

[159]R. B. McClurg and C. F. Zukoski, "The electrostatic interaction of rigid, globular proteins with arbitrary charge distributions", Journal of Colloid and Interface Science **208**, 529–542 (1998).

[160]G. D. Phillies, "Effects of intermacromolecular interactions on diffusion .1. 2-component solutions", Journal of Chemical Physics **60**, 976–982 (1974).

[161]J. E. Sader and A. M. Lenhoff, "Electrical double-layer interaction between heterogeneously charged colloidal particles: a superposition formulation", Journal of Colloid and Interface Science **201**, 233–243 (1998).

[162]R. R. Gabdoulline and R. C. Wade, "Effective charges for macromolecules in solvent", Journal of Physical Chemistry **100**, 3868–3878 (1996).

[163]D. L. Ermak and J. A. Mccammon, "Brownian dynamics with hydrodynamic interactions", Journal of Chemical Physics **69**, 1352–1360 (1978).

[164]T. Head-Gordon and C. L. Brooks, "The role of electrostatics in the binding of small ligands to enzymes", The Journal of Physical Chemistry **91**, 3342–3349 (1987).

[165]T. Head-Gordon and C. L. Brooks, "Evaluation of simple model descriptions of the diffusional association rate for enzyme-ligand systems", The Journal of Physical Chemistry **93**, 490–494 (1989).

[166]O. Demerdash, E. H. Yap, and T. Head-Gordon, "Advanced potential energy surfaces for condensed phase simulation", Annual Review of Physical Chemistry, Vol 65 **65**, 149–174 (2014).

[167]H. Li, A. D. Robertson, and J. H. Jensen, "Very fast empirical prediction and rationalization of protein pk(a) values", Proteins-Structure Function and Bioinformatics **61**, 704–721 (2005).

[168]S. H. Northrup, S. A. Allison, and J. A. Mccammon, "Brownian dynamics simulation of diffusion-influenced bimolecular reactions", Journal of Chemical Physics **80**, 1517–1526 (1984).

[169]J. D. Madura, J. M. Briggs, R. C. Wade, M. E. Davis, B. A. Luty, A. Ilin, J. Antosiewicz, M. K. Gilson, B. Bagheri, L. R. Scott, and J. A. Mccammon, "Electrostatics and diffusion of molecules in solution - simulations with the university-of-houston brownian dynamics program", Computer Physics Communications **91**, 57–95 (1995).

[170]G. Schreiber and A. R. Fersht, "Rapid, electrostatically assisted association of proteins", Nat Struct Biol **3**, 427–31 (1996).

[171]R. R. Gabdoulline and R. C. Wade, "Protein-protein association: investigation of factors influencing association rates by brownian dynamics simulations", J Mol Biol **306**, 1139–55 (2001).